UNIVERSITY OF CALIFORNIA SAN DIEGO

Ultrafast Dynamics of Coupled Charge, Spin, and Orbital Degrees of Freedom in Perovskite-based Mott-Hubbard Insulators

A dissertation submitted in partial satisfaction of the
requirements for the degree
Doctor of Philosophy

in

Physics

by

Dylan Lovinger

Committee in charge:

Professor Richard Averitt, Chair
Professor Yu-Hwa Lo
Professor Brian Maple
Professor Oleg Shpyrko
Professor Wei Xiong

2020

The dissertation of Dylan Lovinger is approved, and it is acceptable in quality and form for publication on microfilm and electronically:

_____

_____

_____

_____

_____

Chair

University of California San Diego

2020

DEDICATION

To my loving parents, who encouraged my curiosity and love for science, who helped me become the person I am today, and who have always been there for me. Thank you.

EPIGRAPH

"Imagination is more important than knowledge.
For knowledge is limited, whereas imagination embraces the entire world,
stimulating progress, giving birth to evolution."
—Albert Einstein

TABLE OF CONTENTS

LIST OF FIGURES

LIST OF TABLES

ACKNOWLEDGEMENTS

I'd first like to thank my advisor, Professor Richard Averitt. Rick's guidance during my time here has been invaluable, and his hand's off approach has given me so much freedom to learn what experimental and scientific methods work best for me. He is a brilliant scientist and has never failed to provide valuable insight to any question or problem I've encountered. More than that, he has always been incredibly friendly and encouraging. They say that finding an advisor who suits your personality and work style is one of the most important parts of grad school. I think it's true - Rick has helped make this entire process low-stress and enjoyable, and for that I'm incredibly grateful.

The Averitt group as a whole deserves great thanks as well. Jake, Peter, Kevin, Gufeng, and I all joined the Averitt lab around the same time, where we were tasked with building the lab up from scratch. We've all helped each other learn and grow as scientists and been there for moral support through the long nights. All have been great friends and I couldn't have done it without them. Peter in particular deserves special thanks, who worked with me from the start to set up our optical table and has lent a hand in setting up and running most of our experiments. Our newer grad students, Rubaiat, Mustafa, Kelson, Max, Peter, and Ananya have been great to work with as well, and I'm happy that they'll be continuing our work going forward. In general, this has been one of the most laid back and, I daresay, coolest groups around. It's felt like a family, with members who are always willing to help and teach each other. It's been an honor to be a part of the Averitt group.

We've had excellent mentors in the lab when we needed it most, particularly Jingdi who shared so much expertise in building optical experiments, and visiting staff scientist Verner, who provided great assistance (and LabVIEW code!) while running our first experiments. Their help while we were first learning to be experimentalists was instrumental to our success, and I'm very thankful for it.

I'd like to also thank the UCSD physics department as a whole and particularly my cohort.

It's been a pleasure to attend UCSD for grad school. I wouldn't have gotten through my first few years without the help of countless friends I've made, both in terms of schoolwork and my own sanity. I've thoroughly enjoyed my time here because of the amazing people I've met along the way.

A huge thank you goes to my family and my wonderful parents Jeff and Gurli, who raised me to be the person I am today. They encouraged my curiosity and answered every one of my endless "why" questions. I was given all sorts of home experiment kits, crystal growing sets, and old electronics that I could take apart, investigate, and rebuild. My parents fostered my love for science, and ultimately led me down the path I'm on now. Thank you!

Finally, shout out to the big bang and the laws of physics as we know them, whose time-evolution has led to this point and without which none of this would be possible!

Chapter 4 is, in full, currently being prepared for submission and publication in Physical Review B. Dylan Lovinger, Matthew Brahlek, Peter Kissin, Dante Kennes, Andrew Millis, Roman Engel-Herbert, Richard D. Averitt. The dissertation author was the primary investigator and author of this material.

Chapter 5 is, in full, a reprint of the material submitted for publication in Physical Review X. Dylan Lovinger, Eli Zoghlin, Peter Kissin, Gihyeon Ahn, Kaveh Ahadi, Peter Kim, Maxwell Poore, Susanne Stemmer, Soonjae J. Moon, Stephen D. Wilson, Richard D. Averitt. The dissertation author was the primary investigator and author of this material.

VITA

2012	B. S. in Physics and Mathematics, University of Massachusetts Amherst
2012-2015	Graduate Teaching Assistant, University of California San Diego
2014	M. S. in Physics, University of California San Diego
2020	Ph. D. in Physics, University of California San Diego

PUBLICATIONS

Dylan Lovinger, Eli Zoghlin, Peter Kissin, Gihyeon Ahn, Kaveh Ahadi, Peter Kim, Maxwell Poore, Susanne Stemmer, Soonjae Moon, Stephen D. Wilson, and Richard D. Averitt. *Magneto-Elastic coupling to coherent acoustic phonon modes in ferrimagnetic insulator $GdTiO_3$*, (under review, Physical Review X)

Dylan Lovinger, Matthew Brahlek, Peter Kissin, Dante Kennes, Andrew Millis, Roman Engel-Herbert, Richard Averitt. *Influence of spin and orbital fluctuations on Mott-Hubbard exciton dynamics in $LaVO_3$ Thin Films*, (in preparation)

Peter Kissin, Sheng Ran, **Dylan Lovinger**, Verner K. Thorsmølle, Noravee Kanchanavatee, Kevin Huang, M. Brian Maple, and Richard D. Averitt. *Quasiparticle relaxation dynamics in $URu_{2-x}Fe_xSi_2$ single crystals*, Physical Review B **99**, 165144 (2019). https://doi.org/10.1103/PhysRevB.99.165144

Marshall van Zijll, Emilie Huffman, **Dylan Lovinger**, Shirley Chiang. *Unusual island formations of Ir on Ge(111) studied by STM*, Surface Science **666**, 90-95 (2017).

Dylan Lovinger, Robert B. Hallock. *Temperature dependence of helium diffusion through common epoxies*, Journal of Physics: Conference Series **400**, 052006 (2012).

ABSTRACT OF THE DISSERTATION

Ultrafast Dynamics of Coupled Charge, Spin, and Orbital Degrees of Freedom in Perovskite-based Mott-Hubbard Insulators

by

Dylan Lovinger

Doctor of Philosophy in Physics

University of California San Diego, 2020

Professor Richard Averitt, Chair

The coupling of charge, spin, and orbital degrees of freedom gives rise to a wide range of emergent physics, resulting in numerous materials with interesting electronic and magnetic properties. Among these are Mott-Hubbard insulators, whose electronic interactions lead to a ground state that cannot be described by a non-interacting band theory. In this work we study two such materials, $LaVO_3$ (LVO) and $GdTiO_3$ (GTO), using ultrafast optical pump-probe reflectivity and magneto-optical Kerr spectroscopy. These time-resolved techniques allow us to partially disentangle the competing degrees of freedom, giving insight into how they interact at their fundamental timescales when driven out of equilibrium. By studying the excitation and relaxation

dynamics we observe signatures of the spin and orbital order phase transitions, as well as evidence of how they couple to other degrees of freedom. In LVO this coupling gives rise to exciton formation, bound electron-hole pairs that arise from the interaction of with a spin and orbitally ordered lattice. In GTO, we observe correlation of an acoustic phonon to the magnetic order, indicative of magneto-elastic coupling. This involves transient strain-induced modification of the magnetic exchange interaction, resulting in a novel method of coupling light to the magnetic degrees of freedom. These effects highlight the physics that emerges from strongly coupled degrees of freedom, and our results provide new ways to understand and manipulate them.

Chapter 1

Introduction and Motivation

As our understanding of fundamental physics grows, research shifts toward the study of more and more complex systems. In Condensed Matter physics, we have moved from the non-interacting electron model of Drude Theory in simple metals, to the rich complexity of highly correlated transition metal oxides (TMOs) and quantum materials. It is in these complex materials where rich and often unexpected physics emerges, and it is here where we turn our attention. Systems with strongly correlated charge, spin, lattice, and orbital degrees of freedom produce an incredible array of complex phenomena owing to their internal competition and interaction. This includes high-T_C superconductivity, colossal magneto-resistance, Mott-Hubbard insulators, topologically protected states of matter, metal-insulator transitions, and much more [1, 2, 3]. It is the goal of our group and this work to better understand the fundamental physics associated with these quantum materials.

Due to their strongly correlated nature, where underlying phases compete and reinforce one another, quantum materials are highly sensitive to changes in external parameters. This offers an opportunity for the experimentalist to adjust and control relevant material properties. Tuning, for example, the external temperature, pressure, electric field, or magnetic field can have drastic effects on the electronic properties (such as resistivity, magnetism, etc). In addition, growth

parameters offer another form of control, where electron/hole doping and epitaxial strain of thin films on particular substrates allows one to explore an entire phase diagram of new states. In many high-T_C superconductors, for example, doping triggers the superconducting state the alters the critical temperature [2].

The tuning parameters above are all static, however, applying primarily to systems in equilibrium. More recently, attention has turned toward driving these materials out of equilibrium to induce macroscopic changes and study dynamics. There is no better suited tool for this task than light, a field of study known as time-resolved spectroscopy. A high energy ultrashort laser pulse is capable of sharply raising the local temperature beyond a critical threshold, directly exciting particular electronic transitions, or driving phonon modes that couple to other degrees of freedom, all of which can alter the macroscopic properties of the material. Furthermore, the energy of a photon can be precisely tuned, enabling mode-selective excitation of specific degrees of freedom. Finally, these optically-induced changes are enacted on femtosecond to picosecond timescales, offering a form of control orders of magnitude faster than any other method.

Time-resolved spectroscopy is more than just a knob for tuning material parameters though. The dynamic study of matter gives us another approach to disentangle the coupled degrees of freedom in strongly correlated materials, and may be one of the keys to understanding these complex systems. After selectively exciting one degree of freedom with a femtosecond pulse, we can observe how energy is exchanged to others on the fundamental timescales at which matter moves and interacts. Phases in competition can be quenched or emerge on these timescales, providing insight into exactly how they are coupled to one another. The characteristic times at which these excited states evolve and recover also helps identify the specific underlying processes. In the end, ultrafast time-resolved spectroscopy provides both a promising form of controlling material parameters, and one of the most modern methods of understanding those materials.

This dissertation is structured as follows. Chapter 2 provides a background to the relevant physics at play in the experiments performed, including Mott-Hubbard insulators and critical

phenomena. Chapter 3 provides an overview of the experimental techniques and methods used to collect and analyze data. Chapter 4 details the work done on $LaVO_3$, where we study critical dynamics at an orbital, magnetic, and structural phase transition. Chapter 5 details the work on $GdTiO_3$, where we observe laser-induced magnetic dynamics and strong magneto-elastic coupling, indicating a potential method of indirectly modifying the exchange interaction on ultrafast timescales. Finally, chapter 6 provides a conclusion and outlook for future work.

Chapter 2

Background

Spectroscopy is, at its heart, the study of light-matter interactions. We therefore begin with the physics of light.

2.1 Optical Response of Materials

In the study of material properties using light, our goal is to take a measured observable, such as the transmission or reflectivity, and relate it to more fundamental properties. Only two quantities are required to completely describe the response of matter to an electromagnetic wave, as they are the only additional terms that appear in Maxwell's equations in a medium. These are the dielectric function, or electric permittivity ε, and the magnetic permeability μ. ε describes the displacement of charges in an electric field, a measure of how strongly bound electrons in the material respond and can be polarized, while μ describes the magnetic response. The electric displacement $\vec{D}$ in an electric field $\vec{E}$, and the magnetic flux density $\vec{B}$ in a magnetic field $\vec{H}$, are

quantified simply as

$$\vec{D} = \varepsilon \vec{E} \tag{2.1}$$

$$\vec{B} = \mu \vec{H}, \tag{2.2}$$

respectively. This linear description with static charges, however, is too simplistic. In the field of optics, we are concerned with the time-varying electric field of light and real materials with losses and axial dependencies. The dielectric function is truly a complex rank 2 tensor with a frequency dependence that encapsulates this. For simplicity we will now consider an isotropic medium and ignore the tensor nature, writing the dielectric function as

$$\tilde{\varepsilon}(\omega) = \varepsilon_1 + i\varepsilon_2. \tag{2.3}$$

Generally, the real part of $\tilde{\varepsilon}$ describes the degree of polarization, while the imaginary part describes damping and loss of the field in the material. The permeability μ is also complex and frequency dependent, but in the regimes we study and with the weak magnetic response of crystals it can be ignored considered constant (i.e. $\mu = \mu_0$) [4].

From the complex dielectric function we can define a number of other optical constants which will aid our description of light-matter interactions. First and foremost is the complex optical conductivity, given by

$$\tilde{\sigma}(\omega) = \sigma_1 + i\sigma_2. \tag{2.4}$$

This can be written in terms of the dielectric function as

$$\tilde{\sigma}(\omega) = i\omega(\varepsilon_0 - \tilde{\varepsilon}). \tag{2.5}$$

While $\tilde{\varepsilon}(\omega)$ characterizes the response of a bound charge to an electric field, the optical conduc-

tivity $\tilde{\sigma}(\omega)$ characterizes the response of free charges. This produces a current of the form

$$\tilde{J}(\omega) = \tilde{\sigma}(\omega)E(\omega). \tag{2.6}$$

This reduces to the familiar linear expression $J = \sigma E$ for a free charge in vacuum, but in a medium axial differences and off-diagonal terms in the complex conductivity tensor must be considered. The optical conductivity is extremely useful in informing the choice of wavelength in an experiment, as it indicates where the optical response is strongest, where gaps appears, and more.

A second useful quantity is the complex index of refraction, $\tilde{n}(\omega) = n + ik$, used to describe the behavior of an electromagnetic wave in a medium. The real part n describes the phase velocity of the wave, and is therefore effective at modeling the slowing and bending of light in a medium. The imaginary part k describes losses, specifically the attenuation of light as it propagates in a medium and thus the penetration depth. The index of refraction, in a typical material where $\mu = \mu_0$, can again be written in terms of the dielectric function as

$$n = \left(\frac{\varepsilon_1 + \sqrt{\varepsilon_1^2 + \varepsilon_2^2}}{2\varepsilon_0} \right)^{1/2} \tag{2.7}$$

$$k = \left(\frac{-\varepsilon_1 + \sqrt{\varepsilon_1^2 + \varepsilon_2^2}}{2\varepsilon_0} \right)^{1/2}. \tag{2.8}$$

In this manner, all of our optical constants are inter-related and can be framed in terms of one another, depending on the experimental use case. For a complete table of these forms, refer to Ref. [5]. We now have a mathematical framework for describing the fundamental interactions between light and matter.

2.2 Drude Theory

We now wish to connect the optical constants to the electromagnetic response of a material, in an effort to understand the physical origin of such responses. The starting point for a theoretical description of the carrier response is always Drude Theory. The Drude-Lorentz Model is a simple, non-interacting model of the electron as a bound oscillator based on classical equations of motion with a charge in a field. In its general form it describes a bound charge at an arbitrary resonant frequency, and is effective at modeling resonant phenomena such as optical phonon modes.

The most significant contribution to the optical constants, however, is the "free carrier" response where the resonant frequency $\omega_0 = 0$. In this case, electrons are unbound and move freely, with a characteristic scattering time τ. The Drude contribution to the dielectric function can be written as

$$\tilde{\varepsilon}_D(\omega) = 1 - \frac{\omega_p^2}{\omega^2 + i\tau\omega}, \tag{2.9}$$

where ω_p^2 is the plasma frequency. It is defined as

$$\omega_p^2 \equiv \frac{ne^2\tau}{m^*}, \tag{2.10}$$

where n is the carrier density, e is the carrier charge, and m^* is the carrier effective mass. Furthermore, the complex optical conductivity can be expressed in these terms as

$$\tilde{\sigma}_D(\omega) = \frac{\omega_p^2}{1 - i\omega\tau}. \tag{2.11}$$

Eq. 2.11 is known as the Drude conductivity. Despite its simplicity, the Drude model is remarkably useful in predicting the optical properties and conductivity of many materials, especially simple metals and doped semiconductors. At low frequencies it shows that a material with sufficient carriers is perfectly reflective, and at high frequencies the Drude contribution becomes zero, the material behaving like a dielectric and becoming transparent. The crossover point, near the plasma

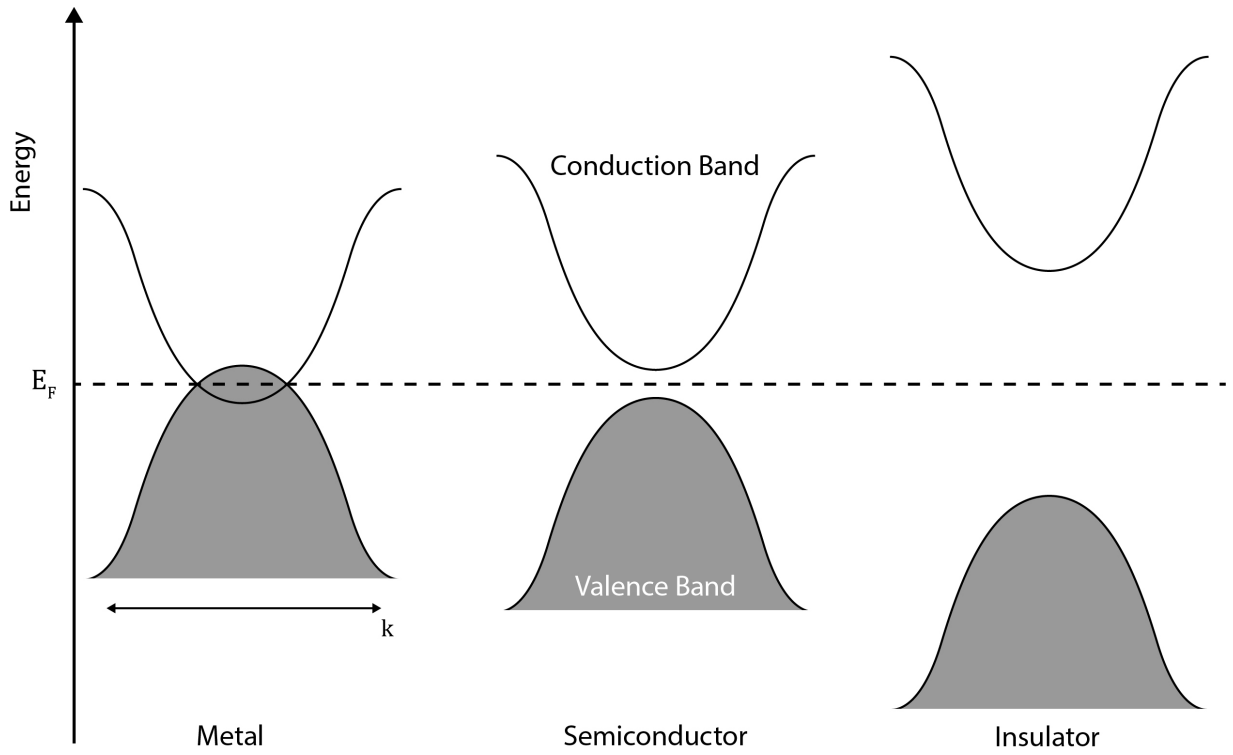

Figure 2.1: Band structure diagram near the Fermi level E_F for metals, semiconductors, and insulators. The Fermi level must lie at least partially within the conduction band for the material to freely conduct, as shown in the left-most diagram for a metal.

frequency ω_p, is where carriers stop effectively responding to the electric field, and there are further features in the optical conductivity below ω_p and near the scattering rate frequency $1/\tau$. Where the Drude model breaks down most noticeably is in strongly correlated materials, where the electronic degrees of freedom begin interacting heavily. In the case where electron-electron interactions are strong, the carriers can no longer be treated as isolated and independent and the Drude predictions fail.

2.3 Band Theory and Mott-Hubbard Insulators

The concept of non-interacting electrons has further implications for understanding material properties, including band theory. Consider the motion of electrons on a periodic lattice, with periodic potential wells centered at each lattice site and no electron-electron interactions. In

the limit of many lattice sites, the Schrödinger equation for such a configuration has an energy spectrum with respect to momentum k that is split into continuous energy bands separated by band gaps [6]. The number of bands and their filling is determined by the number and nature of atomic orbitals, and the total number of electrons. The occupancy of these bands determines the conduction properties of the material, as shown in Fig. 2.1. If the conduction band is partially occupied or overlaps with the valence band, electrons are free to move within the band (itinerant) or hop between lattice sites, and the material is a conductive metal. If the valence band is fully occupied, motion and hopping is suppressed, and the material is insulating. Semi-conductors also have a fully occupied valence band, but the gap between this band and the the conduction band is small enough that thermal fluctuations can promote some carriers into a conducting state.

This band model is simplistic yet effective at predicting the conduction properties of many materials, but it encounters the same failings as Drude theory; for more complex materials with strong correlations the theory breaks down because it ignores interactions. Hopping from one site to a nearest neighbor contributes kinetic energy, but also costs some amount of energy at least equal to the Coulomb repulsion between carriers. This becomes relevant and must be considered for materials where the Coulomb energy is on the same order as or higher than the hopping energy. In these cases, we turn to the Hubbard model to make predictions about the material. The Hubbard hamiltonian can be written as

$$H = -t \sum_{\langle ij \rangle, \sigma} c^{\dagger}_{i\sigma} c_{j\sigma} + U \sum_{i} n_{i\uparrow} n_{i\downarrow}, \tag{2.12}$$

where t represents the hopping (kinetic) energy, c is the creation/annihilation operator for electrons at site i with spin σ summed over nearest neighbors $\langle ij \rangle$, and U represents the energy of Coulomb repulsion for electrons at site i with opposite spin [7]. This quantifies the energy cost of creating a doublon or electron-hole pair as U, with corresponding kinetic energy gain equal to the Hubbard bandwidth $W = 2zt$, where z is the number of nearest neighbors [6]. The ratio of U to W then

determines the mobility of carriers in the system. If $U/W < 1$, then the hopping term is dominant and it is energetically favorable for carriers to move through the system. The electrons are itinerant and the material can be classified as a metal, as traditional band theory would predict. If $U/W \geq 1$, then the Coulomb cost exceeds the kinetic gain and carriers remain localized. A gap in the density of states opens as U/W increases, splitting the valence band into an upper and lower Hubbard band at the Fermi Energy. While band theory may have predicted a metallic state, the material is insulating due to strong electron-electron correlations and is classified as a Mott-Hubbard (MH) insulator.

MH insulators represent a prototypical class of strongly correlated materials, better known as quantum materials. They are a textbook example of the rich physics that emerges from strongly interacting degrees of freedom, and showcase the importance of considering many-body interaction effects when developing a theory of solids. Often, MH insulators display other strong-correlation effects, such as coupled spin and orbital order, colossal magnetoresistance (where electrical resistance becomes a function of magnetic field), and superconductivity (where carriers interact to move as Cooper pairs with zero resistance). These effects and more make MH insulators extremely promising materials to study both the fundamental physics of strong interactions and the applications thereof. Both of the materials reported on in this dissertation, LVO_3 and $GdTiO_3$, are MH insulators, and represent classes of material with strongly interacting electronic degrees of freedom that give rise to unconventional physics.

2.4 Photoexcitation and the Effective Temperature Model

Time-resolved optical experiments are concerned with non-equilibrium dynamics, involving energy transfer between internal degrees of freedom after photoexcitation. In this section, we discuss a phenomenological theory for modeling this transfer process, known as the effective temperature model, or two/three temperature model (TTM).

There are main degrees of freedom in a solid state system which we are primarily concerned with: spin, lattice, and electron. Each subsystem has a particular temperature T_s, T_l, and T_e, and a particular heat capacity C_s, C_l, and C_e, respectively. After exciting this system with a laser pulse, energy and heat is exchanged internally through various relaxation and coupling processes. This energy and temperature exchange is quantified by the effective temperature model, composed of a series of heat diffusion differential equations. It is written as [8]

$$C_e \frac{\partial T_e}{\partial t} = G_{el}(T_l - T_e) + G_{es}(T_s - T_e) + P \tag{2.13}$$

$$C_s \frac{\partial T_s}{\partial t} = G_{sl}(T_l - T_s) + G_{es}(T_e - T_s) \tag{2.14}$$

$$C_l \frac{\partial T_l}{\partial t} = G_{sl}(T_s - T_l) + G_{el}(T_e - T_l), \tag{2.15}$$

where P represents the absorbed laser energy at $t = 0$ (determined by the laser fluence and often approximated as a delta function), and G_{xy} is the coupling strength between subsystems x and y. This is a homogeneous form of the model, which assumes spatial homogeneity and is valid in most experimental cases. In the inhomogeneous limit, an additional term $\nabla(\kappa_x \nabla T_x)$ must be added to each equation, where κ_x is the thermal conductivity for each subsystem.

The solution to the effective temperature model takes the form of an exponential decay with $T_x \propto e^{-t/\tau_{x-y}}$, where τ_{x-y} represents the characteristic time constant for coupling between subsystem x and y. A representative solution set is shown in Fig. 2.2, depicting the time evolution of the electron, spin, and lattice subsystem temperatures after photoexcitation with a femtosecond laser pulse. Before the pulse, at $t < t = 0$, the system is in thermal equilibrium with $T_s = T_l = T_e = T_0$. At $t = 0$ the laser pulse creates a non-equilibrium distribution of only electrons, due to their direct absorption of the light and their much lower heat capacity, sharply raising T_e. The electrons thermalize with each other through electron-electron scattering, then begin exchanging energy with the spin subsystem through electron-spin coupling, and with the lattice through electron-phonon coupling. During this time, spin-lattice coupling provides an

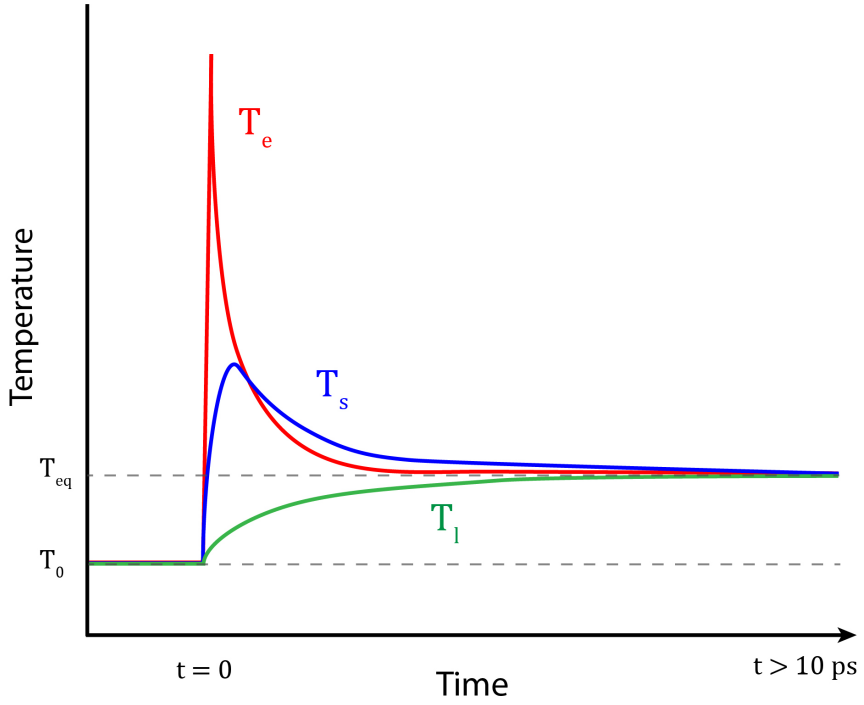

Figure 2.2: Time evolution of the electron (T_e), spin (T_s), and lattice (T_l) temperatures according to the effective temperature model. Photoexcitation at $t = 0$ directly creates a high temperature electron population, which exchanges energy with the lattice and spin subsystems until they come into thermal equilibrium at $T_{eq} > T_0$.

additional energy exchange pathway, but it is very weak compared to others and contributes to the slow equilibration time of the lattice. After a period of time on the order of picoseconds, all three subsystems come into thermal equilibrium at a temperature $T_{eq} > T_0$. At a much later time, on the order of nanoseconds, heat diffuses out of the system and the collective temperature returns to T_{eq}.

While the effective temperature model is simple and does not capture the microscopic physics at work, it does provide useful insight into the processes following photoexcitation, which involve transfer of energy between various internal degrees of freedom. We have discussed three here, the electron, spin, and lattice subsystems, but there are many more in a real material. Orbital degrees of freedom play an important role in most systems, especially in those with orbital order, as well as any other quasiparticle or collective excitation (such as excitons, plasmons,

Cooper pairs, etc). These subsystems are all coupled and exchange energy with one another following laser excitation, and this exchange is a fundamental contribution to the time-resolved signal in a pump-probe experiment. This gives insight into why experimental pump-probe data is often well-fit by a serias of exponential functions - to first order, it is often a heat exchange process between multiple internal degrees of freedom. This can be used to estimate the coupling strength between particular subsystems, for example by identifying a relaxation process as e.g. spin-lattice thermalization, extracting an exponential time constant from the time-dependent data, and approximating the time constant as $\tau_{s-l} = C_s/G_{s-l}$. If the coupling strength G is already known, fitting of the time constants can provide experimental verification.

2.5 Phase Transitions and Critical Dynamics

Throughout our experiments we drive materials to their extremes, exploring the myriad electronic, magnetic, and structural phases that they exist in. Often, the most interesting results involve how a material changes and behaves at or beyond one of it's phase transitions. This includes the paramagnetic to ferrimagnetic phase transition of GTO [9], the simultaneous spin, orbital, and structural ordering transitions in LVO [10, 11], the metal-insulator transition in VO_2 and V_2O_3 [12], superconducting transitions in Cuprates and other superconductors [2], and much more. In some sense, our work truly focuses on the optical signatures of phase transitions, thus it is important to discuss the fundamental nature of a phase transition.

Generally, a phase transition is marked by dramatic changes in the thermodynamic properties of a system under changes of an external parameter, such as temperature or pressure. This is accompanied by changes in or breaking of symmetry, typically from a high-temperature high symmetry (i.e. more disordered) phase to a low-temperature, low symmetry ordered phase. Structural phase transitions involve a change of crystal symmetry, for example, and magnetic phase transitions involve the collective ordering of spins. As the system is driven toward a phase

transition, or a new minimum of the free energy, a particular ground state order is "chosen" in a process referred to as spontaneous symmetry breaking. This change in symmetry is a hallmark of all phase transitions, from elementary particles to astronomical systems, and can be characterized by a measure known as the order parameter. In structural transitions the order parameter may refer to the ratio of certain crystallographic axes, or in magnetic transitions the magnetization m. Phase transitions can be classified by the behavior of the order parameter at the transition point; in a first order phase transition, the order parameter is discontinuous, while in a second order phase transition the order parameter changes continuously.

The pathway to a phase transition can be mapped and quantified by the free energy of the system. The free energy can be constructed explicitly from the expression $F = U - TS$, where U is the internal energy, S is the entropy, and T is the temperature. This requires consideration of various microscopic details of the system, either explicitly (e.g. individual spin states on a lattice) or as a mean field average (e.g. averaging spins to parametrize the magnetization m). But this approach is not always practical or wise, particularly in the many-body systems encountered in condensed matter physics. Enter Landau Theory. By taking the mean field approach, recognizing that the order parameter is very small in the vicinity of the transition temperature T_C, and considering certain symmetries of the system, we can develop an effective phenomenological route to the free energy F.

In the following we will focus on a ferromagnetic phase transition, using the magnetization m as the order parameter. With a mean field approach this is defined as the average magnetization of a spin, $m = \langle \sigma_i \rangle$, and is zero in the high temperature disordered state. The full free energy can be written as an integral over the parameter space of the free energy density f,

$$F = \int f(x) d^d x. \tag{2.16}$$

Because the order parameter m is small near the transition, we may write the free energy density f

as a generalized Taylor expansion [13]:

$$f(m) = -Hm + Am^2 + Bm^3 + Cm^4 + ... \tag{2.17}$$

where H is an applied magnetic field and A, B, and C are temperature-dependent coefficients specific to the physical system. Due to the magnetic symmetry of the system, symmetric under the transformation $m \to -m$ in zero field, the odd terms of the free energy drop out and we are left with

$$f(m) = Am^2 + Cm^4, \tag{2.18}$$

excluding higher order terms. We may consider the temperature dependence of the system by defining A as:

$$A(T) = \alpha(T - T_C), \tag{2.19}$$

where α is a parameter and T_C is the critical (transition) temperature. The phase transition now occurs at T_C, the point where $A(T)$ switches sign. Using this form of the free energy we can begin to understand how the system behaves and changes over the course of a phase transition.

Fig. 2.3 depicts the free energy f as a function of the order parameter m for three values of A: first where $A > 0$ and thus $T > T_C$ (blue curve), then for $A = 0$ at $T = T_C$ (orange curve), and finally for $A < 0$ and $T < T_C$ (yellow curve). The ground state of the system lies at the free energy minimum, much like a potential energy minimum, which provides some intuition in interpreting the curves. Above T_C there is only one minimum, the magnetically disordered state with $m = 0$. This widens as the transition is approached, then bifurcates into two minima separated by some non-zero value of the order parameter, indicating a degenerate ground state with non-zero net magnetization. The red ball and arrow indicates how the system relaxes to a new ground state during the phase transition, by following the free energy landscape to its minimum. In making a "choice" between two such degenerate minima, the ground state symmetry

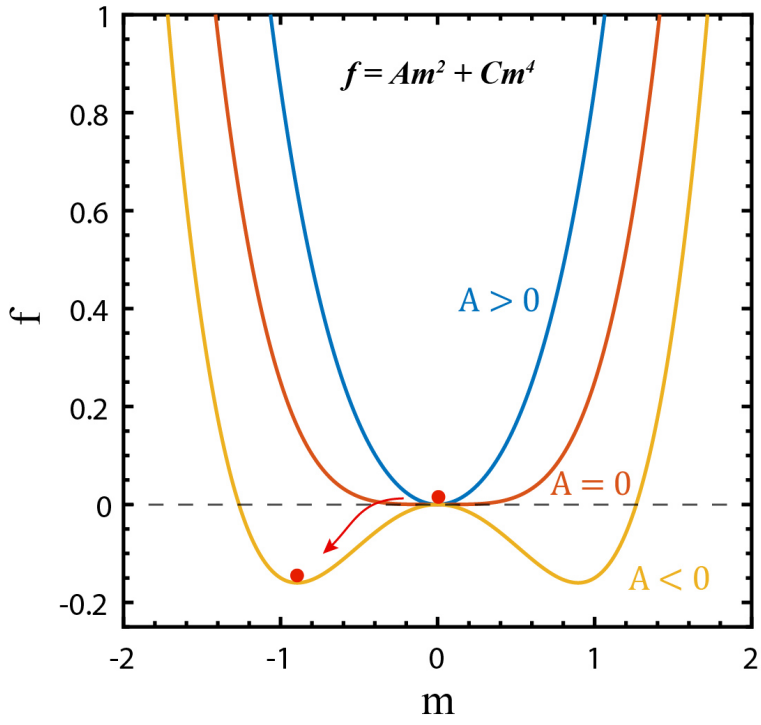

Figure 2.3: The free energy f as a function of order parameter m (magnetization). The parameter A is a function of temperature such that $A(T) = \alpha(T - T_C)$. The blue curve represents the free energy above the phase transition temperature ($T > T_C$), the orange curve at the transition ($T = T_C$), and yellow below the transition ($T < T_C$). The red ball indicates how the system relaxes to the new ground state during the phase transition. At $T = T_C$, dynamics slow due to widening and flattening of the free energy landscape, a phenomenon known as critical slowing down.

is spontaneously broken, hence the name spontaneous symmetry breaking. The free energy also provides phenomenological insight into the dynamics, which tend to slow at a phase transition; at $T = T_C$ the free energy landscape flattens, such that the ground state minimum widens and any perturbation of the order parameter takes longer to reach equilibrium. Consider for example a ball in a gravitational potential, which takes longer to reach equilibrium in a wide, shallow potential well like that depicted in the $A = 0$ curve of Fig. 2.3. This slowing of dynamics is known as critical slowing down, one aspect of a larger study in critical phenomena introduced below.

2.5.1 Critical Exponents

As stated above, the minima of the free energy correspond to the ground states of the system. We can find the local minima of f (in zero field) by computing the first derivative and setting it to zero:

$$\frac{\partial f}{\partial m} = 0 \tag{2.20}$$

$$2A(T)m + 4Cm^3 = 0 \tag{2.21}$$

which yields the solutions

$$m = 0 \quad \text{and} \quad m = \pm\sqrt{-\frac{A(T)}{2C}}. \tag{2.22}$$

The first solution corresponds to the state above T_C, the second below. It is the latter quantity we are interested in, which can be rewritten as

$$m = \pm\sqrt{-\frac{\alpha(T - T_C)}{2C}} \tag{2.23}$$

$$m = \pm\sqrt{\frac{\alpha\, t}{2C}}, \tag{2.24}$$

where t is the reduced temperature defined as

$$t \equiv \frac{T - T_C}{T_C} \tag{2.25}$$

Therefore, the ground state magnetization is proportional to the reduced temperature

$$m \propto \left(\frac{T - T_C}{T_C}\right)^{\beta} \propto t^{\beta}, \tag{2.26}$$

where $\beta = 1/2$ and is known as a critical exponent. While the exact proportionality is dependent on microscopic details of the system, the critical exponent is not, depending rather on the

Table 2.1: Table of various static critical exponents related to magnetic parameters, and their values in differing dimensions and symmetries. M is the magnetization, χ is the magnetic susceptibility, C is the specific heat, ξ is the correlation length, and S is the correlation function [14].

Exponent	Definition	Mean Field	Ising ($d = 2$)	Ising ($d = 3$)	Heisenberg ($d = 3$)
β	$M \propto t^{\beta}$	0.5	0.125	0.3265(3)	0.3689(3)
γ	$\chi \propto t^{-}\gamma$	1	1.75	1.2372(5)	1.3960(9)
α	$C \propto t^{-\alpha}$	–	0	0.110(1)	-0.1336(15)
ν	$\xi \propto t^{-\nu}$	0.5	1	0.6301(4)	0.7112(5)
η	$S \propto q^{-2+\eta}$	0	0.25	0.0364(5)	0.0375(5)

symmetry of our magnetic model or system. This introduces the concept of universality.

There are numerous other thermodynamic quantities which can be described by power law scaling of the reduced temperature near T_C. Some other universal critical exponents include specific heat (exponent α), susceptibility (γ), correlation length (ν). These exponents belong to particular universality classes which depend only on the symmetry of the order parameter, the spatial dimensionality of the system, and the range of interactions. A few are listed in Table 2.1 for various symmetries and dimensions, in the context of magnetic systems in zero field [13][14][15][16][17]. This universal scaling behavior is partly due to length scale invariance as the correlation length ξ diverges near T_C, washing out the microscopic details of the system. The universality of the above quantities means that, so long as they share certain symmetries, wildly different systems may have order parameters which scale identically and behave similarly at the phase transition [18]. Other implications are length scale invariance due to a diverging correlation length, the existence of various universal scaling laws relating the critical exponents to one another, and the divergence of the order parameter at T_C.

The above introduces static, time-averaged critical exponents, but dynamic quantities also display critical behavior. Of particular relevance to our work is the characteristic time, which

Table 2.2: Dynamic critical exponents z, for various magnetic models. The anisotropic models can be either FM or AFM [14][19].

Model	Definition	z ($d = 3$)
Heisenberg (FM)	$(d+2-\eta)/2$	~ 2.5
Heisenberg (AFM)	$d/2$	1.5
Anisotropic Magnet	$2+\alpha/\nu$	~ 2
Anisotropic Kinetic Ising	$2+0.72\,\eta$	~ 2

broadly refers to time-dependent behavior like spin fluctuation rates or excited quasiparticle recovery rates. Dynamical scaling theory lets us relate static quantities, such as the correlation length, to dynamic ones [19]. The characteristic time τ scales as

$$\tau \propto \xi^z \propto t^{-z\nu}, \tag{2.27}$$

where ξ is the correlation length and ν it's critical exponent, and z is the dynamical critical exponent. Table 2.2 lists z for various magnetic models [19]. As a phase transition is approached the characteristic timescale diverges in a process known as critical slowing down. This is particularly relevant to our time-resolved measurements, in which we observe critical slowing down of excited-state recovery rates near magnetic, orbital, and structural phase transitions. Critical slowing down has been observed in a wide range of other systems, from spin relaxation dynamics in ferromagnets [20][21] to neural spiking in brain activity [22], and can often be interpreted as a sign that a phase transition is imminent.

A useful phenomenological description of critical slowing down involves the flattening of the free energy introduced in the previous section and in Fig. 2.3. In this picture, small perturbations from equilibrium take much longer to recover in a flat potential landscape, leading to a collective slowing of dynamics. Microscopically, this can be related to diverging length scales and correlation lengths near T_C. As the correlation length grows to macroscopic scales, the

internal restoring forces which would guide the system to the above-T_C equilibrium grow weaker and slower, until the system settles into a new equilibrium state. Examples of this are found in both material systems studied, $LaVO_3$ and $GdTiO_3$, discussed in Chapter 4 and Chapter 5.

Chapter 3

Experimental Techniques

3.1 Time-Resolved Spectroscopy

Our primary tool used to investigate the optical response of materials is time-resolved optical spectroscopy. This is as opposed to static optical measurements (e.g. Raman), which excel at measuring equilibrium properties such as band structure and optical conductivity. Time-resolved spectroscopy on the other hand is dynamic, measuring the evolution of material properties after excitation with light. This allows access to novel and often inaccessible non-equilibrium states which contain a wealth of information on how strongly coupled degrees of freedom interact. As the system relaxes back to equilibrium after excitation, various timescales emerge which correspond to physical processes and transfer of energy between subsystems (lattice, electron, spin). In its simplest form, this process is described by the effective temperature model, discussed in Sec. 2.4. After hundreds of picoseconds to nanoseconds, typically, heat is transferred out of the sample and the system returns to equilibrium. During the recovery, each process is accompanied by a characteristic timescale, discernible by later analysis and fitting.

To gather time-resolved data, we employ an experimental technique known as ultrafast pump-probe spectroscopy. A high-energy femtosecond pump pulse is used to selectively excite a

sample, followed by a weaker probe pulse which monitors the photoinduced change in reflectivity or transmission. By varying the delay time between pump and probe pulses we can record the photoexcited changes as a function of time and map out the evolution of excited states. "Ultrafast" refers to the relevant timescales measured in these experiments, ranging from a few femtoseconds to hundreds of picoseconds ($10^{-15} - 10^{-12}$ s). These are the fundamental timescales at which matter moves and interacts, at which energy is exchanged between the electron, spin, and lattice subsystems [23], essential to understanding the dynamics of complex condensed matter systems.

An educated choice of pump and probe wavelength is crucial in designing spectroscopic experiments. With experimental capabilities that span from the visible through mid-IR and into THz, we have a wide range of excitation energies and related phenomena to choose from. The work described in this thesis focuses on excitation in the visible range ($\sim 1.5 - 2.4$ eV), where laser energies typically lie at or above the material band gap. This promotes carriers above the Fermi level to the conduction band, and generates a population of non-equilibrium electrons which take up to nanoseconds to relax back to the ground state. During this process we are able to study coupling/thermalization between electronic, phonon, and magnetic subsystems; quasiparticle generation, scattering, and recombination; the effect of phase transitions on the above, and more. Determination of the exact wavelength in the visible region is often aided by a study of the optical conductivity determined by static measurements. As discussed in Sec. 2.1, the optical conductivity $\sigma_1(\omega)$ is a material property that defines the response to light at a given frequency. A higher optical conductivity implies a larger and cleaner signal. In addition, there are typically changes in $\sigma_1(\omega)$ with temperature, spectral broadening or transfer of spectral weight from one frequency region to another, signifying the opening or closing of a gap in the density of states or other changes to electronic occupancy. These regions are of particular interest and help define the parameters of our experiment.

3.2 Experimental Setup

3.2.1 Pulsed Laser Operation

The heart of any time-resolved spectroscopy experiment is the pulsed laser. For most KHz systems this consists of an optical resonator called the oscillator and an amplification stage. Light from a laser diode is directed into the oscillator optical cavity, containing two mirrors with a gain medium (such as Ti:Sapph, Nd:YAG, or Yb:KGW) between them. The gain medium is externally pumped until population inversion is achieved, where there is a greater number of occupied high-energy excited states than there are unexcited states. At this point amplification can occur. The electric field of light circulating in the cavity prompts phase-coherent photoemission from excited states in the gain medium, a process called stimulated emission. This adds energy to the light in the cavity on each pass through the gain medium.

Light within the cavity is continuously amplified in this manner, but in order to produce an ultrashort laser pulse additional elements must be introduced. The most effective method for generating femtosecond pulses is known as mode locking, which actively or passively fixes the relative phase of the modes allowed in the cavity and allows a pulse to constructively form. There are many methods to achieve mode locking, including an active acousto-optic modulator to periodically modulate the resonator, a gain medium that employs passive self-focusing Kerr lensing (Ti:Sapph), or in our case, use of a saturable absorber mirror. Any incident light is first absorbed before saturating the absorber and being reflected by the mirror, introducing a time-variation to the intensity and a mechanism to reject low-intensity light. This preferentially selects the highest intensity light, cutting out the continuous background and allowing a high-energy pulse to form that can be coupled out of the oscillator.

To produce high energy mJ and μJ pulses of KHz lasers, pulses are then selected by a pulse picker and sent to an amplification stage. This consists of an additional gain medium which further amplifies the intensity of light. To avoid damaging optics at such high energies, pulses are

temporally stretched before this stage to lower the peak intensity, and re-compressed to an ultra short duration after.

The particular laser system that this work makes use of is the Spectra-Physics Spirit, a Yb-based hybrid-fiber pulsed laser. The output is a 350 fs pulse centered at 1040 nm, at a repetition rate of 209 KHz with a pulse energy of 38 μJ. This averages to 8 W of power, half of which is used to drive a THz spectroscopy setup that is beyond the scope of this work, the other half of which is used to generate visible light for optical pump-probe experiments and will be discussed in the following section.

3.2.2 Nonlinear Optical Parametric Amplification

For most optical pump-probe experiments it is desirable to operate with a choice of wavelength in the visible range. In order to tune our experiment to a specific desired wavelength we make use of a nonlinear parametric amplifier (NOPA). We use a Spectra-Physics Spirit-NOPA to convert the near-IR output of the Spirit to a wavelength tunable from 650 - 900 nm and compressed to 20 fs, with a few hundred mW of total power. This conversion involves a number of non-linear processes, outlined here.

The input pump beam is split, the majority of the power undergoing frequency doubling to 520 nm in a β-Barium Borate (BBO) crystal. The remainder is focused into a sapphire crystal, generating broad-bandwidth supercontinuum white light. This is a highly nonlinear process, where an ultra-short pulse is heavily dispersed and spectrally broadened due to the interaction of effects such as self-phase modulation and filamentation. This creates an extended self-focusing region for nonlinear interaction and dispersion, resulting in broadband white light. The white light generation process can quickly cause damage in the substrate, thus it is an important experimental consideration to physically adjust the generation crystal's position every 6-8 hours.

The two beams are then used in an optical parametric amplification (OPA) process. This is a special case of difference-frequency generation, where two photons interacting in a non-

centrosymmetric crystal with large second-order susceptibility $\chi^{(2)}$ generate a third photon at the difference of input frequencies, satisfying conservation of energy $\omega_1 - \omega_2 = \omega_3$. This is mediated by a nonlinear polarization induced in the crystal by the strong photon electric field,

$$P = \chi^{(2)}_{12} E_1 E_2. \tag{3.1}$$

In the OPA process, a pump beam at frequency ω_p and a signal beam at frequency ω_s are mixed in a BBO crystal, down-converting photons at the pump frequency to the signal frequency and producing a third idler photon at ω_i. Energy is thus transferred from the pump to the signal, amplifying it. Again, these photons satisfy conservation of energy such that $\omega_p - \omega_s = \omega_i$. In this case the pump is the green 520 nm beam, and the signal is the broadband white light. The process is highly sensitive to the relative phases of input photons; by rotating the mixing crystal and adjusting the time delay we can selectively phase match the two beams, choosing a particular wavelength of the white light to amplify as a signal beam. This process of selectively amplifying a portion of the white light spectrum is known as the preamplification stage, and can enhance the signal beam power by a factor of up to 10^6 [24].

Following, the signal and pump enter the main amplification stage, undergoing the same process in a second BBO crystal to further amplify the power of the signal. Again, the crystal orientation and time delay between pump and signal beams are crucial to achieve appropriate phase matching and maximum power amplification. In ideal cases, the conversion efficiency of pump to signal and idler can exceed 30% [24]. The final stage of the OPA is a pulse compressor, using a multi-pass prism pathway to temporally compress the pulses to a bandwidth-limit of 20 fs. In our Spirit-NOPA, the best-case final power output after re-alignment is $300 - 400$ mW.

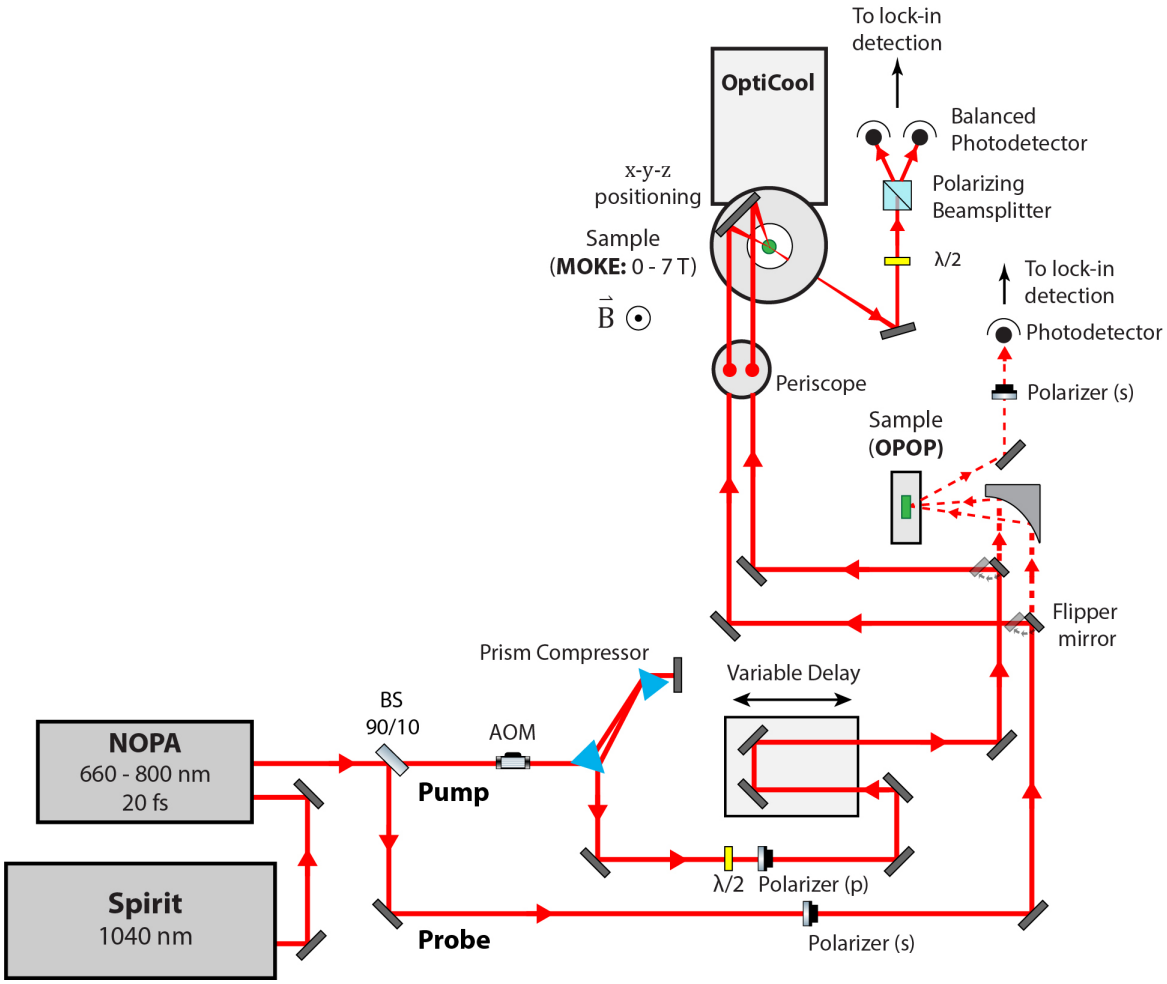

Figure 3.1: Diagram of the experimental setup used for OPOP and MOKE measurements. A set of flipper mirrors is used to swap between optical-pump optical-probe measurements (OPOP) in a standard cryostat, and magnetic field-dependent measurements in the OptiCool system.

3.2.3 Experimental Design and Detection Scheme

This section details the experimental setup and design, including the detection scheme. A diagram of the full experimental setup used in our optical pump-probe and magneto-optical Kerr measurements is shown in 3.1. Following the NOPA, pulses are split by a 90/10 beamsplitter into a pump and probe beam. The pump is modulated by a quartz acousto-optic modulator (AOM) at $f_{AOM} = f_{laser}/4$ (52 KHz), necessary for lock-in detection. The high modulation frequency yields a significant reduction in $1/f$ noise. Combined with the relatively high laser repetition

rate of 209 KHz, we have a highly sensitive experimental setup that can still deliver moderately energetic pulses. As the AOM is highly dispersive, it is followed by a pair of prisms for pulse compression. Here, pump pulses are also pre-chirped to account for dispersion from subsequent transmissive optics. Next, a polarizer ensures that the pump is fully polarized along either the *s* or *p*-direction, followed by a delay stage (Newport, 250 mm) that extends the pump path length relative to the probe, enabling a pump-probe time delay of up to 1 ns. Finally, focusing optics (a parabolic mirror or series of lenses) direct the beam to the sample in the cryostat. The probe path is simpler, essentially just containing a polarizer to cross-polarize the beam relative to the pump, and similar focusing optics. Typical spot sizes for the focused pump beam on the sample are on the order of 100 μm.

The probe beam reflected from the sample is then directed to a detection setup for measuring pump-induced changes in reflectivity. A pinhole and polarizer are used to eliminate pump scatter, and a series of lenses collimate and focus the beam to a size suitable for the small-area photodiode. Typical experiments are run in a single photodetector scheme which we have found to provide a better signal to noise ratio than balanced detection for moderate amplitude signals. The photodetector output is sent to an SR830 lock-in amplifier, which is locked to the AOM frequency of 52 KHz. The lock-in is a phase sensitive signal amplifier, isolating only the signal that is in phase with and centered at the modulation frequency, eliminating all other sources of high/low frequency noise. While the photodetector directly measures the probe intensity, it is the pump that is modulated at f_{AOM}. Thus the lock-in records only the changes in sample reflectivity caused by the pump, or the pump-induced ΔR. In addition, the signal is integrated with a specified time constant (typically 0.3 s) to further improve signal to noise. With the above, our experiment is capable of measuring relative changes in reflectivity of $\Delta R/R \approx 10^{-6}$.

Finally, the experiment is controlled and data recorded via custom built LabVIEW routine. The vast majority and base of this routine was developed previously by Verner Thorsmølle. However a significant amount of work was put into integrating this software with our hardware

and improving upon it's functionality. A routine designed specifically for standard optical-pump optical-probe and for magnetic-field dependent measurements were both developed.

3.3 Magnetic Field-Dependent Measurements

A system dedicated to measuring samples in a magnetic field was also developed. This has been an excellent resource for investigating magnetic dynamics using the magneto-optical Kerr effect (MOKE), and for studying the general optical response of materials in a magnetic field. MOKE physics is described below. Here we detail the experimental setup.

Magnetic field-dependent measurements are performed in a Quantum Design OptiCool cryostat. This is a closed loop system with a working temperature range from $1.7-400$ K and a continuously tunable magnetic field from $0-7$ T, capable of optical measurements in both reflection and transmission. The experimental setup and beam path are shown in Fig. 3.2. The work performed on $GdTiO_3$ was measured in reflection, necessitating a series of optics on a breadboard raised from the cryostat to prevent excessive forces in high magnetic fields. Still, it was found that fields in excess of $\sim$1 T introduced excess noise and artifacts to the data, so care should be taken when measuring in much larger magnetic fields. Before the cryostat, a polarizer on both the pump and probe path ensures the pulses are orthogonally polarized. After, light is coupled into the cryostat with a periscope and a 1 m focal length lens on a series of translation stages for positional control. The magnetic field is aligned perpendicular to the table, along the optical axis of the cryostat and out of plane from the sample.

After reflection from the sample, a pickoff mirror directs the linearly-polarized probe beam to the MOKE detection setup. In this geometry we measure changes in the polarization of light due to interaction with the magnetic moment of a sample in an applied field. The polarizer is removed from the detection setup and replaced with both a half-wave plate ($\lambda/2$) and a Wollaston prism. The half-wave plate is set to a rotation of $\pi/8$ from the fast axis, such that a

Figure 3.2: The experimental setup for magnetic field-dependent measurements. The system is a Quantum Design OptiCool closed-loop cryostat. Measurements are performed in reflection, coupled into the top of the cryostat with a raised periscope assembly. The magnetic field is out of plane. Transmission measurements through the side windows are also possible.

linearly polarized input beam will become circularly polarized, with an equal *s* and *p*-polarization amplitude. The Wollaston prism is a polarizing beam splitter that separates light into two purely polarized linearly orthogonal components. In this way it decomposes the now-circularly probe beam into it's component *s* and *p*-polarizations. These two orthogonally polarized beams are directed to a balanced photodiode, which measures the relative and absolute intensity of each. With the pump blocked, minor rotational corrections are made to the half-wave plate to ensure that the photodetector is well balanced. In this detection geometry, very small photoinducd changes in probe polarization result in a relative change of *s*/*p*-polarization amplitude after the half-wave plate, which is captured by the balanced detector, sent to the lock-in, and used to record the Kerr

rotation.

3.4 Magneto-Optical Kerr Spectroscopy

3.4.1 Physics of the Magneto-Optical Kerr Effect

The magneto-optical (MO) effect offers a method of examining the magnetic properties of a material with light. Using a femtosecond pulsed laser setup, this can be extended to measuring time-resolved spin and spin-related dynamics of optically excited states. A polarized photon transmitted or reflected from a sample with a non-zero magnetic anisotropy will incur a change in polarization state, a fact which forms the basis of magneto-optic spectroscopy.

A macroscopic description of magneto-optical effects involves the interaction between the electric field of light and the motion of electrons in a material. It is easiest to consider the case with circularly polarized light. This extends to the case of linearly polarized light, which can be equivalently described by the superposition of two circularly polarized beams. Right-circularly polarized (RCP) light will drive electrons into right circular motion, with an orbital radius dependent on the restoring force of the medium. Left-circularly polarized (LCP) light will drive electrons into left circular motion, with an equal radius. In the presence of a magnetic field, the RCP and LCP orbits expand or contract due to the Lorentz force, which alters the absorption and phase velocity of the propagating light and results in a change in polarization [24].

Mathematically this MO effect can be described by the dielectric tensor, which generally determines the optical response of a material. The dielectric function was presented in Section 2.1, and here is extended to it's tensor form to characterize a material with axial differences. Rather than a fully generalized description of the dielectric response, we will focus on a geometry relevant to our experiment, with a uniform magnetic field $\mathbf{H}$ directed along the z-axis. The

dielectric tensor becomes:

$$\widetilde{\varepsilon} = \begin{pmatrix} \varepsilon_{xx} & \varepsilon_{xy} & 0 \\ -\varepsilon_{yx} & \varepsilon_{yy} & 0 \\ 0 & 0 & \varepsilon_{zz} \end{pmatrix}, \tag{3.2}$$

where $\varepsilon_{xx} = \varepsilon_{yy} = \varepsilon_{zz}$ for an isotropic material. The off-diagonal components are associated with MO effects, and to first order are proportional to the sample magnetization **M** such that

$$\varepsilon_{xy}(M,\omega) = -\varepsilon_{yx}(-M,\omega) \propto M. \tag{3.3}$$

These off-diagonal terms are the result of time-reversal symmetry breaking, present in any magnetically ordered material and a consequence of the spin operator **S** changing sign when acted upon by the time-reversal operator. Thus, a transformation of the applied field's sign $H \rightarrow -H$ will transform the off-diagonal terms antisymmetrically. The diagonal terms in the dielectric tensor are symmetric under time-reversal, implying symmetric changes with field reversal. This difference is fundamental to the MO response. The off-diagonal dielectric elements quantify the different response to RCP and LCP light that was described above. The complex dielectric function determines the polarization-dependent index of refraction, given by:

$$\varepsilon_{\pm} = \varepsilon_{xx} \pm i\varepsilon_{xy} = (n_{\pm} + ik_{\pm})^2. \tag{3.4}$$

Due to propagation differences based on the complex index of refraction, light of any polarization transmitted or reflected from the sample will have some conversion from RCP to LCP or visa-versa. The interaction of the real part n results in a phase shift and subsequent rotation of polarization, while the imaginary part k results in absorption and ellipticity, both of which are characteristic to the MO response.

Microscopically, there are two primary factors affecting the off-diagonal dielectric components and therefore the MO response; the spin exchange interactions (i.e. inherent magnetism)

and spin-orbit coupling (SO). The SO interaction relates the motion of a charge to it's spin. This introduces a term to the hamiltonian of the form:

$$H_{SO} = (\hbar/4m^2c^2)\vec{\sigma} \cdot (\nabla V \times \vec{p}), \tag{3.5}$$

based on momentum $\vec{p}$, the electric potential ∇V, and the effective magnetic field (inherent and applied) [25]. In a non-magnetic material the equal number of spin up and down electrons cancels the effect. In a magnetic material, however, the effect is nonzero, leading to energy level splitting dependent upon electron motion and spin. This ultimately results in a different response to the electric field of RCP and LCP light, the differences in transition strength and absorption forming the basis of the MO effect.

3.4.2 MOKE in Experiment

In an experimental measurement, the quantities we wish to observe are the rotation of polarization and change in relative RCP/LCP amplitude (ellipticity). Most magnetic materials are metallic and strongly absorb light, so we will focus on a reflective geometry like that used in our experiments. We can define a complex MOKE angle that describes the Kerr rotation θ_k and Kerr ellipticity η_k, given by

$$\widetilde{\Theta}_k = \theta_k + i\eta_k. \tag{3.6}$$

The question then becomes how to define the Kerr rotation and ellipticity as a function of observable quantities. In an optics experiment, this is typically the change in reflectivity of the sample after photoexcitation. Consider the reflection coefficient, defined as the ratio of the reflected and incident electric field,

$$r = \frac{E^r}{E^i}, \tag{3.7}$$

where r and i denote the reflected and incident field, respectively. Because polarization is crucial we can define a similar reflection coefficient for both s and p-polarized light, r_{ss} and r_{pp}. We then use a Jones Matrix notation, which treats polarized light as a 2-dimensional Jones vector, to describe the incoming and outgoing electric fields. Reflection from a simple, non-magnetic sample is represented as

$$E^r = RE^i \tag{3.8}$$

$$\begin{pmatrix} E_s^r \\ E_p^r \end{pmatrix} = \begin{pmatrix} r_{ss} & 0 \\ 0 & r_{pp} \end{pmatrix} \begin{pmatrix} E_s^i \\ E_p^i \end{pmatrix} = \begin{pmatrix} r_{ss}E_s^i \\ r_{pp}E_p^i \end{pmatrix}, \tag{3.9}$$

where R is the full reflection matrix composed of Fresnel coefficients r_{ij} [26]. In this notation, we see that it is the diagonal elements of the reflection matrix responsible for simple linear reflection at a given polarization. For a magnetic sample in an external field, however, there is a conversion of polarization from s to p and visa-versa as described in the preceding section. This can be represented by off-diagonal terms in the reflection matrix, given by

$$r_{sp} = \frac{E_s^r}{E_p^i} \tag{3.10}$$

$$r_{ps} = \frac{E_p^r}{E_s^i}. \tag{3.11}$$

Adding these off diagonal terms to the reflection matrix, the total reflected electric field becomes [26]:

$$\begin{pmatrix} E_s^r \\ E_p^r \end{pmatrix} = \begin{pmatrix} r_{ss} & r_{sp} \\ r_{ps} & r_{pp} \end{pmatrix} \begin{pmatrix} E_s^i \\ E_p^i \end{pmatrix} = \begin{pmatrix} r_{ss}E_s^i + r_{sp}E_p^i \\ r_{ps}E_s^i + r_{pp}E_p^i \end{pmatrix}, \tag{3.12}$$

As the MO signal is the result of conversion from one polarization to another, based on the off-diagonal elements, the Kerr rotation and ellipticity for a given polarization are given by a ratio of reflection components [27]:

$$\widetilde{\Theta}_s = \theta_s + i\eta_s = \frac{r_{ps}}{r_{ss}}, \tag{3.13}$$

$$\widetilde{\Theta}_p = \theta_p + i\eta_p = \frac{r_{sp}}{r_{pp}}. \tag{3.14}$$

Using this representation, we can calculate the Kerr rotation and ellipticity from experimentally observable quantities, using the relative reflected intensity of light from the sample. The full analysis is shown below in Sec. 3.4.3. Before that, it is important to discuss the geometry of the experiment.

Measurement of the Magneto Optical Kerr Effect is highly dependent on geometry, and depends on the relative orientation of the applied magnetic field and the electric field of incident light. There are three standard geometries for MOKE experiments: polar, longitudinal, and transverse. In the polar geometry, the applied field is perpendicular to the sample surface and parallel to the light's plane of incidence; in longitudinal, the magnetic field is parallel to both the sample surface and plane of incidence; and in transverse, the field is perpendicular to the plane of incidence. In practice, the polar geometry is the only that can be used to study reflection at normal incidence to the sample, and thus is used in our experiment and the following analysis. Fig. 3.3(a) displays a schematic of the polar geometry in our experiment on $GdTiO_3$. The electric field of the incident light is directed along the x-direction (s-polarized), and the applied field H along the z-direction, out-of-plane. Upon interaction with the magnetized sample, electrons oscillate along the E-field direction (x) and are acted upon by a Lorentz force $F_L \propto \vec{v} \times \vec{H}$ in the y-direction. This generates a new p-polarized component of the field along the y-direction, rotating the polarization of the total reflected field by a small angle. This is shown in Fig. 3.3(b), where the original s-polarized component E_s^r and the newly generated p-polarized component of the electric field E_p^r

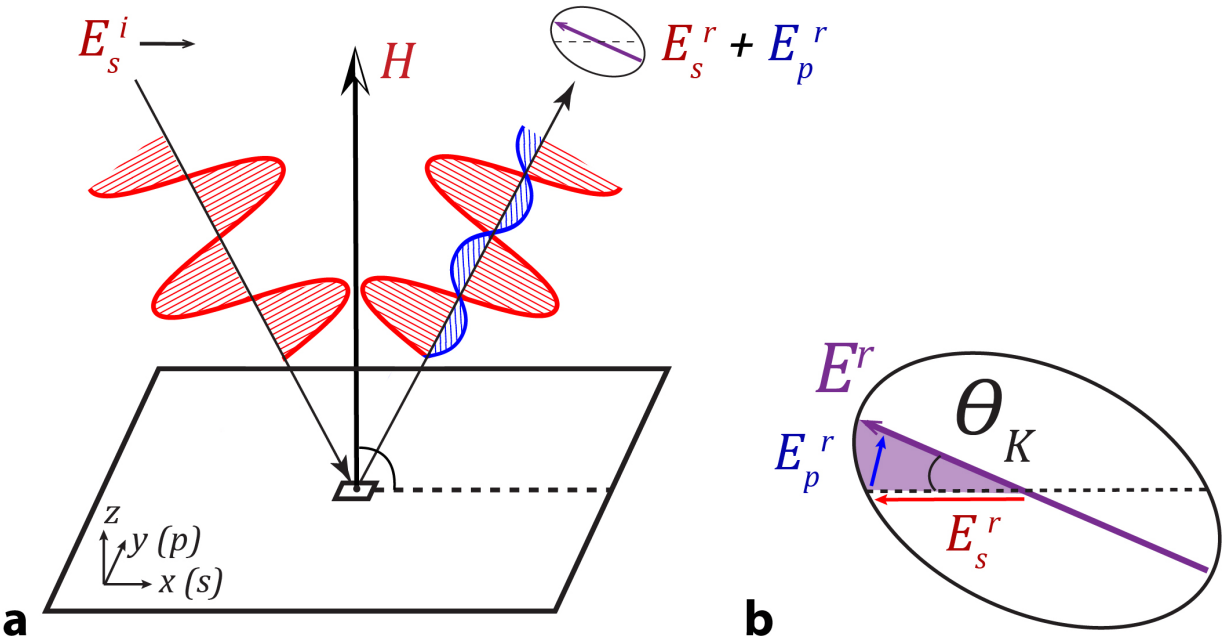

Figure 3.3: (a) The polar Kerr geometry used in our experiment. The magnetic field is perpendicular to the sample surface, and the light parallel to the plane of incidence. Incident light is *s*-polarized. Upon reflection, the polarization of light is rotated as a *p*-polarized component is generated. (b) detail of the reflected vector components, indicating that the total reflected beam is composed of the original *s*-polarized component and a new *p*-polarized component.

sum to the total reflected field E^r with a Kerr rotation of θ_k.

For this geometry, with the incident electric field directed along x and the field along z, the complex MOKE angle can be quantified in terms of dielectric tensor elements as

$$\widetilde{\Theta}_s = \theta_s + i\eta_s = \frac{i\varepsilon_{xy}}{\sqrt{\varepsilon_{xx}(\varepsilon_{xx}-1)}}. \tag{3.15}$$

A full derivation can be found in reference [28]. Because ε_{xy} is proportional to the sample magnetization M, the Kerr rotation and ellipticity are as well, and both become a probe for magnetism. In the following section, we detail the calculations used to extract the Kerr rotation angle from measurable data.

3.4.3 Analysis: Jones Matrix Formalism

Here we show the analysis necessary to calculate a Kerr rotation from experimental data, using the Jones matrix formalism. This is an important step, as it is specific to the optics used in the experiment and is necessary to ensure that the signal measured genuinely represents magnetic dynamics. The Jones formalism, or Jones Calculus, represents a method of quantitatively analyzing polarized light and it's interaction with various optics throughout the experiment [29]. This was briefly introduced in the previous section, where a 2x1 Jones vector is used to describe the polarization state of a photon, and is expanded upon here. In addition to the Jones vector for light, 2x2 Jones matrices are used to describe the effect of optical elements on the passing photon. This is a 2-state basis, where the two orthogonal linear polarization states of light are represented by the Jones basis vectors:

$$E_s = \begin{bmatrix} 1 \\ 0 \end{bmatrix}, \quad E_p = \begin{bmatrix} 0 \\ 1 \end{bmatrix}. \tag{3.16}$$

Here we will use components s and p referring to our experimental geometry in Fig. 3.3(a). Again, this is a polar MOKE geometry where z is the out-of-plane direction in reference to the sample surface and the magnetic field direction. After reflection from the sample, the only transmissive optics the probe beam passes through are a half-wave plate and a polarizing beamsplitter known as a Wollaston prism. Each of these is accounted for by it's own unique Jones matrix, and the total effect of all interactions is described by the product. These are multiplied in reverse order, such that the output is on the left side of the equation, with the last optic as the fist matrix product and so on. Using this notation, we can write the output electric field recorded at the detector as follows:

$$E_{Det} = J_{wol} * J_{\frac{\lambda}{2}} * R * E_{in}. \tag{3.17}$$

Where J_{wol} is the Jones matrix of the Wollaston prism, $J_{\frac{\lambda}{2}}$ is the Jones matrix of the half-wave plate, and R is the reflection matrix at the sample. The Wollaston prism can be ignored, as it only splits light into constituent polarizations and has no other effect on the polarization. Substituting the appropriate values [30] [31], we have

$$\begin{pmatrix} E_s^r \\ E_p^r \end{pmatrix} = \begin{pmatrix} cos2\theta & sin2\theta \\ sin2\theta & -cos2\theta \end{pmatrix} \begin{pmatrix} r_{ss} & r_{sp} \\ r_{ps} & r_{pp} \end{pmatrix} \begin{pmatrix} E_s^i \\ E_p^i \end{pmatrix} \tag{3.18}$$

For polar MOKE at normal incidence, the symmetry allows us to simplify the Fresnel coefficients $r_{pp} = -r_{ss}$ and $r_{sp} = r_{ps}$ [32]. Our light is s-polarized, so $E_p^i = 0$, and we set the wave plate to $\pi/8$ to yield equal intensity of s and p-polarized light for balanced detection at equilibrium conditions. Substituting these values yields

$$\begin{pmatrix} E_s^r \\ E_p^r \end{pmatrix} = \frac{\sqrt{2}}{2} \begin{pmatrix} 1 & 1 \\ 1 & -1 \end{pmatrix} \begin{pmatrix} r_{ss} & r_{ps} \\ r_{ps} & -r_{ss} \end{pmatrix} \begin{pmatrix} 1 \\ 0 \end{pmatrix} \tag{3.19}$$

$$\begin{pmatrix} E_s^r \\ E_p^r \end{pmatrix} = \frac{\sqrt{2}}{2} \begin{pmatrix} r_{ss} + r_{ps} \\ r_{ss} - r_{ps} \end{pmatrix} \tag{3.20}$$

Now, we use the fact that the intensity of light recorded at the detector is equal to the square of the field, $I_n = |E_n^2|$. The Kerr intensity I_K is the balanced photodetector reading, the s-polarized intensity minus p-polarized. Substituting our expression for the electric field from Eq. 3.20, the

Kerr intensity becomes

$$\begin{aligned} I_{Kerr} &= I_s - I_p \\ &= |E_s^2| - |E_p^2| \\ &= \frac{1}{2}(|r_{ss}+r_{ps}||r_{ss}+r_{ps}|^* - |r_{ss}-r_{ps}||r_{ss}-r_{ps}|^*) \\ &= r_{ss}r_{ps}^* + r_{ps}r_{ss}^* \\ &= |r_{ss}|^2(\frac{r_{ps}^*}{r_{ss}^*} + \frac{r_{ps}}{r_{ss}}) \\ &= |r_{ss}|^2(\Theta + \Theta^*) \\ &= 2R\theta_s \end{aligned} \tag{3.21}$$

where we use the definition of the MOKE angle Θ_s given in Eq. 3.14 and define $R = |r_{ss}|^2$. The photoinduced differential Kerr intensity is then

$$\Delta I_{Kerr} = 2R_0\Delta\theta(t) + 2\Delta R(t)\theta_0. \tag{3.22}$$

In our experiment the magnitude of the first term is much larger than the second, which can be dropped [28] to yield

$$\Delta I_{Kerr} = 2R_0\Delta\theta(t). \tag{3.23}$$

Next, we can define the total intensity of light on the detector I_{total} as

$$\begin{aligned} I_{total} &= I_s + I_p \\ &= |E_s^2| + |E_p^2| \\ &= |r_{ss}|^2 + |r_{ps}|^2 \\ &= |r_{ss}|^2(1-\Theta^2) \\ &= |r_{ss}|^2(1-\varepsilon^2-\eta^2) \\ &\cong R_0 \end{aligned} \tag{3.24}$$

where the MO quantities θ and η are small, and to first order their squares can be dropped. Finally, the photoinduced change in Kerr rotation $\Delta\theta_k$ is given by combining Eq.'s 3.21 and 3.24

$$\frac{\Delta I_{Kerr}}{2I_{total}} = \frac{I_s - I_p}{2(I_s + I_p)} = \Delta\theta_k. \tag{3.25}$$

This gives us an expression for the Kerr rotation in terms of the two measurements at the balanced photodiode, and says that θ_k is proportional to the change in relative *s* and *p*-polarized light intensity. This analysis verifies that the measurement records real magnetization dynamics. To further ensure this, we take an additional step and measure all Kerr rotations at both +H and -H applied fields, taking the difference to eliminate any signal that does not depend on H and the sample magnetization M. The final reported Kerr rotation in our work is defined as

$$\Delta\theta_{reported} = \Delta\theta_k(+H) - \Delta\theta_k(-H). \tag{3.26}$$

This ensures that the Kerr signal we measure is a probe of genuine magnetic dynamics in the sample.

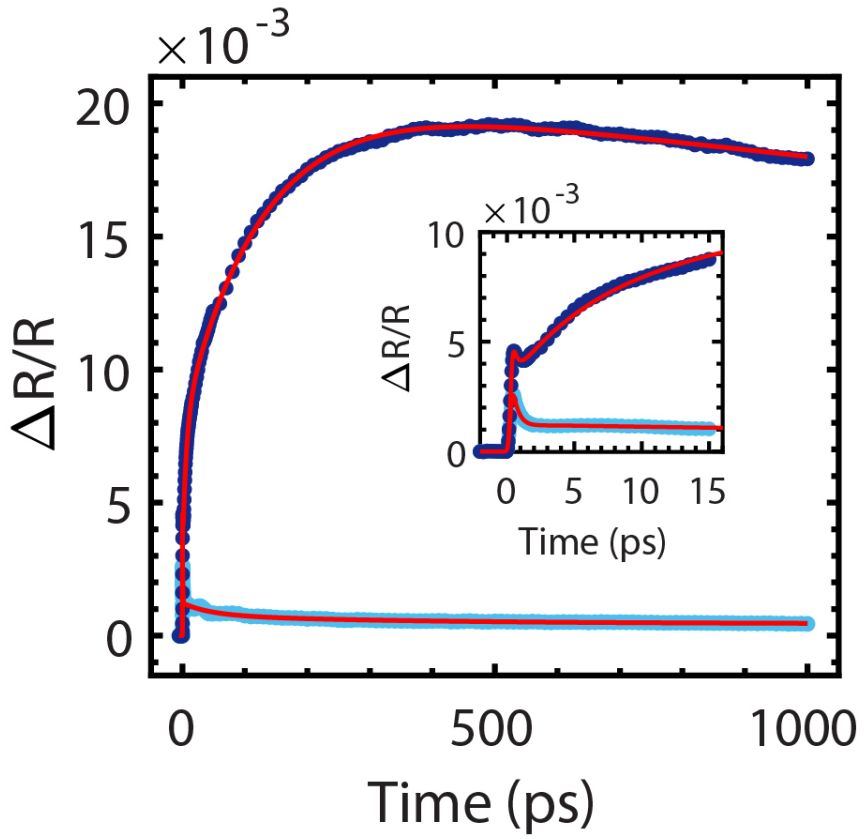

Figure 3.4: A Typical time-resolved reflectivity $\Delta R/R$ signal taken from a pump-probe experiment, at two different temperatures. The red lines represent exponential fits to the data. The inset shows a detailed view of the first 15 ps of data, where the rise time and first few time constants are clearly visible.

3.5 Data Analysis - Fitting

An important step in the analysis of experimental data is fitting - computing a mathematical model of the time evolution of the signal. From this model one can extract useful information, such as the time constants characteristic to the rise and decay of the excited state. In addition, it allows subtraction of the average signal to reveal more subtle physics, such as oscillatory phonon modes. In this section we describe the process used to evaluate and fit the data retrieved from a our time-resolved pump-probe experiments.

A typical time-resolved reflectivity $\Delta R/R$ signal taken from experimental measurements on $GdTiO_3$ is shown in Fig. 3.4. Two different temperatures are marked in different shades of

blue, while the red lines represent exponential fits to the data. Prior to the fitting step, we subtract the average background from before $t = 0$ to create a zero baseline for meaningful comparison of data. Following this, the data is run through a home built MATLAB program. A significant amount of time has been spent developing a robust and efficient fitting routine, capable of quickly applying fits to complex data through a wide series of temperatures. An overview is given here, with details and user instructions in Appendix A.

The fitting routine makes use of of the Nelder-Meade optimization algorithm to converge on a best-fit solution given a series of starting points. To begin, the functional form of the fit must be supplied. This can be configured arbitrarily but is typically a sum of n exponentials with a constant offset, of the form

$$\frac{\Delta R}{R} = (C + A_1 e^{-t/\tau_1} + ... + A_m e^{-t/\tau_m}) * erfc((t - t_0)/B), \tag{3.27}$$

where C is the constant offset, A_m is the exponential amplitude, and τ_m is the time constant. *erfc* is the complementary error function which encapsulates the quick rise time near $t = 0$, and is given by

$$erfc(x) = \frac{2}{\pi} \int_x^\infty e^{-t^2} dt \tag{3.28}$$

This represents the start of the signal when the pump is overlapped in time with the probe. There are a total of n fit parameters to be optimized. With a functional form defined, the user supplies the MATLAB program with a best guess of the initial fit parameters, as well as a maximum and minimum bound for each parameter. From the given bounds, an array of initial conditions is generated that fully spans the parameter space. Using this array and the user-defined best guess the Nelder-Meade algorithm is applied, a simplex triangulation method which ranks and attempts new solutions to cover a wide range of the n-dimensional parameter space and converge on the best solution. A simplex with n+1 vertices is formed (n-triangle, essentially), where each of the

vertices is an n-dimensional array with initial conditions for the fit. This gives us n+1 potential solutions to the fit, each of which is evaluated for goodness of fit based on the sum residual and R^2. It is R^2 which we attempt to minimize. The Nelder-Meade algorithm then follows the series of steps outlined below [33]:

1. **Ordering**

   The n+1 solutions to the fit are ranked in ascending order according to goodness of fit, with the minimum R^2 first. List these solutions as x_n, which solve the fit equation $f(x)$ such that $f(x_1) < f(x_2) < ... < f(x_{n+1})$.

2. **Centroid**

   Calculate the centroid, or mean, x_0 of all solutions, excluding the worst (x_{n+1}).

3. **Reflection**

   Calculate the reflection point x_r , reflecting the x_{n+1} vertex of the simplex about the centroid point x_0. This reflection moves the simplex away from x_{n+1}, the region with the worst solution. The reflected vertex is given by computing $x_r = x_0 + \alpha(x_0 - x_{n+1})$, where α is the user-defined reflection amplitude (typically close to 1).

   The following step depends on the ranking of x_r. If the reflected vertex is a better solution than the second worst, but not the best, such that $f(x_1) \leq f(x_r) < f(x_n)$, then we replace the worst point x_{n+1} with x_r and return to step 1.

4. **Expansion**

   If the reflected vertex is the best solution ($f(x_r) < f(x_1)$), then we expand along the reflected direction in an attempt to reach a more optimal region of parameter space. The expanded point is calculated as $x_e = x_0 + \gamma(x_r - x_0)$, with γ the expansion parameter > 1.

   If $f(x_e) < f(x_r)$, i.e. the expanded vertex is a better solution than the reflected, then replace

the worst solution x_{n+1} with x_e and return to step 1. Otherwise, if $f(x_r) < f(x_e)$, replace x_{n+1} with x_r and return to step 1, repeating the process with a new simplex.

5. **Contraction**

   If the reflected vertex x_r is worse than the second-worst solution, $x_n < x_r$, then we have overshot the optimal solution region. Now, contract the size of the simplex by computing the contracted vertex $x_c = x_0 + \rho(x_{n+1} - x_0)$ with $0 \leq \rho \leq 0.5$.

   If $f(x_c) < f(x_{n+1})$, i.e. the contracted vertex is a better solution than the worst solution, then replace the worst solution x_{n+1} with x_c and return to step 1.

In this manner the process is repeated until some termination condition is reached. This may be defined as an R^2 below some threshold value, but in practice this varies between data sets and it is sufficient to terminate after a fixed number of iterations. At this point, the best solution x_1 is an excellent fit to the data.

A major advantage of this fitting routine is the range of solutions which can be tested. An exceedingly accurate initial guess is not needed, so long as the bounds of each parameter can be defined properly. A solution is converged upon fairly quickly, and in many cases few or no adjustments are needed for a range of data from 10 K to room temperature. One must always check that the number of fit parameters, or exponential terms, is sufficient, and that the fit is not over or underparameterized. An underparameterized fit can be checked by eye and will not appear as a good fit, while determining overparameterization is more subtle. The coefficient covariance matrix can be checked, where larger elements indicate higher covariance and thus chance that the fit parameters are mutually dependent. In general, the least number of fitting terms should be used, while avoiding underparameterization. Many of the results in the proceeding sections are based on the fits from this routine.

Chapter 4

Influence of spin and orbital fluctuations on Mott-Hubbard exciton dynamics in $LaVO_3$ Thin Films

4.1 Abstract

In this section we present optical pump-probe results on Mott-insulator $LaVO_3$. Recent optical conductivity measurements reveal the presence of Hubbard excitons in certain Mott insulators. In light of these results, it is important to revisit the dynamics of these materials to account for excitonic correlations. We investigate time-resolved excitation and relaxation dynamics as a function of temperature in perovskite-type $LaVO_3$ thin films using ultrafast optical pump-probe spectroscopy. $LaVO_3$ undergoes a series of phase transitions at roughly the same critical temperature $T_C \cong 140\ K$, including a second-order magnetic phase transition (PM $\rightarrow$ AFM) and a first-order structural phase transition, accompanied by *C*-type spin order (SO) and *G*-type orbital order (OO). Ultrafast optical pump-probe spectroscopy at 1.6 eV monitors changes in the spectral weight of the Hubbard exciton resonance which serves as a sensitive reporter of

spin and orbital fluctuation dynamics. We observe dramatic slowing down of the spin, and orbital dynamics in the vicinity of $T_C \cong 140$ K, reminiscent of a second-order phase transition, despite the (weakly) first-order nature of the transition. We emphasize that since it is spectral weight changes that are probed, the measured dynamics are not reflective of conventional exciton generation and recombination, but rather are related to the dynamics of Hubbard exciton formation in the presence of a fluctuating many-body environment.

4.2 Introduction

Transition-metal oxides (TMO) display a wide range of interesting magnetic and electronic properties, owing to strong electron correlation and competition between charge, spin, lattice, and orbital degrees of freedom. The interplay of these interactions makes for rich and diverse physics, with relevant phenomena including colossal magnetoresistance, metal-insulator transitions, ferroelectricity, and high-T_c superconductivity [1, 3]. The rare-earth vanadates RVO_3 (R = rare-earth or Y) are a class of TMO displaying many of these features. Specifically, these materials are Mott-Hubbard (MH) insulators with highly coupled spin, charge, and orbital degrees of freedom, making them an ideal prototypical system for studying the interplay of some of the most fundamental properties of matter [34, 35, 36, 37].

Recently, optical conductivity measurements and DFT/DMFT calculations indicate that Hubbard excitons (HE) play an important role in the physics of vanadates [38, 39, 40]. The lowest lying peak in σ_1 ($\sim$1.8 eV), previously attributed to a $3d$ multiplet, appears to belong instead to an excitonic resonance. Further, the formation of these excitonic signatures appear to be strongly influenced by the presence of spin and orbital order. In general, there remain significant open questions regarding the physics of MH excitons in quantum materials. Under what conditions do these excitons form, what are their characteristic timescales, and what degrees of freedom influence their dynamics? Advances in theory and experimental techniques have begun to address

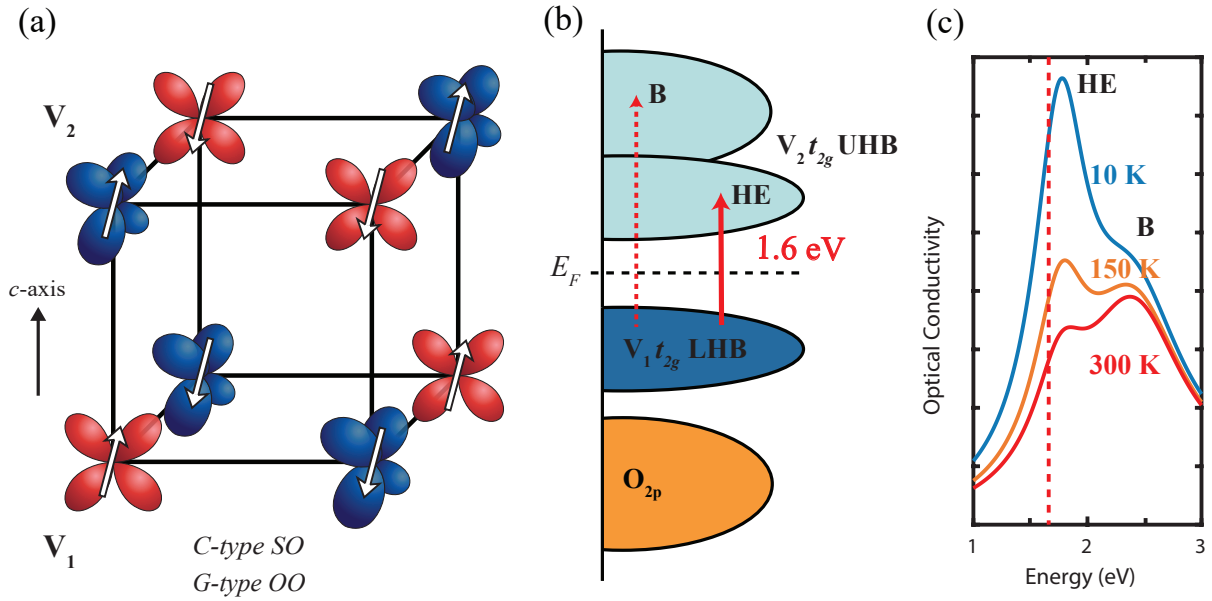

Figure 4.1: (a) Diagram of the C-type spin and G-type orbital order configuration in $LaVO_3$. The spins on d_{zx} and d_{yz} orbitals, shown as white arrows, are slightly canted from the c-axis. (b) Depiction of the density of states near the Fermi level, showing the photoexcitation process at 1.6 eV from the lower Hubbard band (LHB) to the upper Hubbard band (UHB). An electron from a t_{2g} orbital in the LHB on Vanadium atom V_1 is promoted to a t_{2g} orbital in the UHB on V_2. (c) Depiction of the c-axis optical conductivity evolution with temperature, reproduced from [11]. Peak HE corresponds to the excitonic resonance in the vicinity of the MH gap, and peak B an excitation from LHB $\rightarrow$ UHB (consisting of well separated quasiparticles). The ratio of peak HE to peak B grows drastically below the ordering temperature at T_C = 140 K, indicating the importance of spin and orbital order upon the exciton spectral weight. The red dotted line indicates the laser photoexcitation energy.

these questions, indicating for example that the recombination rates are proportional to the MH gap and mediated by magnon emission [41, 42, 43]. Ultrafast optical spectroscopy is a technique particularly well-suited to furthering our understanding of this field, and has been used extensively to study ultrafast dynamics in many MH insulators, including cuprates [44, 45, 46], manganites [47, 48], and TaS_2 [49].

The relative simplicity of the vanadates as d^2 materials, along with coupled spin and orbital order, makes them an excellent platform in which to study HE dynamics, particularly in relation to the spin and orbital degrees of freedom. In this work we focus on lanthanum vanadate $LaVO_3$ (LVO). LVO has a perovskite-type lattice and is a $3d^2$ Mott-Hubbard insulator, with

both d-electrons occupying the t_{2g} band. Strong quantum orbital fluctuations, enhanced by a highly frustrated Kugel-Khomskii superexchange [50], play a role in stabilizing the t_{2g} energy even at room temperature, resulting in fairly equal occupation of the d_{xy}, d_{yz}, and d_{zx} orbitals [51, 52, 34]. Upon cooling, this degeneracy is broken as LVO undergoes a structural phase transitions at T_C = 140 K that, in turn, modifies the spin and orbital order. A first-order structural phase transition from an orthorhombic *Pbnm* lattice to monoclinic $P2_1/b$ [10, 11] is accompanied by G-type Jahn-Teller and $GdFeO_3$-type distortion. As shown in Fig. 4.1(a), this lifts the t_{2g} orbital degeneracy and results in G-type orbital ordering with an always occupied d_{xy} orbital and alternatingly occupied d_{yz} and d_{zx} orbitals in all lattice directions [52, 11, 53, 40]. This orbital configuration subsequently induces an antiferromagnetic exchange interaction between sites in the *ab* plane, resulting in a second-order transition from paramagnetic to C-type antiferromagnetic order with slightly canted spins [52].

The degree of spin and orbital order also affects the optical properties of LVO, which exhibits a strong anisotropy in the optical conductivity. While the spectrum is almost entirely temperature independent for $\boldsymbol{E} \perp c$, for $\boldsymbol{E} \parallel c$ there is a large transfer of spectral weight from high (> 3.5 eV) to low ($\sim$2 eV) energy as the temperature is lowered, as shown in Fig. 4.1(c) (data reproduced from [11]). Furthermore, a splitting of the 2 eV region is observed, separating the low energy optical conductivity into peak HE at 1.8 eV and peak B at 2.4 eV. Both correspond to an excitation across the MH gap, associated with d_{yz}-d_{yz} or d_{zx}-d_{zx} transitions between adjacent V^{3+} sites along the *c*-axis [11, 54], resulting in a high-spin excited state. While peak B represents a single particle excitation consisting of a well separated particle and hole, peak HE reflects the Hubbard exciton, with the peak separation proportional to the HE binding energy [39, 40]. This distinction is clarified in Fig. 4.1(b), with the 1.6 eV red arrow indicating our experimental pump-probe energy at the HE peak (as described in greater detail below). As peak HE lies above the MH gap [55], it is not a truly bound state. Rather, it is an excitonic resonance within the continuum, comprised of a weakly bound state between an excited d^3 state in the upper Hubbard

band and a d^1 state in the lower Hubbard band [38, 39].

It is of particular importance to note the role of spin and orbital order in Hubbard exciton dynamics. In the following, we refer to the photoexcited quasiparticle as a "double occupancy" (DO), but note that it is composed of two half-filled d_{yz} and d_{zx} orbitals, each with a single electron, and not a traditional doublon. Exciton formation in semiconductors is generally driven by a lowering of the Coulomb energy, but in an antiferromagnetic Mott-Hubbard system is governed by the kinetic energy. Hopping of a single hole or DO on the AFM background disrupts the local spin order, leaving a trace of disordered spins behind. As each step requires more energy than the last due to the compounding magnetic frustration, motion of a bare DO or hole is hindered and the kinetic energy reduced. However, moving as a pair preserves spin order, so a spinless bound exciton may freely move through the lattice, thereby gaining kinetic energy and becoming the energetically favorable state [43, 56]. A similar argument may be made for the motion of holes in an antiferro-orbital ordered background (as in LVO) where motion of the hole or DO leaves a trace of misaligned orbitals [57]. Indeed, static optical conductivity measurements have shown the influence of orbital order in Hubbard exciton formation in vanadates such as YVO_3, $GdVO_3$, and $CeVO_3$ [39]. In addition, time-resolved optical conductivity measurements on YVO_3 indicate the role of spin order/disorder in exciton dynamics [38].

It follows that optical measurements tuned near the excitonic peak at 1.8 eV serve as a highly sensitive probe of the coupled spin and orbital order. In the present work we carry out measurements using femtosecond optical pump probe spectroscopy in the vicinity of the HE resonance in epitaxial $LaVO_3$ thin films grown on $SrTiO_3$ to monitor spin and orbital dynamics. The various processes involved in excitation and recovery have unique intrinsic timescales, including spin-lattice coupling on the order of < 10 ps and recovery of spin/orbital order in $>$ 500 ps, allowing us to disentangle interacting degrees of freedom and observe how they change in different phases. In doing so we observe a large anomalous slowdown in the dynamics near the spin and orbital ordering phase transition, attributable in part to the influence of a highly

fluctuating spin/orbital background upon the presence of Hubbard excitons.

4.3 Methods

The $LaVO_3$ sample studied is a $\sim$50 nm thin film grown by hybrid molecular beam epitaxy on a (001) $SrTiO_3$ substrate. X-ray diffraction measurements have confirmed that the LVO film is coherently strained to the substrate. The film is slightly compressively strained, with an out of plane lattice parameter of 3.951 Å and in-plane lattice parameter of 3.905 Å, yielding an epitaxial strain of $c/a = 1.012$. The ultrafast optical measurements were made using a Spectra-Physics Spirit 200 kHz 1040 nm Yb-based hybrid-fiber laser coupled to a nonlinear optical parametric amplifier. The amplifier outputs $\sim$20 fs pulses at 770 nm (1.61 eV), which are split, cross-polarized (pump *s*-polarized, probe *p*), and used as degenerate pump and probe beams in a reflective geometry. The film grows with the *c*-axis in plane and the signal does not change with rotation of the sample, suggesting it is polycrystalline in nature and that the excitation (and probing) is in part $\boldsymbol{E} \parallel c$. We used a low pump fluence of 60 μJ/cm^2 to ensure that we were in the linear excitation regime. Measurements at a fluence of 20 μJ/cm^2 show no change in the dynamics in comparison to the 60 μJ/cm^2, indicating that the laser heating is small. The laser energy of 1.61 eV is near the HE peak in the optical conductivity, as discussed above [Fig. 4.1(c)]. Photoexcitation at this wavelength corresponds to an inter-site V^{3+} *d*-*d* transition. In the orbitally ordered state this involves electron transfer between d_{yz}-d_{yz} or d_{zx}-d_{zx} orbitals on adjacent vanadium sites along the *c*-axis [53], as shown in Fig. 4.1(b). The formation of Hubbard excitons is highly sensitive to spin and orbital order (e.g. the spectral weight of the HE peak in Fig. 4.1(c) decreases with increasing temperature because of such spin and orbital fluctuations). Therefore, by measuring changes in the reflectivity after photoexcitation as a function of pump-probe delay time (arising from photoinduced HE spectral weight transfer), we can track the time-dependent dynamics of spin, orbital, and structural order in LVO at various temperatures.

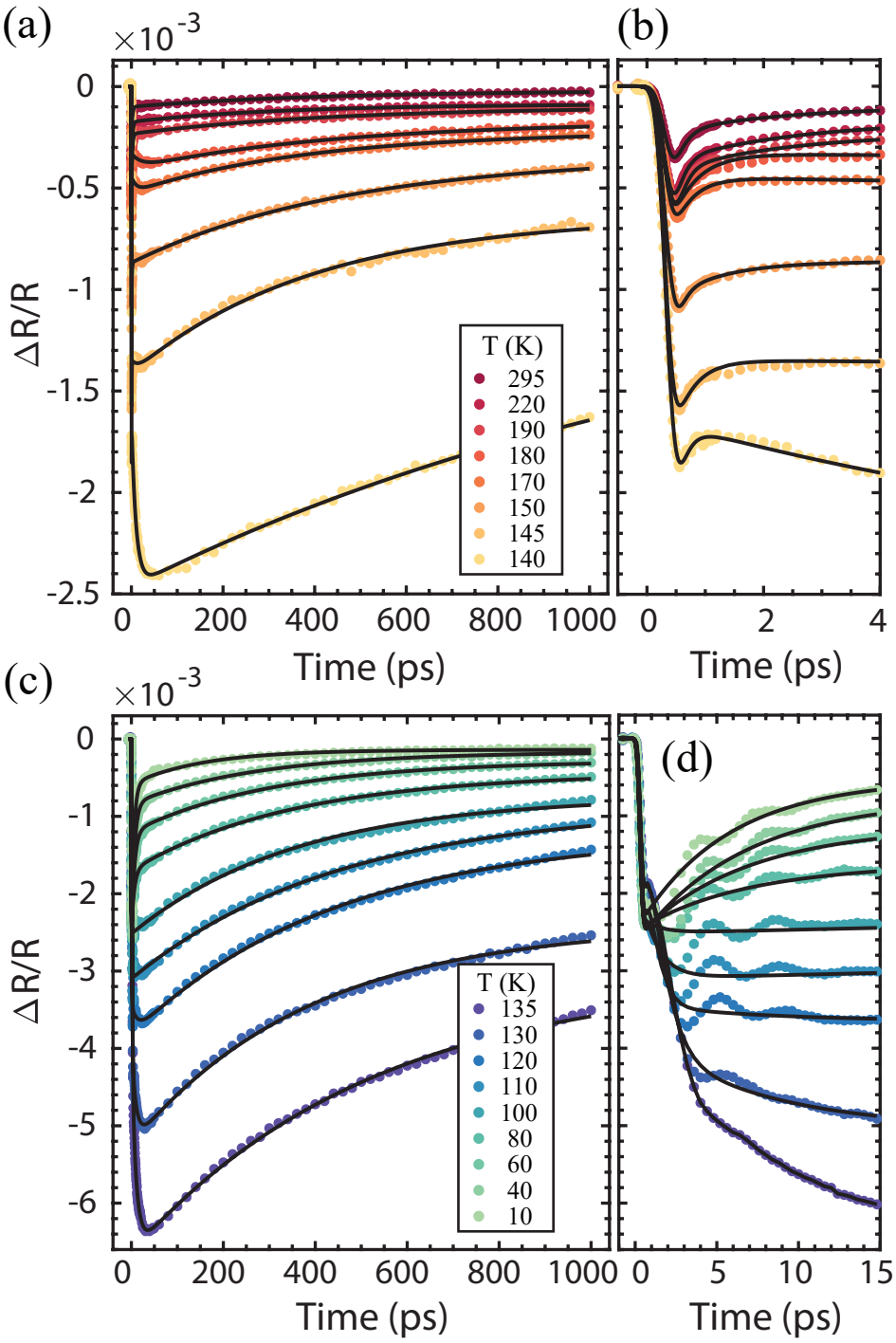

Figure 4.2: Photoinduced differential reflectivity traces in the high temperature phase ($T \geq 140$ K), for long (a) and short (b) pump-probe delays, and in the low temperature phase ($T \leq 135$ K) for long (c) and short (d) pump-probe delays. The black curves are exponential fits to the data, of the form given in Eq. 4.1.

4.4 Experimental Results

The time-dependent differential reflectivity signal $\Delta R/R$ in the high temperature phase (T $\geq$ 140 K) is shown in Fig. 4.2(a) and (b), for long and short pump-probe delays, respectively. The black lines are exponential fits to the data. Generally, the photoinduced change in $\Delta R/R$ is negative; there is a sharp increase in the signal amplitude occurring in $\sim$500 fs, followed by a slower multi-component recovery. As the temperature is lowered from 295 K we observe nearly an order of magnitude increase in the signal amplitude and a slowing of the recovery dynamics. Remarkably, upon crossing T_C = 140 K the trend is reversed. As shown in Fig. 4.2(c) and (d), the signal amplitude decreases and the dynamics quicken as the sample is cooled to 10 K. This indicates a fundamental change in the degrees of freedom our probe is sensitive to upon traversing T_C. Also of note is the emergence of an overdamped coherent mode with a period of $\sim$4 ps, seen in Fig. 4.2(d), which becomes less damped as the temperature is lowered. This is the result of an acoustic phonon launched by photoexcitation at the sample surface [58].

To better understand the changes occurring between the high and low temperature phase, $\Delta R/R$ in the vicinity of T_C is plotted in Fig. 4.3(a) for long time delays, and in Fig. 4.3(b) for short delays. The data in this region is highly reproducible and taken with particularly small temperature steps. The changes are dramatic; there is nearly an order of magnitude increase in the signal amplitude, occurring as the result of a secondary rise time emerging in the 10 – 40 ps range. The slowing of dynamics is clearly evident as well the recovery rate entirely flattening as the signal maxima at $T = 137.5$ K is approached, and the large offset at 1 ns indicating the presence of a long-lived carrier population. It is at this temperature that LVO enters the orbital and spin ordered phase, and the drastic changes in the signal reflect this. Further, this is the temperature at which formation of Hubbard excitons becomes energetically favorable after photoexcitation, due to the interaction with the AFM spin and anti-ferro orbital background in the ordered phase [38, 39]. Thus the photoinduced signal here begins, in part, to reflect exciton dynamics, evident

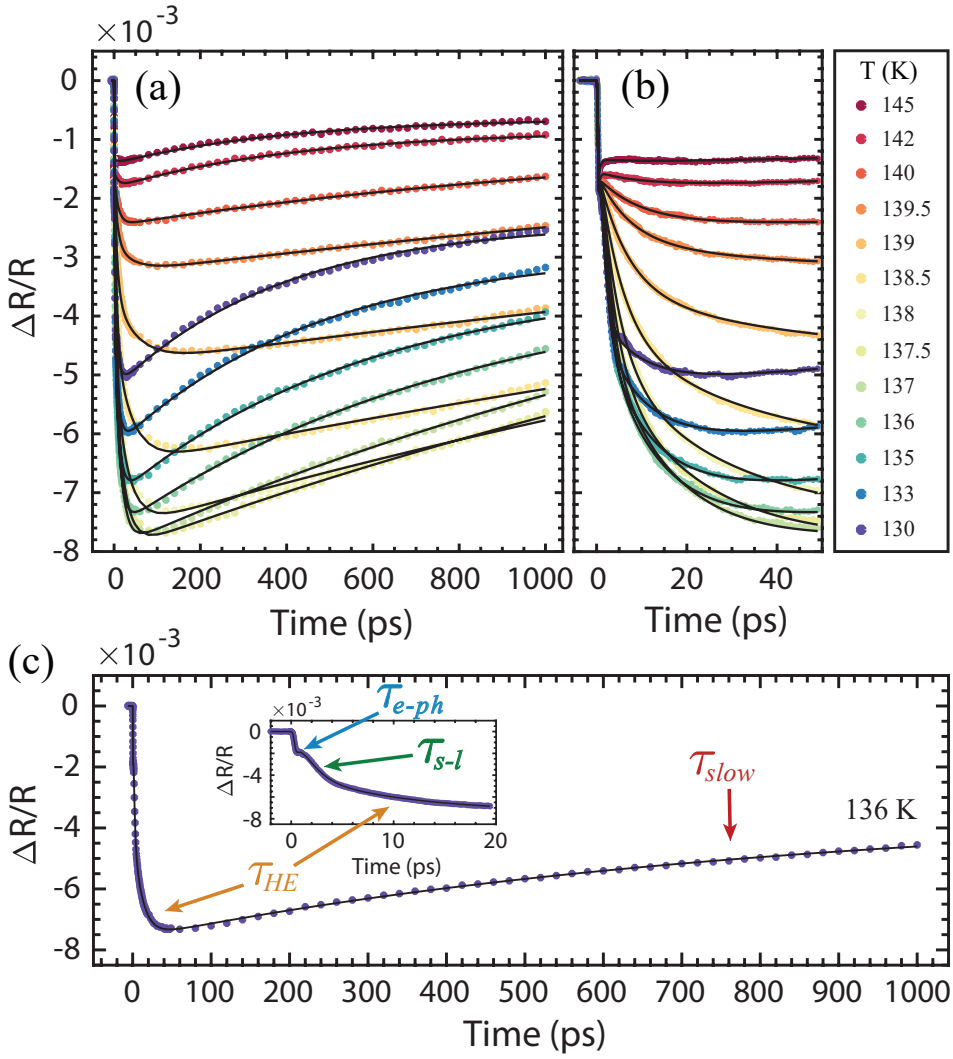

Figure 4.3: Photoinduced reflectivity traces near the critical temperature for long (a) and short (b) pump-probe delays with considerably smaller temperature steps in comparison to Fig. 4.2. Black curves are multi-exponential fits to the data. (c) Pump-probe scan at 136 K, showing the four separate components of the response, color-coded relative to Eq. 4.1.

in the emergence of a new rise time.

A quantitative analysis of the signal supports these claims and reveals further details of the response. The dynamics below T_C can be fit by a four-component exponential decay plus a constant offset of the form:

$$\Delta R/R(t) = A_{e-ph}e^{-t/\tau_{e-ph}} + A_{s-l}e^{-t/\tau_{s-l}} + A_{HE}e^{-t/\tau_{HE}} + A_{slow}e^{-t/\tau_{slow}} + C, \quad (4.1)$$

The fits using this equation are shown as the black lines in Fig. 4.2 and 4.3. An additional error function term (not included in Eq. 4.1) models the initial step-like rise in reflectivity. In the high temperature phase $T \geq 140\ K$, the 3^{rd} component labeled τ_{HE} vanishes, accurately fitting to only three exponentials. The full recovery process is largely dependent on the temperature, but in general there is a fast ($\tau_{e-ph} < 1$ ps) and slow recovery component ($\tau_{slow} \approx 100$'s ps), along with an intermediate ($\tau_{s-l} \leq 10$ ps) and an emergent component ($\tau_{HE} \approx 10-50$ ps), varying with temperature. These components are shown in Fig. 4.3(c) for a representative trace at 136 K.

As the measured time scales are well separated, we can attribute each time constant to a specific physical process. The initial delta-like increase in the magnitude of $\Delta R/R$, completed in less than 500 fs, can be attributed mainly to pump-induced photocarrier generation by intersite vanadium *d-d* transitions along the *c*-axis. This non-equilibrium distribution of carriers thermalizes via electron-electron (e-e) scattering within the initial rise time. At lower temperatures, in the ordered phase, this is accompanied by disruption of the orbital order, which similarly contributes to the sharp rise in $\Delta R/R$ [54, 59]. Following photoexcitation is an initial fast recovery, τ_{e-ph}, which occurs in $\sim$0.5 ps and is relatively temperature independent. This is attributed to electron-phonon (e-ph) relaxation, a process in which the hot photoexcited carriers thermalize with the lattice by coupling to optical and acoustic phonon modes. The timescale measured is consistent with results in other transition metal oxides, which measure e-ph relaxation on the order of < 1

ps [60, 61, 62]. The observed temperature independence of this time constant is consistent with expectations for electron-phonon thermalization.

A secondary rise time $\tau_{s-l} \leq 10$ ps occurs subsequent to electron-phonon relaxation. Near room temperature, this component has a characteristic timescale of $\sim$2 ps, which rises to $\sim$10 ps near 180 K, where its amplitude crosses zero from negative to positive. There is no divergence in the time constant upon approaching the spin and orbital ordering temperature, though the amplitude does sharply peak at T_C. Instead, τ_{s-l} monotonically decreases to $\sim$1 ps, and continues dropping to $\sim$0.4 ps at the lowest temperatures. We ascribe this process to spin-lattice thermalization. Thus at a delay of $\sim \tau_{s-l}$ the electron, lattice, and spin subsystems are at the same temperature, between $\sim 1-5$ K above the initial pre-photoexcitation temperature in the vicinity of T_C for the fluence we used. The observed timescales are consistent with measurements on other vanadates, such as YVO_3 and $GdVO_3$, where disruption of spin order occurs on the timescale of 2-4 ps [62, 63].

The third component of the signal τ_{HE} manifests as an additional rise on the order of 4 – 50 ps emerging near the critical temperature at $T = 140\ K$, shown in Fig. 4.4(a) as a function of temperature. We attribute this component to the transfer of spectral weight away from the Hubbard exciton peak in response to the photoinduced increased spin disorder and fluctuations (i.e. essentially a thermo-modulation signal from the small temperature increase). The value of τ_{HE} shows a sharp peak at T_C, while the amplitude peaks slightly below T_C. This component of the dynamics emerges only as G-OO and C-SO are established. Formation of the HE is governed by interaction of carriers with an antiferro-orbitally ordered and AFM spin ordered background. It follows that a timescale associated with the HE should emerge only below the ordering temperature, as observed. On this timescale, the increased temperature of the spin and orbital subsystem significantly increases quantum fluctuations, reducing the binding affinity of HEs. This causes a transfer of spectral weight away from the HE peak in the optical conductivity to higher energies, reducing the absorption at the probe energy and causing an additional decrease

in $\Delta R/R$. We note that while the spin subsystem has thermalized with the other high-temperature degrees of freedom on τ_{s-l} timescales, spin disorder continues to propagate on longer timescales. This has been observed in YVO_3 with time-resolved optical conductivity measurements, where spectral weight is transferred away from the HE peak on timescales between 50 – 400 ps as local photoinduced spin perturbations diffuse [38]. At low temperatures order is locked in and fluctuations are reduced, minimizing the spectral weight transfer away from the HE peak and thus minimizing time constant and amplitude of the τ_{HE} component.

The final component τ_{slow} is an exponential recovery on the order of $\sim$100 to $>$1000 ps, with the extracted time constant and amplitude as a function of temperature shown in Fig. 4.4(b). At both high and low temperatures the recovery time is relatively constant (approximately $\sim$400 ps). However, upon approaching T_C there is a sharp divergence in both the time constant and amplitude, rising by nearly an order of magnitude. We attribute this final component to the recovery of the excitonic resonance spectral weight as fluctuations subside and spin/orbital order is re-established. The return of spectral weight to the probed HE peak corresponds to an increase in absorption, visible in the increase of $\Delta R/R$ as it begins to recover to its equilibrium value. While a significant offset in $\Delta R/R$ remains at the longest times measured, indicating that heat does not fully diffuse out of the lattice until $t \gg 1$ ns, the photoexcited spin and orbital subsystems do return to equilibrium within $t \approx \tau_{slow}$. Above T_C, in the non-ordered phase, the amplitude of this component is nearly zero, only increasing to appreciable values as order and the HE develop, but photoinduced fluctuations must still recover and contribute to the recovery of $\Delta R/R$ at higher temperatures. The timescales we measure are highly consistent with optical pump-probe results on similar vanadates such as YVO_3 and $GdVO_3$, where the slow component assigned to spin relaxation is measured to be 300 – 3000 ps [40]. Our data is also consistent with the 400+ ps recovery of spin disorder in YVO_3 observed via spectral weight transfer between the HE and B peak [38]. While the recovery of orbital order has been recorded closer to 50 ps in YVO_3 and $GdVO_3$ [40], the close proximity of the spin and orbital ordering temperature in LVO and their

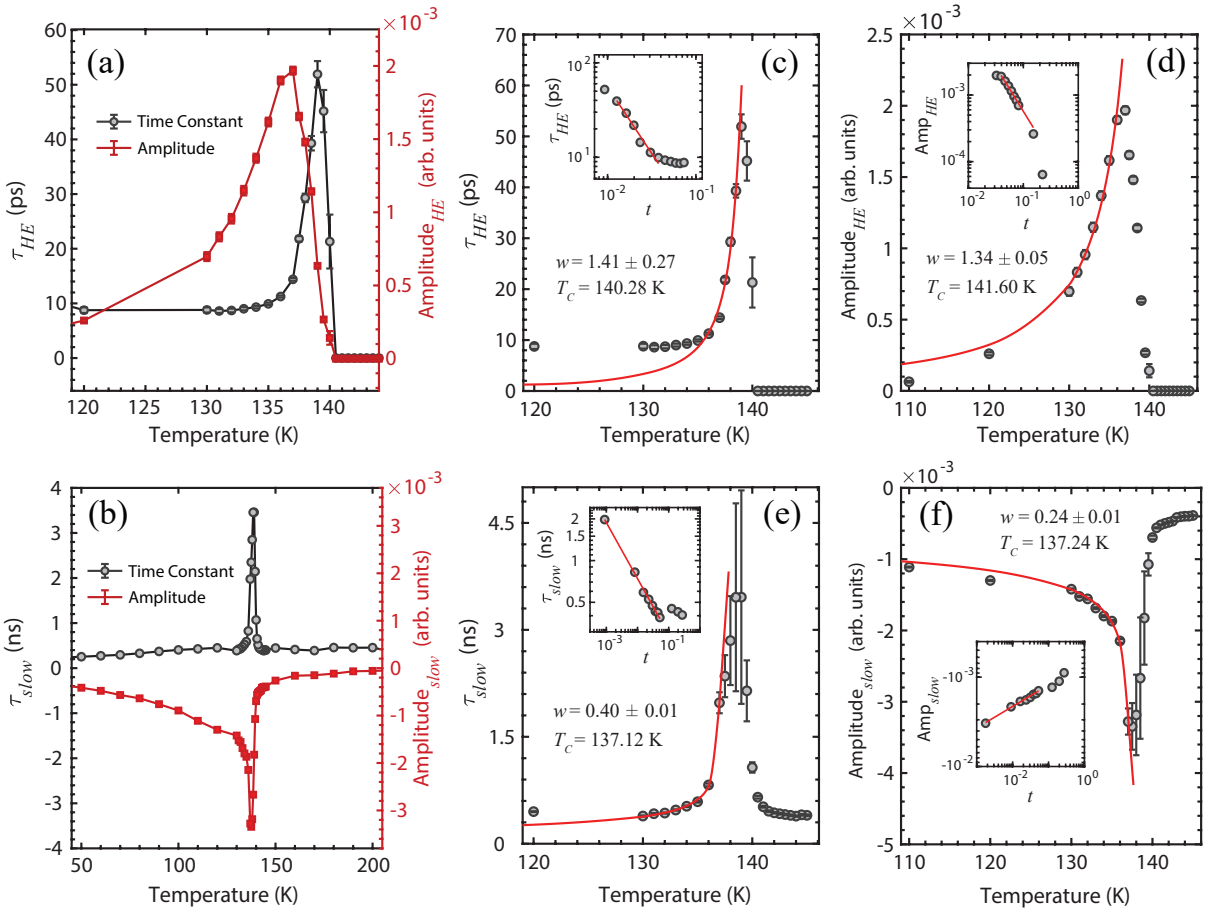

Figure 4.4: Time constants and amplitudes extracted from the exponential fits, for (a) the Hubbard exciton component τ_{HE} emerging at 140 K, and (b) the τ_{slow} component assigned to the recovery of spin and orbital order. The lines are guides to the eye. (c) and (d) depict the critical behavior and power-law fit (of the form given in Eq. 4.2, in red) for τ_{HE} and A_{HE}, respectively. The insets show the same data on a log-log scale with the reduced temperature. (e) and (f) present the power-law fits for the for τ_{slow} and A_{slow}, respectively.

highly coupled nature likely leads to additional frustration and longer orbital recovery times in our measurements. In summary, because the HE is highly dependent on the spin and orbital order in LVO and other vanadates, the recovery of order in these degrees of freedom re-establishes the excitonic resonance, transfers spectral weight back to the probed HE peak, and subsequently returns the $\Delta R/R$ signal to equilibrium.

4.5 Analysis and Discussion

Analyzing the diverging behavior of the τ_{HE} and τ_{slow} components in Figs. 4.4(a) and (b) near T_C yields additional insights. The dynamics are reminiscent of critical behavior seen at a second-order phase transition, where the order parameter and other thermodynamic quantities can be modeled by a power-law and critical exponent that obeys universal scaling laws. This takes the form

$$A = A_0 t^{-w}, \tag{4.2}$$

where w is the critical exponent and t is the reduced temperature $t = \frac{|T-T_C|}{T_C}$. The critical exponent is defined by a universality class based solely on the symmetry and dimensionality of the system, and therefore can be compared to theoretical predictions. Furthermore, dynamical scaling theory allows us to relate the critical exponents of static thermodynamic quantities to dynamic ones, such as a time constant extracted from time-resolved data [64, 65].

In the following analysis, we make an initial simplifying assumption that the phase transition observed at $T_C = 140$ K is primarily magnetic in nature. The magnetic correlation length ξ describes the characteristic length scale of magnetic correlations, and diverges at T_C as magnetic domains grow to macroscopic lengths with the form $\xi(T) \propto |t|^{-\nu}$, where ν is the correlation length critical exponent. This is related to the spin relaxation time by $\tau = \xi^z$, and leads to the expression $\tau(\mathrm{T}) \propto |t|^{-\nu z}$, where z is the generalized dynamic critical exponent [66, 67]. Both critical exponents depend solely on the universality class, i.e. the magnetic symmetry, of the system. The expression for the relaxation time above indicates a divergence of the relaxation time at T_C, a phenomenon known as critical slowing down. This is clearly visible in our data as τ_{HE} and τ_{slow} exhibit a quasi-divergence precisely at the transition. Finally, while dynamical scaling theory directly describes the behavior of a time constant near T_C, its amplitude is proportional to the population of carriers contributing to that time constant, resulting in a linear relationship between amplitude and time constant [68]. As such, a power-law analysis of both parameters is

appropriate.

To quantify the critical slowing down in LVO, we fit the time constant and amplitude of the τ_{HE} and τ_{slow} components to a power-law of the form given in Eq. 4.2. These fits are shown as the red curves in Figs. 4.4(c)-(f). The value of T_C is found by varying it within a small range to yield the best fit. The insets of these figures show the fit on a log-log scale as a function of the reduced temperature t, where linearity indicates a good fit. The results are excellent, considering that we expect a close fit only in a small temperature region near T_C where the theory is valid. Figs. 4.4(c) and (d) show the fits for τ_{HE} and A_{HE}, respectively. These yield critical exponents $w_{\tau-HE} = 1.41 \pm 0.27$ and $w_{A-HE} = 1.34 \pm 0.05$, and critical temperatures $T_{C-\tau-HE} = 140.28$ and $T_{C-A-HE} = 141.60$. This yields an average critical temperature of $T_{C-HE} = 140.94 \pm 0.93$ for the *HE* component. The same analysis can be applied to the *slow* component, and is shown in Figs. 4.4(e) and (f) for τ_{slow} and A_{slow}, respectively. These yield critical exponents $w_{\tau-slow} = 0.40 \pm 0.01$ and $w_{A-slow} = 0.24 \pm 0.01$, and critical temperatures $T_{C-\tau-slow} = 137.12$ and $T_{C-A-slow} = 137.24$. This yields an average critical temperature of $T_{C-slow} = 137.18 \pm 0.08$ for the *slow* component.

Next, we compare the critical exponent w extracted from our fits to those predicted by theory. As detailed above, the measured time constants are related to the dynamic and correlation length critical exponents by $\tau(\mathrm{T}) \propto |t|^{-\nu z}$, such that $w = \nu z$. Due to the anisotropic *C*-type AFM spin order LVO should be described by the 3D Ising model, which predicts $\nu = 0.63$ [69] and $z = 2$ [66] with $w = z\nu = 1.26$. The critical exponents of the τ_{HE} and A_{HE} component in Figs. 4.4(c) and (d) are close but moderately higher than this, while those measured from the τ_{slow}components in Figs. 4.4(e) and (f) are substantially lower. Other models are less suited to describe the magnetic symmetry of LVO and come no closer to the measured critical exponents: the 3D AFM Heisenberg model predicts $\nu = 0.71$ [70] and $z = 1.5$ [66] ($z\nu = 1.07$), the 2D Ising model predicts $\nu = 1$ [71] and $z = 1.75$ [72] ($z\nu = 1.75$), and the 2D Heisenberg AFM model is only valid in the limit $\mathrm{T} \to 0$ [73]. It appears that the critical behavior of the τ_{HE} component

near T_C nearly matches that of the 3D Ising universality class, but the τ_{slow} component does not belong to any predicted universality class for magnetic order. These results are consistent with our assignments of τ_{HE} and τ_{slow}. τ_{HE} represents the diffusion of spin disorder, a phenomenon described by a magnetic order parameter that obeys universal scaling laws. On the other hand, the departure of τ_{slow} from universal scaling behavior implies that this timescale reflects more than just the spin degree of freedom. It is a measure of the recovery of both spin *and* orbital order, and therefore need not belong to a particular universality class. However, the power-law dependence of τ_{slow} does suggest that orbital recovery dynamics may be modeled by an order parameter that obeys non-standard or unknown scaling laws. Further time-resolved measurements on materials with a well-separated spin and orbital ordering temperature, such as YVO_3, should be performed to confirm this interpretation.

In the above analysis we have assumed a phase transition that is second-order in nature, but it is instructive to consider this more closely. According to heat capacity, magnetization, and neutron diffraction measurements on LVO single crystals [74, 75], the phase transition at 140 K appears to be first-order. Yet the observed diverging power law behavior and critical slowing down near T_C suggest a second-order phase transition. However, although the phenomenon of critical slowing down is usually ascribed to a second order phase transition, it is known [66] (and we will explicitly show in the following) that many of the features of slowing down are also found in a dynamical simulation of a generic first order phase transition with free energy:

$$f(T) = f_0(T) + \alpha_0(T - T_c)m^2 + \frac{1}{2}\beta m^4 + \frac{1}{3}\gamma m^6 \qquad \alpha_0 > 0, \quad \beta < 0, \quad \gamma > 0, \quad (4.3)$$

where m is the order parameter and $f_0(T)$ describes the temperature dependence of the high temperature phase near the phase transition. We treat the parameters of this theory as fit parameters, and check that the obtained values are consistent with previously reported results for the behavior of the specific heat (described by the same theory of a first order phase transition). As shown

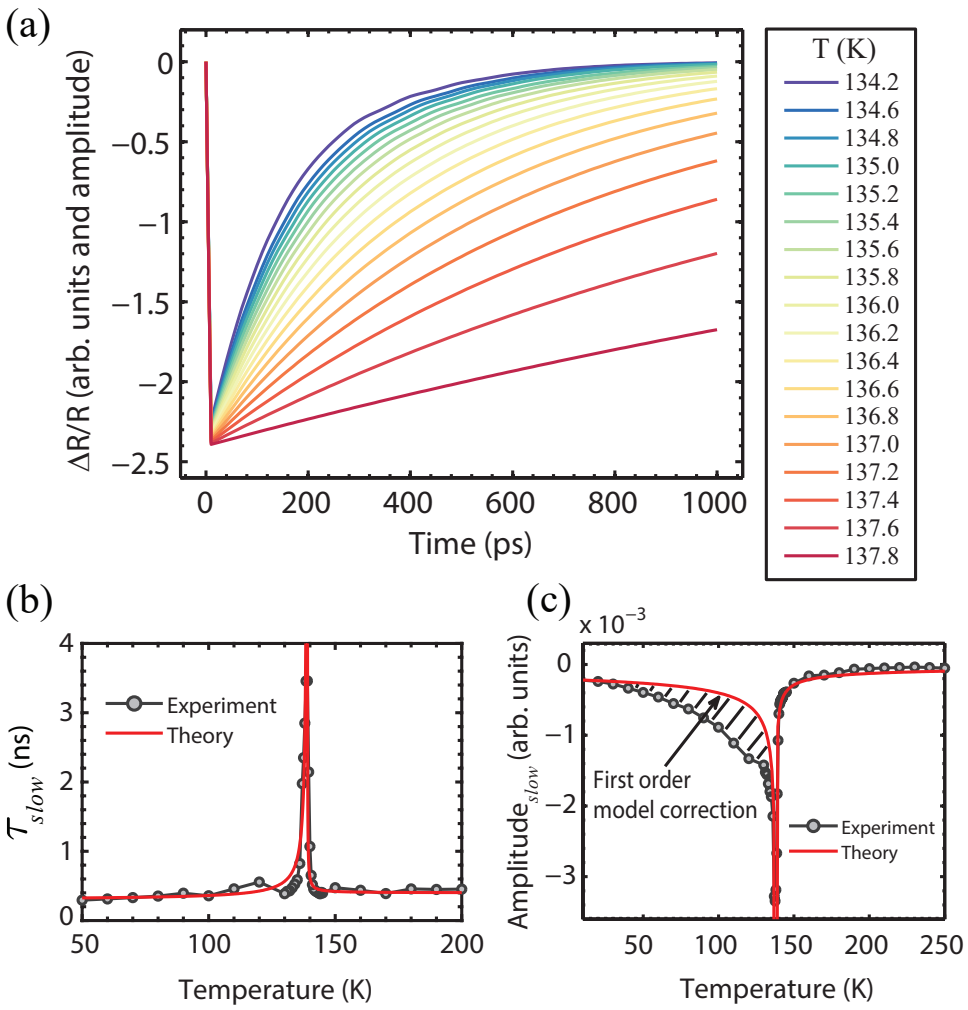

Figure 4.5: (a) Time-dependent Ginzberg-Landau simulations for a generic first order phase transition, as a function of temperature near T_C. The results qualitatively match the experimental data, with a similar slowing down of dynamics approaching T_C. The simulated fit parameters, (b) τ_{slow} and (c) A_{slow}, are plotted in red alongside the experimental values. The modelled amplitude deviates below T_C, and expanding the order parameter to higher orders provides a slight correction. Modelling the system parameters specifically LVO will provide further correction.

in Fig. 4.5(a), we find that the simulation yields dynamics which are remarkably similar to the experimental pump-probe results: a prominent slowing down and flattening in the recovery rate as T_C is approached. Fig. 4.5(b) and (c) show the simulation-derived time constant and amplitude, respectively, plotted versus temperature along with the experimental data. The modeled results show a similar divergence in τ_{slow} at T_C. The deviation in the amplitude below T_C indicates a correction that we believe can be obtained by using a model for the free energy specific to LVO, rather than a generic first-order phase transition. Indeed, we have checked that adding higher order terms to the free energy can be used to improve the agreement. As we do not have enough information about the true free energy of the system at this point and we cannot rule out that the physics might actually be more involved (e.g. coupling to other ordering tendencies). As such, we leave a study of a microscopically motivated model for the future. However, as pointed out above even this generic theory succeeds in capturing the key experimental findings of the slowing down of the relaxation dynamics.

The above model indicates that the transition may not be of second order but instead weakly first-order, with pseudo-critical dynamics that are described by a non-conserved order parameter and non-universal scaling [76]. This is associated with a first-order phase transition involving metastable ordered states and long-lived dynamics. This may be applicable to the slow recovery of spin and orbital order in τ_{slow} observed near the transition. Recent work on charge and magnetically ordered perovskite $La_{1/3}Sr_{2/3}FeO_3$ films have shown similar pseudo-critical behavior [77].

Finally, we wish to understand the origin of the observed critical slowing down near T_C. The Landau free energy is a good starting point. Generally, as a phase transition is approached the free energy landscape widens and bifurcates from a single potential minimum to two below T_C, separated by some non-zero value of the order parameter. In doing so, any perturbation of the order parameter will take longer to reach equilibrium in this shallower potential at T_C, thus slowing down the dynamics. While this is common to any second order and perhaps to a weakly

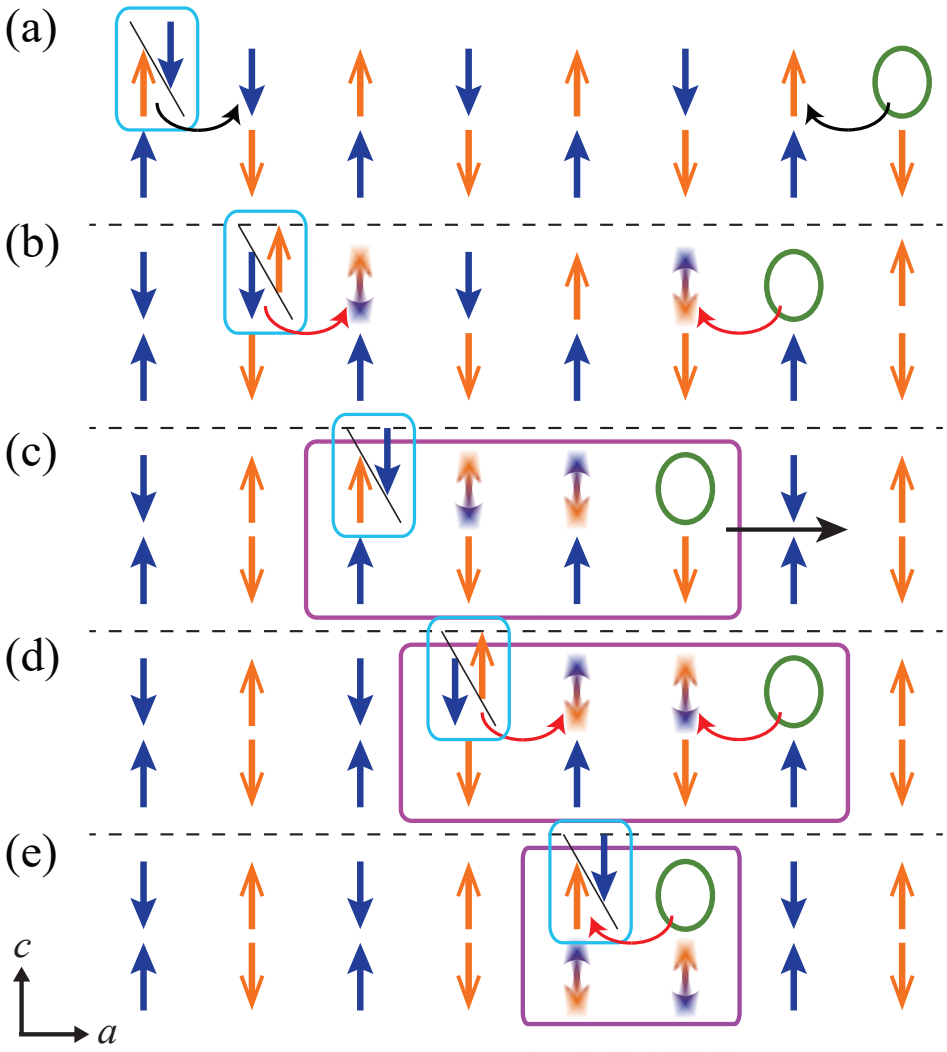

Figure 4.6: Exciton (purple square) dynamics near T_C on an AFM spin and antiferro-orbitally ordered background. Each arrow represents the spin at a separate lattice site. Blue (orange) arrows represent a filled d_{yz} (d_{zx}) orbital, the green "O" a hole, and the light blue square a "double occupancy" (DO). Blue and orange double arrows represent fluctuating spin and orbital order. (a) Hole and DO are well separated some time after photoexcitation. Each hopping process creates both spin and orbital disorder. (b) Hopping to a site with fluctuating order is slower (red arrow) due to lower orbital overlap. (c) Exciton formation. Motion of the bound exciton leaves zero net spin/orbital disorder. (d)-(e) Recombination requires additional hopping processes, slowed by fluctuations.

first-order phase transition, it ignores microscopic details.

A less phenomenological explanation involves spin and orbital fluctuations and their relation to exciton dynamics. Fluctuations in any system's order parameters occur in the vicinity of phase transitions. LVO in particular is known to have strong orbital fluctuations which exist up to room temperature and are suppressed only in the low temperature ordered phase [34, 50]. Though fluctuations may in fact be less significant than previously assumed [39], any system approaching criticality at a phase transition will experience fluctuations. It is these fluctuations that alter the energy landscape and slow the dynamics. The measured recovery times τ_{HE} and τ_{slow} are, as described above, associated with photoinduced spectral weight transfer away from and back to the HE peak. As such, the measured dynamics are related to the dynamics of Hubbard exciton formation in the presence of a fluctuating many-body environment.

Fig. 4.6 depicts the exciton formation process, starting from a point after photoexcitation where the hole and "double occupancy" (DO) have diffused and are well separated. As previously described, motion of a single hole or DO on the ordered background in any direction leaves a trail of misaligned spins and orbitals, frustrating the system and reducing the effective hopping [Fig. 4.6(a)-(b)]. These quasiparticles will therefore seek to move together as a bound pair that leaves zero net disorder. Near T_C and on τ_{HE} timescales, spin and orbital fluctuations are large, lowering the average orbital overlap between adjacent sites is reduced and reducing the effective electron hopping. Combined, this leads to a drastic slowing of the motion of unbound quasiparticles at T_C and greatly suppresses the exciton formation process [Fig. 4.6(b)-(c)]. This reduces the spectral weight at the probed HE peak both at temperatures near T_C where spin/orbital fluctuations are inherently large, and at timescales on the order of τ_{HE} after photoexcitation when fluctuations are large due to pump-induced spin/orbital disorder and heating. Fluctuations must subside before the excitonic formation probability improves and spectral weight is transferred back to the HE peak, which occurs on τ_{slow} timescales after photoexcitation. In addition, spatial segregation of charge carriers due to increasing correlation length and growth/fluctuation of ordered domains

may contribute to the divergence in timescales observed at T_C. This has been shown in the manganite $Ti_2Mn_2O_7$, where spin disorder and spatial inhomogeneity near a phase transition slow the carrier/hole recombination process [78]. As the sample is further cooled below T_C, fluctuations in the spin and orbital degrees of freedom are frozen as strong order is established, exciton formation is no longer suppressed, and the optical conductivity at the HE peak greatly increases.

While we do not measure exciton recombination directly, the following scenario details the process in order to provide a complete description of HE dynamics. As the Hubbard exciton is not a truly bound state, the constituent hole and DO still somewhat spatially separated, the recombination process suffers from the same effects as those influencing HE formation. The hopping processes required to recombine are slowed due to the fluctuating background order near T_C [Fig. 4.6(d)-(e)]. Again, exciton recombination requires orbital overlap between adjacent sites, which is reduced on a fluctuating background and slows recombination. It is clear that both HE formation and recombination are intimately tied to the spin and orbital order and their fluctuations. Changes in exciton dynamics directly contribute to changes in spectral weight at the probe energy, and thus are reflected in the timescales we measure.

4.6 Conclusion

In summary, we have measured the time-resolved photoexcited dynamics of $LaVO_3/SrTiO_3$ thin films using ultrafast pump probe spectroscopy. The 1.6 eV pump and probe wavelength corresponds to an excitonic resonance above the Mott-Hubbard gap. As the Hubbard exciton is highly dependent on the spin and orbital order of the system, measurements at this photon energy serve as a sensitive probe of order parameter dynamics. The dynamics after photoexcitation proceed as follows: (1) direct photoexcited carrier generation, followed by electron-electron thermalization within 500 fs; (2) thermalization of hot electrons with the lattice through electron-

phonon coupling, occurring in ∼0.5 ps; (3) perturbation of the spin order and out-of-equilibrium thermalization of the spin, lattice and electron subsystems through spin-lattice coupling, occurring on the order of 2 – 10 ps; (4) transfer of spectral weight away from the HE peak in the optical conductivity as spin disorder diffuses and the excitonic resonance decreases in ∼4 – 50 ps; (5) and recovery of the HE spectral weight as spin and orbital order recover and photoinduced fluctuations subside within ∼300 – 3500 ps. The dynamic HE spectral weight transfer reveals anomalous slowing down of the exciton, spin, and orbital dynamics at the structural, spin, and orbital ordering temperature $T_C \cong 140$ K. All display pseudo-critical behavior and critical slowing down, reminiscent of a second-order phase transition, despite the (weakly) first-order nature of the transition.

This work provides a path for further investigating Mott-Hubbard exciton dynamics in transition metal compounds with highly correlated spin and orbital order. The observation of non-universal critical behavior in the coupled spin and orbital order recovery component suggests that orbital dynamics could potentially be described by a universal critical exponent. The specific relation of the individual spin and orbital degrees of freedom to the exciton binding energy also merits further study. High sensitivity, low fluence measurements on related Mott-Hubbard insulators with well separated phase transition temperatures, such as YVO_3 and $YTiO_3$, should be performed to check for similar critical behavior. Studying Hubbard exciton physics in these highly correlated systems will allow us to better understand the complex materials where multiple intertwined degrees of freedom interact to produce pairing mechanisms and interesting emergent behavior.

4.7 Acknowledgements

This chapter is, in full, a submission to Physical Review B in 2020. The dissertation author was the primary investigator and author of this paper. Dylan Lovinger, Matthew Brahlek,

Peter Kissin, Dante Kennes, Andrew Millis, Roman Engel-Herbert, Richard Averitt 2020.

Chapter 5

Magneto-Elastic Coupling to Acoustic Phonon Modes in Ferrimagnetic Insulator $GdTiO_3$

5.1 Abstract

In this section we present results on single crystal $GdTiO_3$, a promising candidate material for Floquet engineering and magnetic control, using ultrafast optical pump-probe reflectivity and magneto-optical Kerr spectroscopy. $GdTiO_3$ is a Mott-Hubbard insulator with a ferrimagnetic and orbitally ordered ground state (T_C = 32 K). We observe multiple signatures of the magnetic phase transition in the photoinduced reflectivity signal, in response to above band-gap 660 nm excitation. Magnetic dynamics measured via Kerr spectroscopy reveal optical perturbation of the ferrimagnetic order on spin-lattice coupling timescales, highlighting the competition between the Gd^{3+} and Ti^{3+} magnetic sub-lattices. Furthermore, a strong coherent oscillation is present in the reflection and Kerr dynamics, attributable to an acoustic strain wave launched by the pump pulse. The amplitude of this acoustic mode is highly dependent on the magnetic order of the

system, growing sharply in magnitude at T_C, indicative of strong magneto-elastic coupling. The driving mechanism, involving strain-induced modification of the magnetic exchange interaction, implies an indirect method of coupling light to the magnetic degrees of freedom and emphasizes the potential of $GdTiO_3$ as a tunable quantum material.

5.2 Introduction

The rare-earth titanates (unit formula $RTiO_3$, where R is a rare-earth ion) are a class of complex materials with strongly correlated spin, orbital, and lattice degrees of freedom. They are $3d^1$ compounds with a single d-orbital electron occupying the Ti^{3+} t_{2g} orbital, whose degeneracy is broken by strong crystal field splitting [79]. This presents an opportunity to study a strongly correlated system in relative simplicity, which nonetheless exhibits rich physics and interesting properties. The perovskite titanates, for example, are Mott-Hubbard (MH) insulators with interconnected orbital and spin order [80, 81, 82, 83, 84]. Of particular interest is the complex magnetic phase diagram for this class of materials, with a magnetic ground state that varies from ferrimagnetic to antiferromagnetic as a function of the rare-earth ion size and subsequent change in Ti-O-Ti bond angle [79, 9]. Various theories have attempted to explain the magnetic order in titanates [83, 85, 86, 87], all of which highlight the need to consider the roles of structure and electronic correlation to understand the complexity embodied in the magnetic phase diagram.

Common to all descriptions of magnetism in the perovskite titanates is the defining role of the lattice and its distortion. It has been argued, for example, that the degree of $GdFeO_3$ distortion and changes to the Ti-O-Ti bond angle directly modify the exchange interaction which, in turn, determines the magnetic order [9, 88]. More recent results emphasize the importance of orbital order in determining the magnetic order. In particular, the direct coupling between the orbital order and lattice, rather than the orthorhombic distortion contributes most strongly to the ground state [89, 90, 91]. Whether it is particular structural distortions or more generalized Jahn-Teller

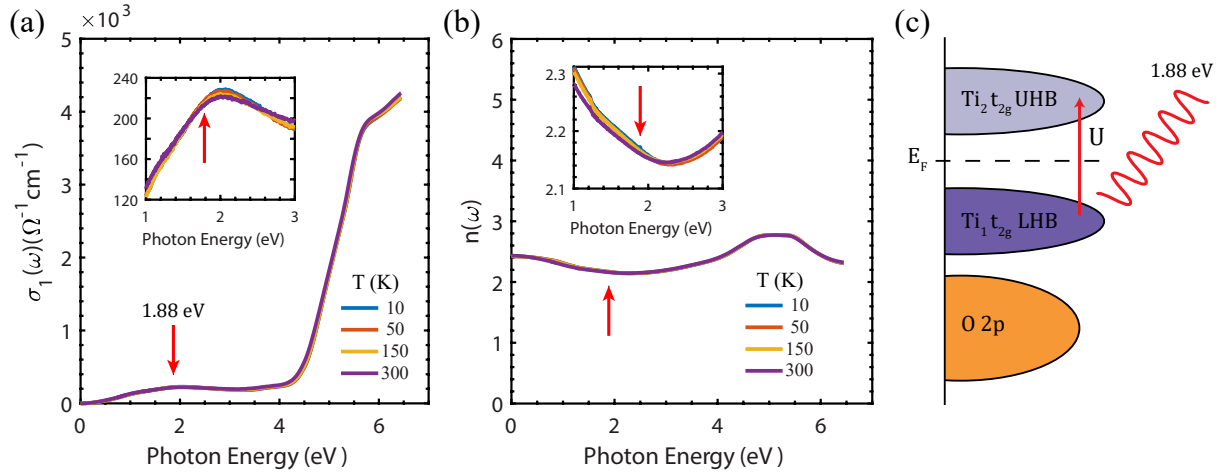

Figure 5.1: (a) Optical conductivity and (b) index of refraction of GTO/LSAT thin film as a function of photon energy and temperature. Red arrows indicate the 1.88 eV pump/probe energy. The weak feature in σ_1 at 2 eV corresponds to the MH gap, while the steep feature near 5 eV arises from O_{2p} to Ti_{3d} and Gd_{4f} charge transfer transitions. (c) Depiction of 1.88 eV laser excitation, corresponding to intersite Ti *3d-3d* transition across the MH gap.

distortions, and regardless of the role of orbital ordering, it is clear that magnetic order in titanates is highly dependent on the lattice.

In this work we study $GdTiO_3$ (GTO), a titanate with an orthorhombic perovskite-type unit cell and relatively large $GdFeO_3$-type distortion. GTO lies just within the ferromagnetic (FM) region of the phase diagram. The proximity to the FM-AFM transition makes GTO particularly sensitive to the effect of structural changes on the magnetism [89]. Below the critical temperature T_C = 32 K it is ferrimagnetically (fM) ordered, with the Ti^{3+} spins aligned ferromagnetically along the *c*-axis, coupled antiferromagnetically to the Gd sublattice [81, 85, 89]. The magnetism saturates at 6 μ_B (7 μ_B Gd – 1 μ_B Ti) in a relatively small field of ∼0.1 T, with no discernable hysteresis [92]. The magnetocrystalline anisotropy is small, with the *a*-axis as the hard magnetization axis and the *b*-*c* plane nearly isotropic. The fM order is accompanied and mediated by (*yz, zx, yz, zx*)-type orbital order, a result of inter-atomic hybridization between the t_{2g} and e_g orbitals [79].

The present work on GTO is motivated not only by the relative simplicity of the system

and rich interconnected order, but also the potential for Floquet engineering and ultrafast control of magnetism. Liu *et al.* explored the Mott insulating titanates as a candidate for tuning the spin-orbital Floquet Hamiltonian and subsequent modification of the spin exchange interaction using light [93]. Meanwhile, Khalsa *et al.* suggest direct excitation of a GTO mid-IR active phonon mode to transiently modify the exchange interaction and switch the ground state from FM to AFM on ultrafast timescales [94].

While the conditions of our experiment lie outside the regimes discussed above, we do observe strong coupling between light, the lattice, and the sample magnetism. Time-resolved pump-probe and magneto-optical Kerr effect (MOKE) measurements tuned to $\sim$1.88 eV, just above the bandgap, allow us to measure the evolution of photoexcited states on femtosecond – picosecond timescales. We observe multiple signatures of the magnetic phase transition in the photoinduced reflectivity signal, as well as optical perturbation of the fM order on spin-lattice coupling timescales in the MOKE signal. In addition, an acoustic phonon mode is present in both signals, whose amplitude is highly coupled to the magnetic order. This implies strong magneto-elastic coupling through transient, strain-induced modification of the exchange interaction, connecting the lattice and magnetic degrees of freedom and indicating that the exchange interaction is tunable on ultrafast timescales.

5.3 Methods

Single crystal and thin film samples of $GdTiO_3$ were investigated. The photoinduced reflectivity signal in both is extremely similar and the following work, except for the measurement of the optical constants, was performed on a single crystal sample. For comparison, the thin film time-resolved reflectivity data is presented in SM I. $GdTiO_3$ thin films ($\sim$20 nm) were grown on a (001)$(La_{0.3}Sr_{0.7})(Al_{0.65}Ta_{0.35})O_3$ (LSAT) substrate by hybrid molecular beam epitaxy [95]. $GdTiO_3$ bulk single crystals were grown by high pressure laser floating zone method [96]. A

small fraction of the crystal rod was cut and polished to optical quality, with *bc*-axis in plane and *a*-axis out of plane. Powder X-ray diffraction measurements indicate extremely high quality crystals with no notable impurity peaks and lattice parameters at 5.393, 5.691, 7.664 Å for *a*,*b*, *c*-axis [96], well matched to literature values [89]. Magnetization measurements indicate no visible hysteresis and a saturation moment of 6 μ_B/FU.

To determine the optical conductivity and index of refraction, frequency-dependent reflectivity spectra $R(\omega)$ in the photon energy region between 3 meV and 85 meV were measured by using a Bruker VERTEX 70v Fourier transform spectrometer. The $GdTiO_3$ thin film was mounted in a continuous liquid helium flow cryostat. We used two spectroscopic ellipsometers (IR-VASE Mark II and M-2000, J. A. Woollam Co.) for obtaining the complex dielectric constants $\varepsilon(\omega) = \varepsilon_1(\omega) + i\varepsilon_2(\omega)$ in the energy range from 60 meV to 0.75 eV and 0.75 eV to 6.4 eV, respectively. The optical conductivity of the $GdTiO_3$ film was obtained by two-layer model fit employing Drude-Lorentz oscillators for optical response of each layer [97].

Ultrafast optical pump-probe reflectivity measurements ($\Delta R/R$) are performed using a 1040 nm 200 kHz Spectra-Physics Spirit Yb-based hybrid-fiber laser coupled to a non-colinear optical parametric amplifier. The amplifier produces $\sim$20 fs pulses centered at 660 nm (1.88 eV), which are split, cross-polarized (pump *s*-polarized, probe *p*), and used as degenerate pump and probe beams. The pump is aligned along the *b*-axis of the GTO crystal. This excitation corresponds to an intersite Ti *3d* – *3d* transition across the Mott-Hubbard gap, shown in Fig. 5.1(c). A moderate pump fluence of $\sim$100 μJ/cm^2 is used to minimize sample heating ($\sim$4 K at 10 K), ensuring we are in the linear excitation regime.

Time-resolved magneto-optical Kerr spectroscopy is used to probe the magnetization dynamics. The same optical system described above is used here, including laser energy, fluence, and optical cryostat (Quantum Design OptiCool). The photoinduced Kerr rotation ($\Delta\theta_K$) is measured using balanced photodiodes in the polar Kerr geometry at near-normal incidence, in a continuously variable external magnetic field (0 – 7 T), with the pump polarized along

the b-axis and Kerr probe polarized along the c-axis of the crystal. The magnetic field is applied normal to the sample surface, along the a-axis of the crystal, resulting in a Kerr signal proportional to the z-component of the photoinduced change in magnetization ΔM_z. In order to eliminate non-magnetic contributions to the signal and ensure we are measuring genuine spin dynamics, we take the difference of the Kerr signal at various positive and negative applied fields: $\Delta\theta_K = \Delta\theta(+M) - \Delta\theta(-M)$ (see SM IV for details).

5.4 Experimental Results

The temperature-dependent optical conductivity signal is shown in Fig. 5.1(a) for photon energies ranging from 0 to 6.5 eV, and for temperatures from 10 K to 300 K. A weak feature is present, centered at 2 eV, corresponding to the Mott-Hubbard gap. Apart from weak thermal broadening with increasing temperature, the peak at 2 eV is nearly temperature independent. While early studies of GTO measured a MH gap of 0.2 – 0.7 eV [98], more recent photoluminescence and DFT/DFT+U results place the gap closer to 1.8 – 2 eV [99]. The small peak in the optical conductivity spectrum at 2 eV measured here supports these recent findings. At much higher energies we observe a significant increase in the optical conductivity. The features near 5 eV correspond to O_{2p} to Ti_{3d} and Gd_{4f} transitions. Fig. 5.1(b) shows the index of refraction in the same energy range, which remains relatively constant as a function of temperature.

The time-dependent photoinduced change in reflectivity $\Delta R/R$ is shown in Fig. 5.2(a), for all measured temperatures between 10 – 295 K (legend on Fig. 5.2(b)). The black lines represent exponential fits to the data as described below. The photoinduced change in $\Delta R/R$ is positive; following laser excitation a non-equilibrium electron population is established in $\sim$500 fs, which then exchanges energy and equilibrates with the spin and lattice subsystems through various pathways, each with a characteristic timescale. This is visible as the slower, multi-component exponential relaxation. As the temperature is decreased from 295 K the signal

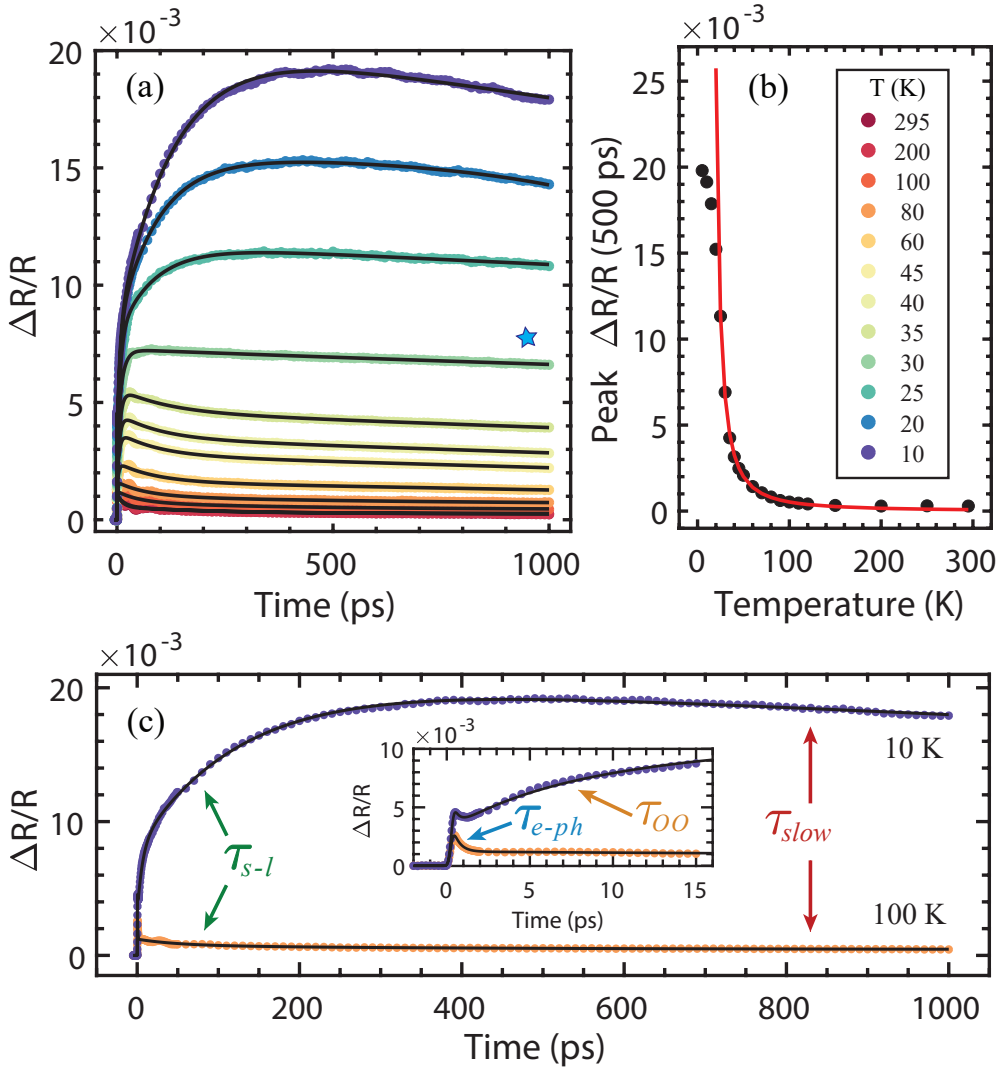

Figure 5.2: (a) Photoinduced differential reflectivity signal $\Delta R/R$ at all measured temperatures, from 10 K to 295 K. The black curves are exponential fits to the data, of the form given in Eq. 5.2. The blue star indicates the data curve taken at T_C. (b) $\Delta R/R$ values at 500 ps, an approximation of the peak signal at all temperatures. The red line is a power law fit, commonly seen in systems undergoing a second-order magnetic phase transition. (c) Representative pump-probe scans at 10 K and 100 K, indicating the various timescales involved in the recovery process (see Eq. 5.2).

amplitude increases, recovery dynamics slow, and two additional features emerge. The first is a delayed rise time, corresponding to a further departure from equilibrium in the first ∼15 ps, emerging below T = 100 K. Second, there is a crossover point visible at delay times of ∼200 ps where recovery dynamics flatten and reverse direction to become an additional rise time. This occurs precisely as the ferrimagnetic ordering temperature T_C = 32 K is crossed (marked by a blue star), indicating that magnetization dynamics manifest in the differential reflectivity signal.

To further investigate the temperature dependence of the reflectivity signal, we plot the peak signal amplitude (at 500 ps) in Fig 5.2(b). The behavior here is distinctive, not uncommon in materials undergoing a second-order magnetic phase transition. The red curve represents a power-law fit to the data, of the form

$$A = A_0 t^{-w}, \tag{5.1}$$

where w is the critical exponent and t is the reduced temperature $t = \frac{|T-T_C|}{T_C}$. Our fit produces a critical exponent $w = 1.28 \pm 0.02$. This very nearly matches the critical behavior predicted by dynamical scaling theory for the 3d Ising model, which yields $w \approx 1.32$ [66, 100, 69] (further detailed in SM II). The close match between experiment and theory, whose predictions depend upon the magnetic symmetry and universality class of the magnetic transition, indicates a strong magnetic contribution in the $\Delta R/R$ signal. Additionally, the qualitative form of the peak amplitude vs temperature follows that of the temperature dependent magnetic susceptibility in bulk GTO [92], and the magnetization M in films [101]. While by no means conclusive, the mean-field behavior and agreement with thermal magnetization does strongly suggest that the $\Delta R/R$ signal measured, particularly at longer times (500+ ps), is sensitive to spin dynamics.

To substantiate these claims, we quantitatively analyze the full time-dependent response. Below 100 K, the dynamics can be fit by a sum of four exponentials with a constant offset, of the

form:

$$\Delta R/R(t) = A_{e-ph}e^{-t/\tau_{e-ph}} + A_{OO}e^{-t/\tau_{OO}} + A_{s-l}e^{-t/\tau_{s-l}} + A_{slow}e^{-t/\tau_{slow}} + C, \quad (5.2)$$

shown as black lines in Fig. 5.2(a). Not listed is an additional error function term, which describes the initial step-like rise dynamics at $t = 0$. A visual representation of the various timescales is shown in Fig. 5.2(c) for two temperatures. After excitation the dynamics follow a general trend; there is a very fast initial recovery, τ_{e-ph} on the order of ~500 fs, followed by an intermediate term τ_{OO} on the order of 2 – 8 ps, both of which are clearly visible in the inset of Fig. 5.2(c). Note that τ_{OO} is an additional rise time which vanishes at higher temperatures, the full dynamics fitting to only 3 exponentials (i.e. above T_C). This is followed by a slower term τ_{s-l} on the order of 100's of picoseconds, and a final much slower recovery τ_{slow}. A careful inspection of the reflectivity data also indicates the presence of small oscillations about the black fitted curves, which we discuss below.

These measured timescales are well separated and can be attributed to distinct physical processes. The initial pump pulse excites an intersite Ti *3d-3d* transition. This directly creates a population of hot carriers which thermalize via electron-electron (e-e) scattering, then subsequently exchange energy with the lattice, orbital, and spin degrees of freedom. We focus on the spin-lattice coupling process here, with a full discussion of the remaining processes and time constants in SM III.

The most relevant component of the $\Delta R/R$ signal is the third fitted exponential, τ_{s-l}, attributed to spin-lattice coupling and shown in Fig. 5.3(a). This term has a characteristic timescale of 10 – 140 ps, excluding the region at the magnetic phase transition temperature T_C = 32 K where the lifetime grows too long to accurately measure. This critical region is visible as a flattening of the ΔR/R recovery at 30 K, indicated by the blue star in Fig. 5.2(a). Before the onset of this third recovery term τ_{s-l}, the ΔR/R signal reveals dynamics indicative of electron-

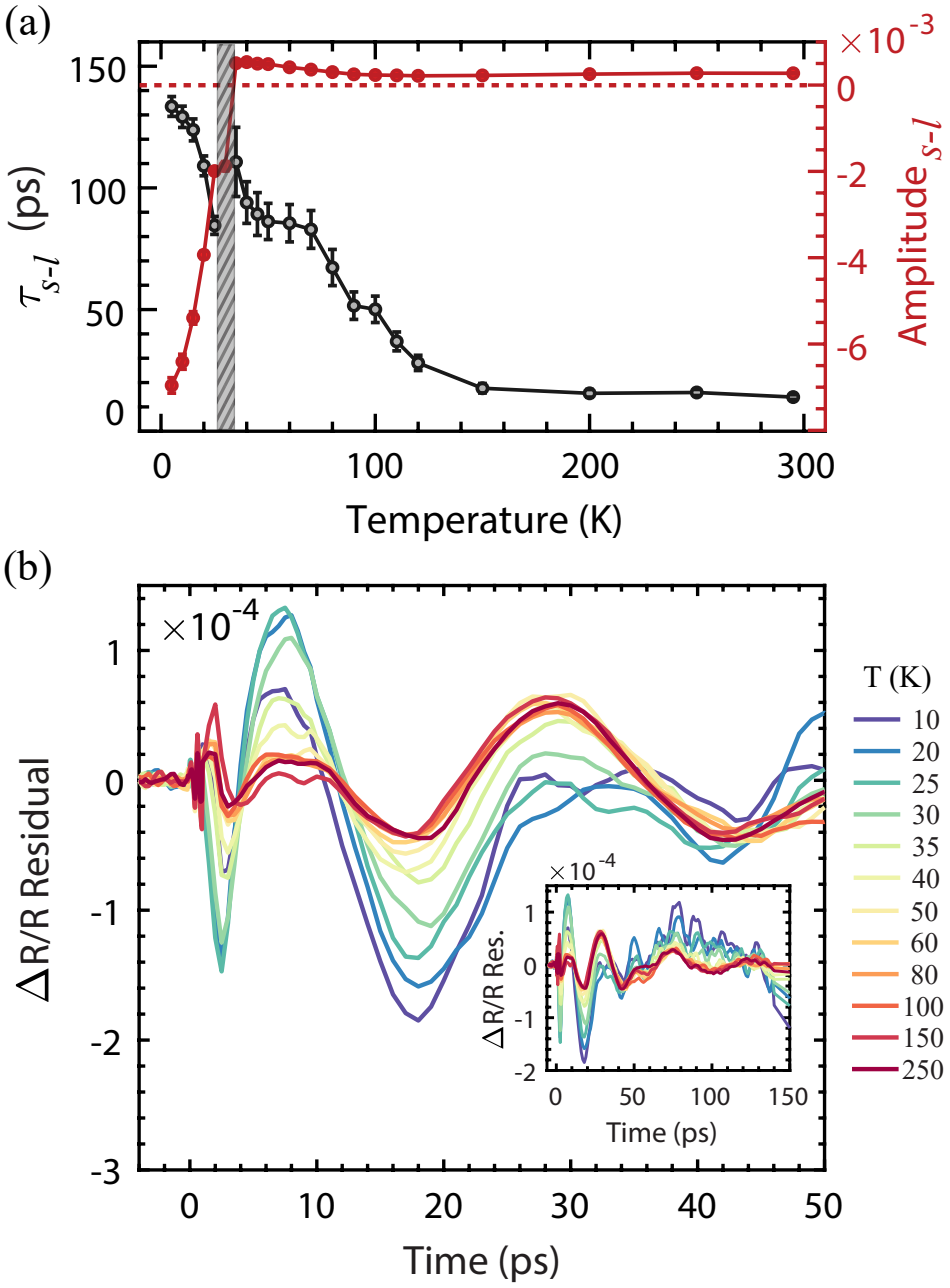

Figure 5.3: (a) Time constant (black) and amplitude (red) of the spin-lattice coupling term, extracted from exponential fits to the $\Delta R/R$ data. The vertical gray section indicates the fM transition region $T_C = 32$ K, where the lifetime is too long to measure (see 30 K curve marked by a blue star in Fig. 5.2(a)). The red dashed line depicts zero amplitude and clarifies the crossover region. (b) Coherent acoustic phonon response, isolated by subtracting the exponential fits from the $\Delta R/R$ data. The inset shows the $\Delta R/R$ residual to a longer delay time of 150 ps, where additional, higher frequency, components emerge.

lattice equilibration. It follows that this longer lifetime is related to equilibration of the spin subsystem with the lattice. The time constant measured, on the order of 100 ps in the magnetic phase, is consistent with spin-lattice coupling in other magnetic insulators [102, 103, 104]. The characteristic time is relatively constant in the paramagnetic phase until $150-200$ K, where it begins to slowly increase. This corresponds to the onset temperature ($\sim$180 K) of spin-spin coupling between the Gd^{3+} and Ti^{3+} ions [85]. Closer to 100 K τ_{s-l} further increases, indicating the onset of short-range fM spin correlations. This is also apparent in the increase in amplitude at this temperature. Finally, as T_C is crossed (dark gray region) we see evidence of the second-order ferrimagnetic phase transition as the time constant diverges and amplitude switches sign. The now-negative amplitude implies an additional rise time in the signal; as energy is transferred to spins and the ferrimagnetic order is disrupted, the system is brought further out of equilibrium. In the paramagnetic phase there is no long-range spin order to disrupt, such that spin-lattice thermalization manifests as a simple recovery to equilibrium. The critical behavior, amplitude reversal, timescale, and temperature dependence of the τ_{s-l} component all suggest that we are measuring spin-lattice coupling on a timescale of $\sim$100 ps, and that it is highly sensitive to the onset of magnetic order.

The final interesting feature of the $\Delta R/R$ data is a slow coherent oscillation, prominent at early times. By subtracting the exponential fits at each temperature we can extract the oscillatory component, plotted in Fig. 5.3(b). The result is peculiar – we observe a low-frequency phonon mode which grows in amplitude and becomes chirped, slowing down and redshifting as it propagates. The oscillation period (on the order of 20 ps), suggests an acoustic strain wave launched by the pump pulse which propagates through the crystal [58]. The probe beam reflected from the sample surface interferes with a portion reflected from the strain wave boundary, resulting in an oscillatory signal. The temperature dependence of this mode is striking – the amplitude is relatively constant at high temperatures, then grows sharply precisely at the fM phase transition temperature. Though it appears to be an acoustic mode, it is also clearly coupled to the magnetic

order. This suggests strong magneto-acoustic coupling, tying the dynamics of the magnetic subsystem to the transiently strained lattice.

To gain further insight into the magnetization dynamics and the influence upon acoustic phonon propagation, we utilize time-resolved magneto-optical Kerr effect (MOKE) spectroscopy. Fig. 5.4 presents the photoinduced Kerr rotation for all temperatures and four fields between 0.1 – 1 T. For details of the analysis, see SM IV. At lower field strengths, the signal reveals a quick rise in the photoinduced out-of-plane magnetization ΔM_z, followed by a reduction and change in sign of ΔM_z. There are two primary components to the Kerr signal, one positive (growing in $\sim$100 ps), and one negative (growing in slower, $\sim$100 – 500 ps). These dynamics are slow and long-lived, as expected in magnetic insulators like GTO due to the localized nature of quasiparticles [104]. To describe the temperature dependence of the signal, we focus on lower field strengths $H = 0.1 - 0.5$ T. At high temperature, in the paramagnetic phase, the Kerr signal is weak and indicates the lack of long-range magnetic order. As the temperature is lowered there is an increase in the photoinduced rotation, with a clear negative signal emerging below T_C. This negative component is largest and appears at earlier delays right at the transition temperature (T_C = 32 K). With decreasing temperature, the crossover to negative values of $\Delta\theta$ occurs at later times. Well below T_C, in the strongly ordered phase, the signal remains positive at all time delays.

We also observe a significant field dependence in the data. The maximum signal amplitude at all temperatures increases with increasing field. In addition, the negative amplitude component is most pronounced at 0.25 T, decreasing in amplitude at higher fields and vanishing entirely by 1 T. At this high field, we note that the photoinduced magnetization dynamics look qualitatively similar to the photoinduced reflectivity signal $\Delta R/R$ shown in Fig. 5.2(a). In the $\Delta R/R$ data, the measured signal is primarily the result of Ti sublattice dynamics due to the 1.9 eV intersite Ti-Ti excitation, and is dominated by Ti spin dynamics: the spin-lattice and spin relaxation terms (τ_{s-l} and τ_{slow}). It follows that the MOKE signal measured at 1 T is primarily a measure of Ti spin dynamics due to its similarity with the $\Delta R/R$ signal. Fits to the 1 T MOKE data support

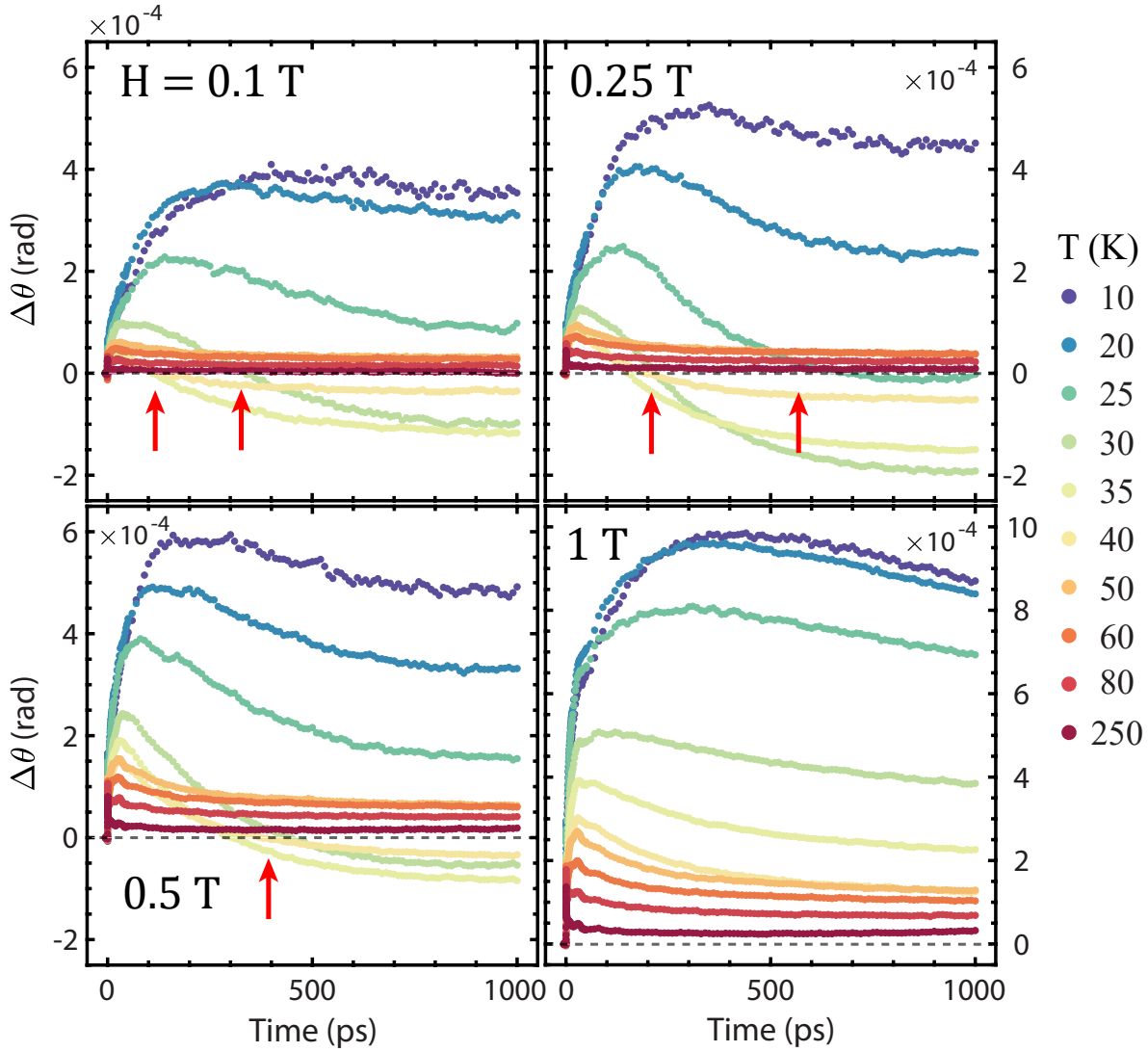

Figure 5.4: Time-resolved Kerr dynamics at various magnetic fields, recorded as the difference between the MOKE signal in opposing field directions $\Delta\theta = \Delta\theta(+H) - \Delta\theta(-H)$. This is a measure of the photoinduced change in the out-of-plane magnetization ΔM_z. Red arrows indicate the crossover to negative values of $\Delta\theta$.

this, yielding a component with a timescale of 100 – 200 ps and a very similar temperature dependence when compared to τ_{s-l} extracted from the $\Delta R/R$ data (see SM V for details). As the field is lowered from 1 T, the magnetization dynamics must be increasingly influenced by the Gd spins. The ferrimagnetic nature of GTO, with two competing magnetic sublattices, is key to understanding the observed behavior as we now discuss.

5.5 Discussion

GTO is ferrimagnetic, the Ti and Gd sublattices coupled via an AFM exchange interaction. Gd spins have a significantly larger magnetic moment than Ti, 7 μ_B vs 1 μ_B respectively [92]. Below T_C, at zero field, the two sublattices are aligned into fM domains such that there is no macroscopic moment. As the applied field H along the a-axis is increased, spins are rotated to form long-range collinear fM order, with the Gd sublattice aligned parallel to H and Ti anti-parallel. In a field of only 0.1 T saturation is approached, with spins slightly canted from the a-axis/H and a net magnetization of $M \approx 5\ \mu_B$. With increasing field, canting and spin fluctuations are reduced, increasing the net moment along H. As we approach 1 T, spin fluctuations are minimized and the magnetization becomes saturated at $M \approx 6.0\ \mu_B$ [92]. The interaction of these two competing magnetic sublattices after photoexcitation will depend on the temperature and applied field and is illustrated in Fig. 5.5(a). The 1.9 eV pump pulse directly excites the Ti sublattice, increasing Ti spin fluctuations on timescales $t < \tau_{s-l}$. This causes partial reorientation and a decrease in the projection of Ti spins along the Gd moment, corresponding to a rapid increase of ΔM_z and a rise in the MOKE signal (i.e. the Ti sublattice magnetization oriented along -z is decreased, leading to an overall increase in the net magnetization in the +z direction due to the ferrimagnetic order). Various pathways exist which may perturb the Ti spins on such timescales, including spin-orbit coupling [105, 106] (orbital order is disrupted in $t < 8$ ps, see SM III), and exchange modification, discussed below. Subsequently, energy is transferred to the Gd

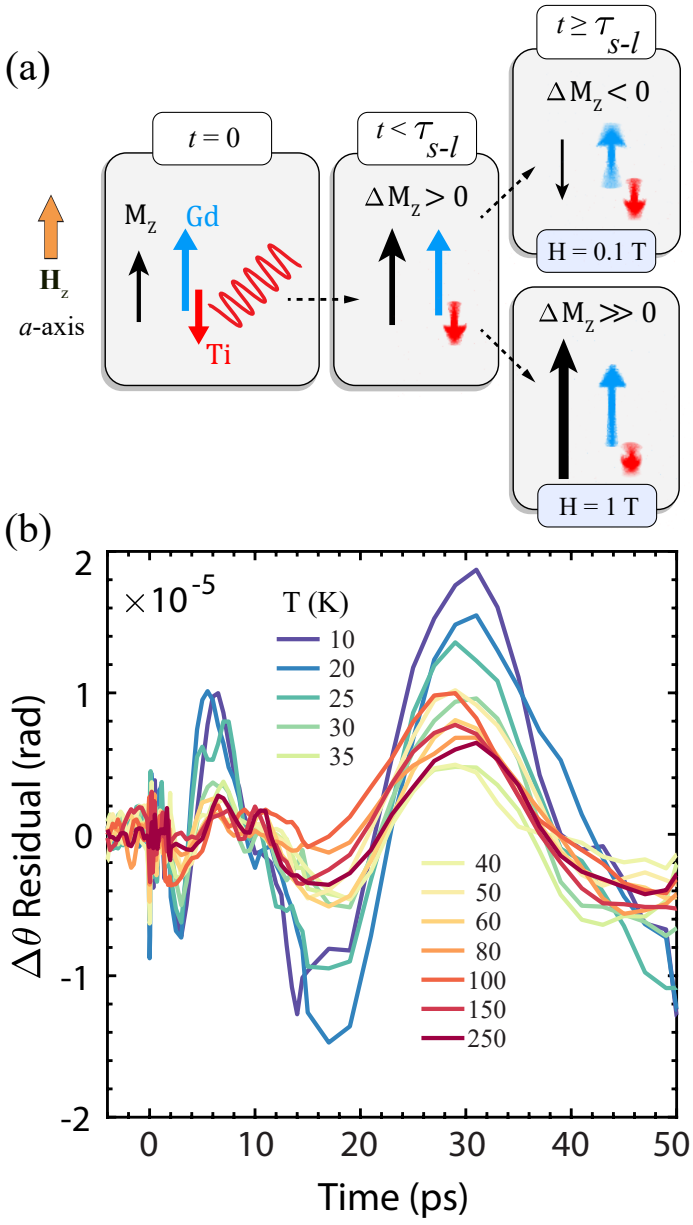

Figure 5.5: (a) Schematic depiction of the spin dynamics. Photoexcitation directly perturbs the Ti spins, which fluctuate and decrease their projection along the applied field H (parallel to a-axis, $+z$) in $t < \tau_{s-l}$ ps, increasing the MOKE signal. At longer times: if H and/or magnetic order is weak, induced spin fluctuations and the AFM exchange coupling lowers the projection of Gd spins along z. Conversely, if H is larger than the exchange field, at 1 T, Gd does not reorient and no negative component of the signal is observed. (b) Coherent acoustic phonon response, isolated by subtracting the exponential fits from the time-resolved Kerr data (at 1 T applied field). The dynamics appear similar to the $\Delta R/R$ residual, implying a common origin which we attribute to a coherent strain wave launched by the pump pulse. The appearance of this signal in the Kerr response indicates coherent acoustic phonon manipulation of the magnetic order, presumably from exchange modulation.

sublattice through spin-lattice thermalization on a timescale $t \geq \tau_{s-l}$. The spin-lattice coupling timescale of 100 – 200 ps measured from fits to the $\Delta R/R$ and MOKE data corresponds to the timescale on which the MOKE signal changes sign, indicating the delayed contribution of Gd spins to the signal. The behavior that follows is field-dependent.

At low fields, at times on the order of τ_{s-l}, the additional heat transfer and the strong AFM exchange coupling between Gd spins and partially-reoriented Ti spins causes a reduction in the Gd moment along the field direction. This is seen as the negative component, decreasing the signal on spin-lattice timescales until the net ΔM_z is negative. At higher field strengths, the applied field exceeds the AFM exchange coupling and the Gd moments are locked in place, the net magnetization only increasing as the Ti spins fluctuate and partially reorient after photoexcitation. This is true also at low temperatures where the magnetic order is more firmly established, and explains why ΔM_z goes negative only in the weakly ordered state near T_C.

Finally, we cannot discount the possibility of direct photo-induced modification of the exchange interactions. While the simplest explanation of the MOKE signal involves only heating and spin-lattice coupling, the overall heating is small (no more than $\sim$4 K at the lowest temperatures at the fluence used). It is therefore not unreasonable to consider more direct electronic changes to the system. The exchange interaction in the titanates is highly dependent on the Ti-O-Ti bond angle and degree of $GdFeO_3$ distortion, as well as the orbital order and occupation [9, 88]. GTO in particular lies on the cusp of the AFM-FM phase boundary, making it especially susceptible to changes in these parameters. Photoexcitation directly disrupts the orbital occupation, which could affect the octahedral distortion and thus the spin exchange interaction. This in turn would provide the drive for reorientation of Ti spins and change in M_z at timescales $t < \tau_{s-l}$, and for subsequent perturbation of Gd spins through exchange coupling with Ti. Further calculations of the energy scales of the Ti-Gd exchange field and corresponding timescales are required to confirm this.

To compare the magnetic dynamics to the $\Delta R/R$ response, we fit the MOKE data to a series

of exponentials similar to Eq. 5.2 and subtract the fits. Once again, a slow coherent oscillation is revealed, shown in Fig. 5.5(b) for the data taken at 1 T. The similarity of the oscillatory Kerr signal to the oscillation in $\Delta R/R$ is striking – both phonon modes have the same frequency, same time-dependent redshift, and same temperature dependence, with the amplitude growing rapidly at T_C. We rule out the possibility of a magnon – at lower fields there is no change in the frequency of oscillation as we would expect from coherent spin precession (SM VI). The amplitude is highly field-dependent however, becoming much smaller at lower fields. These observations suggest that the oscillatory mode in the MOKE signal, necessarily a magnetic phenomenon due to the nature of the measurement technique, has the same origin as the oscillatory mode in the $\Delta R/R$ signal. This is consistent with our interpretation of an acoustic strain wave with strong magneto-elastic coupling. This mechanism has been studied in a variety of ferromagnetic systems, and involves elastic stress modifying the magnetic anisotropy, which exerts a torque on the spins and alters the net magnetization [107, 108, 109].

To quantify the acoustic phonon response, we show in Fig. 5.6(a) the FFT of the full $\Delta R/R$ residual, taken from Fig. 5.3(b) (inset). The oscillatory mode with $\sim$20 ps period featured in Fig. 5.3(b) appears as a strong peak at $\sim$50 GHz. In this region of interest, it is apparent that there are additional higher frequency modes, in addition to the 50 GHz mode. The temperature dependence is also clear; while the FFT amplitude is nearly constant at high temperatures, it grows rapidly upon approaching T_C = 32 K and a higher frequency peak at $\sim$80 GHz emerges. This again suggests coupling to the magnetic order. Fig. 5.6(b) applies the same FFT analysis to data taken at an increased pump/probe wavelength of 800 nm. The features are similar, but exhibit a clear redshift as indicated by the red dashed lines. This behavior is consistent with an acoustic strain wave since it arises (for $\Delta R/R$) from interference of the probe with itself. The phonon frequency is wavelength dependent, its form is given by:

$$f = 2nv/\lambda, \tag{5.3}$$

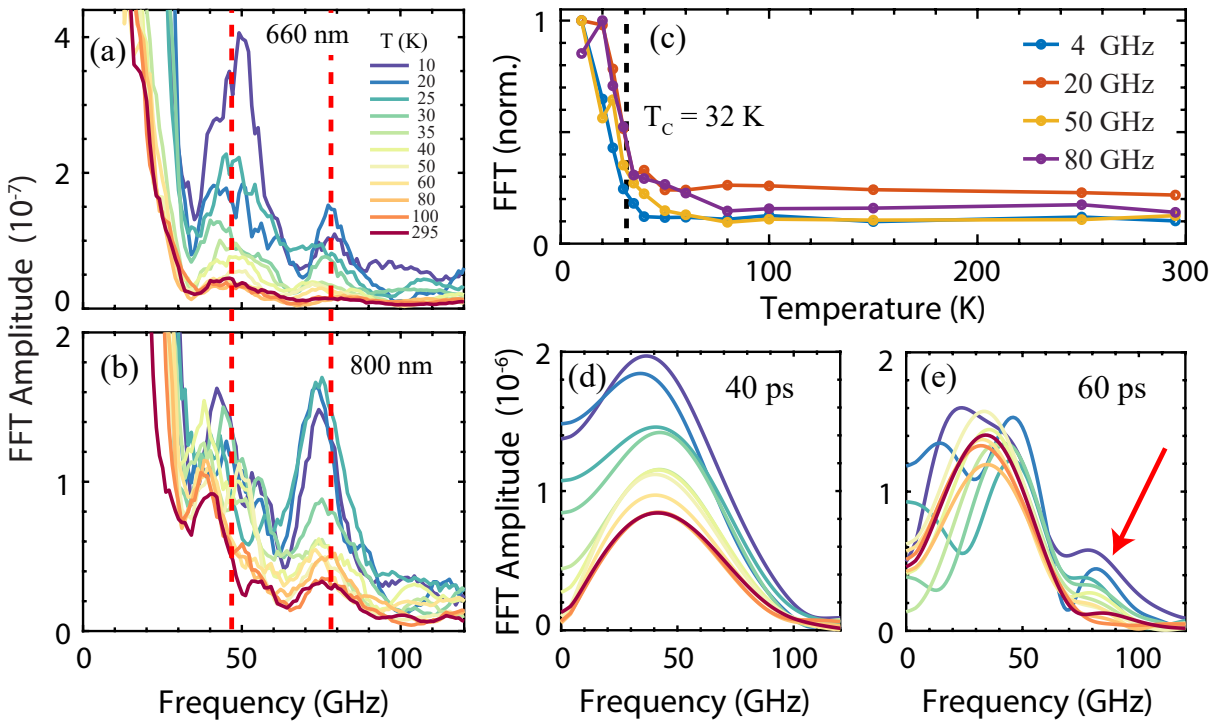

Figure 5.6: FFT amplitude of the $\Delta R/R$ residual, taken at pump/probe wavelength of 660 nm (a) and 800 nm (b). The red dashed lines indicate the approximate peak positions of the 660 nm FFT. Note the redshift to lower frequency at higher wavelength. (c) The integrated FFT amplitudes at various frequencies as a function of temperature, normalized. (d) The FFT limited to the first 40 ps and (e) 60 ps of the $\Delta R/R$ data. The higher frequency mode emerges only after 40 ps.

where n is the index of refraction, v is the sound velocity, and λ is the probe wavelength [58]. As we observe, a higher probe wavelength results in a lower frequency acoustic phonon. Using the measured index of refraction n in Fig. 5.1(b) we can also estimate the sound velocity. At the lower frequency peak near 50 GHz we obtain a sound velocity of $7.2 \times 10^3\ m/s$ and $7.7 \times 10^3\ m/s$ for a 660 and 800 nm probe, respectively. This is a very reasonable range for acoustic propagation in solid materials. These results, and the fact that the oscillation frequency does not depend on magnetic field, confirms our classification of the phonon mode as an acoustic strain wave.

To more closely examine the link to magnetism, we plot the integrated FFT amplitudes for all frequency peaks in Fig. 5.6(c). The normalized curves show a striking trend; the amplitude is nearly constant at high temperatures, but sharply increases at or very near to the magnetic

ordering transition. The temperature dependence of the FFT amplitudes follows the magnetic order parameter and is remarkably similar to the divergence one expects at a second-order magnetic phase transition. This indicates the presence of magneto-elastic coupling. The acoustic attenuation of sound waves near magnetic phase transitions is well studied, and literature suggests that the attenuation follows power law behavior, similar to our result [107]. In the vicinity of T_C, energy density and spin fluctuations play the primary role in attenuation. This behavior has been studied in a wide range of magneto-elastically coupled materials, including Ni [107], CoF_2 [110], and MnF_2 [111].

A final interesting feature to note is shown in Fig. 5.6(d-e), comparing an FFT of the $\Delta R/R$ data limited to the first 40 ps (d) and to the first 60 ps (e) of the scan. This analysis reveals that the high frequency component at 80 GHz begins to emerge only after 40 ps, which is also visible in the time-domain data (Fig. 5.3(b) inset). This timescale is similar to the spin-lattice coupling timescale measured in both $\Delta R/R$ and MOKE, which ranges from $\sim$50 – 150 ps. We have also discussed the spin dynamics following photoexcitation, where Ti spins are immediately perturbed and Gd follows after exchange pathway alterations and spin-lattice thermalization. Given the similar timescales, we suggest that the emergence of the 80 GHz mode indicates the onset of Gd spin dynamics. Roughly 50 ps after photoexcitation the Gd spin subsystem begins thermalizing and fluctuating. This damps the acoustic oscillation and changes the magnetic background. The now higher energy of the Gd spins alters the spin-phonon and magnetostrictive interaction strengths, resulting in a change to the magnetically-coupled elastic parameters of the lattice and a subsequent shift in phonon frequency.

A microscopic description of magneto-elastic coupling involves a transient modification of the exchange interaction. As the acoustic wave propagates it modulates the distance between lattice sites and spins. This in turn produces a periodic modification of the exchange interaction between neighboring spins, coupling the acoustic wave to the magnetic order parameters. The result is an attenuation of the acoustic wave in the high-temperature phase where spin fluctuations

are large, lessening as spin correlations increase in the low temperature ordered phase. The same mechanism decreases acoustic attenuation, increasing the phonon amplitude, in an applied magnetic field as observed in our MOKE signal. This has been described by an approximate analytical theory [111, 112, 113], which generally predicts maximal acoustic damping at the critical point and a MHz frequency shift in the ordered phase. We observe that the damping is consistently large throughout the high temperature paramagnetic phase, and we do not observe such a frequency shift with temperature. In our experiment, however, a MHz frequency shift is too small to be observed, and the dynamics at picosecond timescales are strongly coupled to out-of-equilibrium degrees of freedom that will affect the acoustic wave propagation and attenuation in other unanticipated ways.

The phonon behavior we observe undoubtedly suggests a strong coupling of the lattice to the magnetic order in $GdTiO_3$. Furthermore, the mechanism implies transient exchange modification on an ultrafast timescale. These conclusions are not without precedence. Ultrafast magneto-elastic coupling has been demonstrated by Bigot *et al.*, for example, in Ni thin films [114], with experiments going so far as to control the magnetic precession through acoustic pulses [115]. Kimel *et al.* have shown optical quenching of magnetic order through phonon-magnon coupling in $FeBO_3$ [104] and Nova *et al.* have shown that Mid-IR and THz excitation resonant with specific lattice modes is able to drive collective spin precession [116]. Our work represents another potential method of using light to indirectly alter the magnetic degrees of freedom on ultrafast timescales, through coupling to an acoustic phonon mode.

5.6 Conclusion

We have used a multi-modal approach, consisting of time-resolved photoinduced reflectivity and magneto-optical Kerr (MOKE) spectroscopy, to study magneto-elastic coupling in the ferrimagnetic insulator $GdTiO_3$. We observe multiple, clear signatures of the ferrimagnetically

ordered phase at T_C = 32 K in both signals, and measure spin-lattice thermalization timescales τ_{sl} on the order of 100 picoseconds, as might be expected in a magnetic insulator.

From the MOKE signal we observe long-lived spin dynamics and optical perturbation of the ferrimagnetic order. This includes a change in sign of the photoinduced magnetization on the same timescale as spin-lattice coupling. The ferrimagnetic nature of GTO, with two magnetic sublattices coupled antiferromagnetically, is responsible. Photoexcitation at 660 nm directly perturbs the Ti moments, increasing fluctuations and causing a partial reorientation and decrease in the projection of Ti spins along the Gd moment. This is measured as an increase in the MOKE signal. Heat is then transferred to the Gd subsystem through spin-lattice coupling, which when combined with the AFM exchange interaction leads to a reduction of the Gd magnetic moment along the z-direction, lowering the net magnetization. Modified exchange pathways likely also play a role in the delayed reorientation of Gd spins on these timescales. The data shows that (a) there is a delayed response of the Gd ions to the optical excitation and (b) that spin-lattice coupling and the AFM exchange interaction facilitates this.

In both the reflectivity and MOKE signals, a clear coherent acoustic phonon is present. This strain wave launched by pump is intimately tied to the sample magnetism, with an amplitude that grows sharply at T_C and closely follows the magnetic order parameter. As the acoustic wave propagates it periodically alters the distance between local spins, modifying the exchange interaction. In this way the lattice parameters are coupled to the magnetic order, which causes an attenuation of the acoustic mode near and above T_C, where spin fluctuations are large. This represents a laser-induced modification of the exchange interaction on ultrafast timescales through coupling to an acoustic phonon mode. While theory exists to describe magneto-elastic coupling, it is not particularly well-suited to the experiment and timescales measured here. A deeper theoretical understanding of the mechanisms at work would be instrumental in quantifying our results and motivating further studies. This work also suggests that more controlled excitation may be of interest in transiently controlling the properties of materials. An experiment of this

nature has already been proposed to modify the exchange interaction in GTO, using a resonant mid-IR pulse to directly excite specific phonon modes [94]. The work performed here indicates the potential for GTO, and likely other titanates, as tunable magnetic materials, and highlights the need for further investigations of this nature on the road to coherent control of materials on ultrafast timescales.

5.7 Acknowledgements

This chapter is, in full, a submission to Physical Review X in 2020. The dissertation author was the primary investigator and author of this paper. Dylan Lovinger, Eli Zoghlin, Peter Kissin, Peter Kim, Maxwell Poore, Gihyeon Ahn, Kaveh Ahadi, Susanne Stemmer, Soonjae J. Moon, Stephen. D. Wilson, Richard D. Averitt 2020.

We thank Leon Balents for helpful discussions and assistance with interpretation of the data. This work was supported primarily by ARO Award W911NF-16-1-0361 and additional support was provided by the W M Keck Foundation (SDW). The MRL Shared Experimental Facilities used for sample characterization are supported by the MRSEC Program of the NSF under Award No. DMR 1720256; a member of the NSF-funded Materials Research Facilities Network.

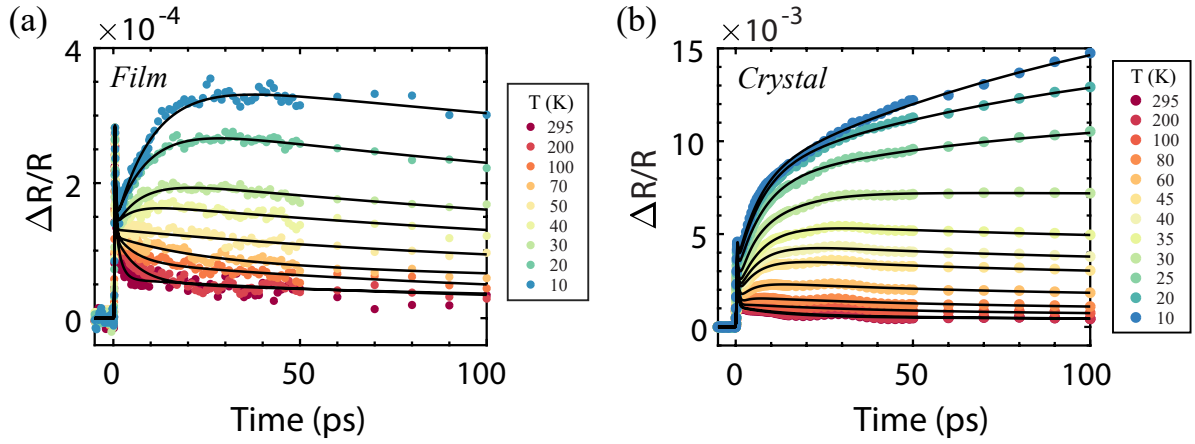

Figure 5.7: Comparison of the photoinduced differential reflectivity signal $\Delta R/R$, measured on (a) 20 nm $GdTiO_3$ thin film with 20 μJ/cm^2 pump fluence and (b) $GdTiO_3$ single crystal with 100 μJ/cm^2 pump fluence (as reported in the main text). The film data is qualitatively similar to that measured on a crystal, with less pronounced secondary rise dynamics.

5.8 Supplementary Information

5.8.1 GTO Thin Film Data

Fig. 5.7(a) presents the photoinduced reflectivity signal $\Delta R/R$ measured on a $\sim$20 nm GTO/LSAT thin film sample. Black lines represent exponential fits to the data. The dynamics in the film are qualitatively very similar to those observed in the single crystal sample, shown in Fig. 5.7(b). The primary difference is an order of magnitude smaller signal in the film and weaker secondary rise dyamics. These differences arise from the lower fluence and the lower interaction volume in the thin film sample.

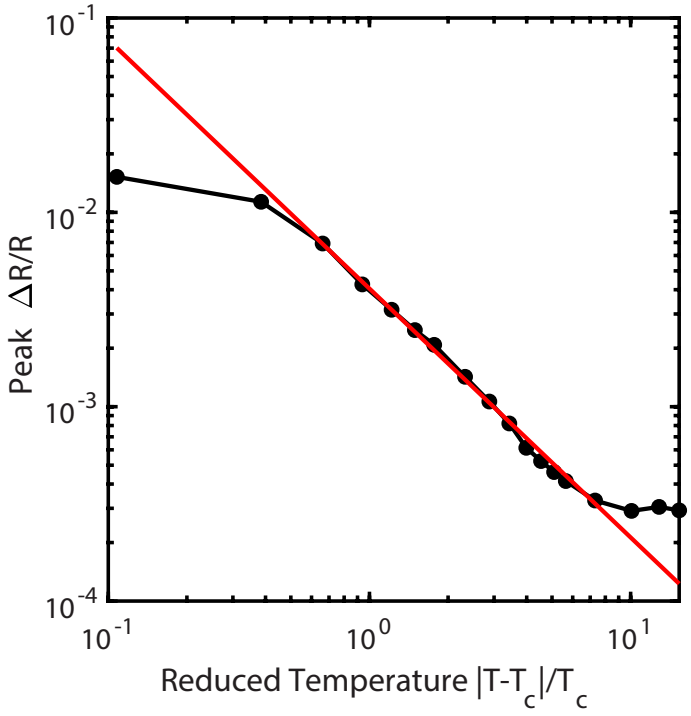

Figure 5.8: Power law fit (red) to the peak amplitude $\Delta R/R$ data (black) on a log-log scale. Linearity indicates strong power-law behavior in the temperature range above 30 K. The critical temperature T_C is found by varying its value until the best linear fit is found.

5.8.2 Power Law Fitting

The power law fit to the peak $\Delta R/R$ amplitude (Fig. 5.2(b) in the text) data takes the form $A = A_0 t^{-w}$, where w is the critical exponent and t is the reduced temperature $t = \frac{|T-T_C|}{T_C}$. The data range which the fit is applied to is 30 – 120 K. This is roughly the region in which a log-log plot of the peak $\Delta R/R$ versus reduced temperature is linear, as shown in Fig. 5.8. In this large temperature range, the fit is excellent. The value of T_C used in the reduced temperature is found by varying its value within a range near 32 K to yield the best fit, which yields $T_C = 18.05$ K. This value is lower than the nominal critical temperature of GTO, which lies closer to 32 K, but the fit is only linear above 30 K as expected. The discrepancy in T_C may be because we are only analyzing peak amplitudes of the $\Delta R/R$ signal rather than genuine magnetic dynamics.

Our power law fit yields a critical exponent $w = 1.28 \pm 0.02$. Dynamical scaling theory

allows us to relate this critical exponent, involving a dynamic parameter from time-resolved data, to static critical exponents which depend solely on the universality class of the system [66]. The relation is given simply by $w = z\nu$, where z is the generalized dynamic critical exponent and ν is the (magnetic) correlation length critical exponent. The magnetism in $GdTiO_3$ can be described by a 3-dimensional Ising model, which yields critical exponents of $z = 2.09$ [100], $\nu = 0.63$ [69], and thus $w = z\nu = 1.32$. This very nearly matches the exponent $w = 1.28 \pm 0.02$ we extract from our power law fit to the $\Delta R/R$ peak amplitude, indicating that the $\Delta R/R$ signal is sensitive to the magnetic order.

While dynamical scaling theory directly describes the behavior of a time constant, it's amplitude is often proportional to the population of carriers contributing to that time constant, resulting in a linear relationship between amplitude and time constant [68]. Thus is it is valid to perform our power law analysis on the signal amplitude and compare it to the critical exponents z and ν.

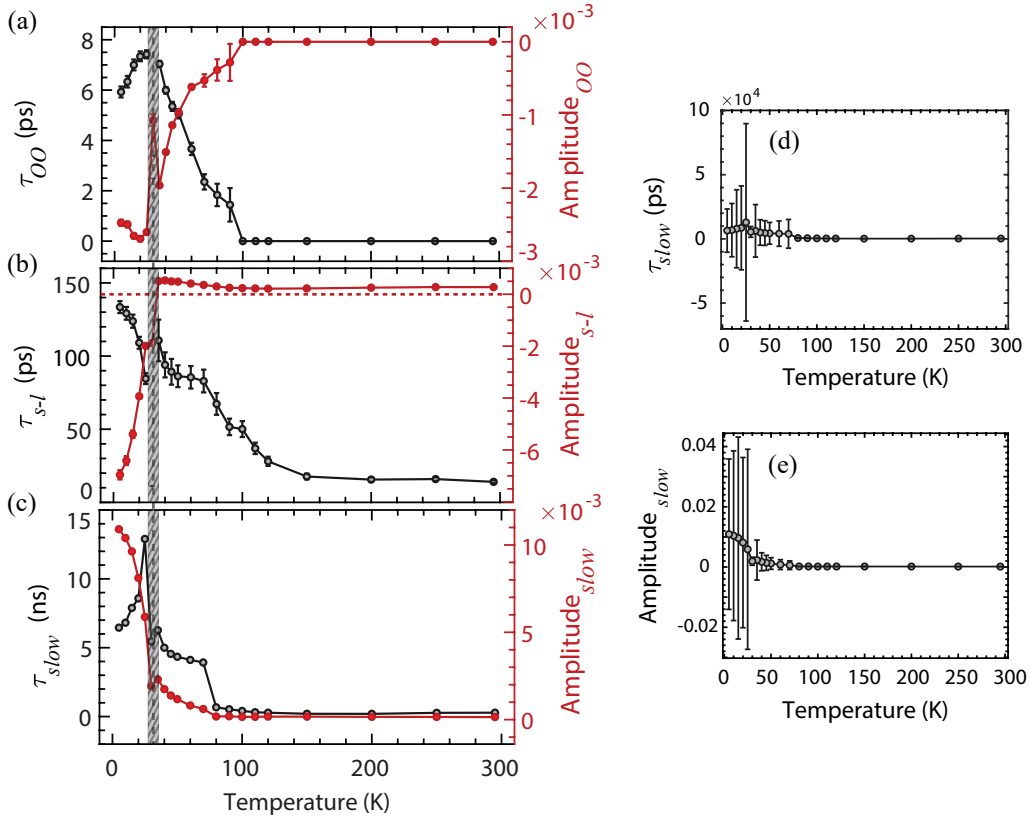

Figure 5.9: Time constants (black) and amplitudes (red) extracted from the exponential fits to the $\Delta R/R$ data. The gray vertical dashed line indicates the fM transition temperature $T_C = 32$ K. (a) is the secondary time constant and amplitude τ_{OO}, representing disruption of orbital order. (b) is the third component of the recovery τ_{s-l}, attributed to spin-lattice thermalization. The red dashed line depicts zero amplitude and clarifies the crossover region. (c) is the final component, τ_{slow}, measuring recovery of spin order. The time constant (d) and amplitude (e) for the slow component are reproduced with error bars. Large uncertainty below 70 K indicates the point where the time constant far exceeds the measured pump-probe delay time.

5.8.3 Full Fit Parameters

The full fit parameters to the reflectivity data are shown in Fig. 5.9. The data is fit to the form given in the text,

$$\Delta R/R(t) = A_{e-ph}e^{-t/\tau_{e-ph}} + A_{OO}e^{-t/\tau_{OO}} + A_{s-l}e^{-t/\tau_{s-l}} + A_{slow}e^{-t/\tau_{slow}} + C. \qquad (5.4)$$

The initial pump pulse excites an intersite Ti *3d-3d* transition, directly creating a nonequilibrium electron distribution which thermalizes via electron-electron (e-e) scattering in less than 500 fs. This is visible as the sharp rise in $\Delta R/R$ at $t = 0$. Subsequently, the first recovery term τ_{e-ph}, arises from electron-phonon (e-ph) thermalization, leading to a decrease in $\Delta R/R$. This term is relatively temperature independent, with a time constant of $\sim$0.5 ps at all temperatures. This value is consistent with e-ph relaxation in other transition metal oxides [60, 61, 62], and the relative temperature independence is further evidence that this is primarily a thermal recovery process.

Following *e-ph* recovery is a secondary rise $\tau_{OO} < 8$ ps whose amplitude (A_{OO}) and characteristic time (τ_{OO}) is plotted in Fig. 5.9(a). This term emerges only below 100 K and has a fairly monotonic increase in magnitude with decreasing temperature. There is a sharp spike at T_C = 32 K, indicating critical behavior at the transition temperature. GTO is known to display orbital order (OO) in the low temperature phase, which assists in the emergence of fM order [79, 88]. Further, in other titanates, NMR studies show signatures of OO well above the magnetic transition temperature, near 100 K in $YTiO_3$ [117, 118, 119]. The timescales involved in orbital order dynamics after photoinduced disruption are on the order of 10 ps in other perovskite Mott-Hubbard insulators [54]. The emergence of this time constant at 100 K and the similarity to literature leads us to attribute τ_{OO} to an increase in orbital disorder after photoexcitation. There is also the possibility of measuring Mott-Hubbard exciton formation dynamics, as there is an excitonic resonance at 1.95 eV found in $SmTiO_3$ and $YTiO_3$ [57], similar to the peak in optical conductivity we see in GTO. We would expect exciton formation only in the orbitally ordered state, consistent with the emergence of this time constant only at 100 K. It is likely that exciton dynamics contribute here.

The third component of the $\Delta R/R$ signal τ_{s-l} is shown in Fig. 5.9(b), with a characteristic timescale of 10 – 140 ps. This component is attributed to spin-lattice coupling and is discussed in the text.

The final component is shown in Fig 5.9(c). Error bars are extremely large and are omitted for clarity, instead reproduced in Fig. 5.9(d) and (e). With a characteristic timescale of $\sim$0.5 – 15 ns, but data that only reaches 1 ns, the fitting procedure is unable to accurately measure these time constants. Nevertheless, there are broad trends that can be discussed. Notably, the amplitude of this time constant is qualitatively similar to that of the $\Delta R/R$ peak amplitude in Fig. 2(b) of the main text, implying that A_{slow} is a significant contribution and that this term is also related to the sample magnetization. The increasing time constant and critical behavior at T_C is indicative of a second-order magnetic phase transition and further suggests that this time constant is related to the magnetic order parameter. Spin recovery dynamics slow down as long-range order onsets and spins begin to behave collectively, consistent with an increase in the lifetime. We therefore attribute τ_{slow} to the partial recovery of spin order after photoexcitation. The near-zero amplitude at high temperatures and sharp change at T_C indicates that this term is intimately related to long-range collective order of the spin system, which is near-zero in the PM phase and becomes most relevant as the fM phase boundary is crossed. In addition, the extremely slow timescale is indicative of heat diffusing out of the system, which likely also contributes to this component of the recovery. The offset at 1 ns, the furthest times measured, indicates there is still significant heat remaining in the crystal that has yet to diffuse from the probe volume.

5.8.4 MOKE Signal Analysis

We have taken multiple steps to ensure that the Kerr signal we report is genuine magnetic dynamics. Details of the Jones matrix calculations for our experiment are described earlier in Section 3.4.3.

The analysis verifies that the measurement records real magnetization dynamics. To further ensure this, we take an additional step and measure all Kerr rotations at both +H and -H applied fields, taking the difference to eliminate any signal that does not depend on H and the sample magnetization M. The final reported Kerr rotation in our work is defined as

$$\Delta\theta_{reported} = \Delta\theta_k(+H) - \Delta\theta_k(-H). \tag{5.5}$$

This ensures that the Kerr signal we measure is a probe of genuine magnetic dynamics in the sample.

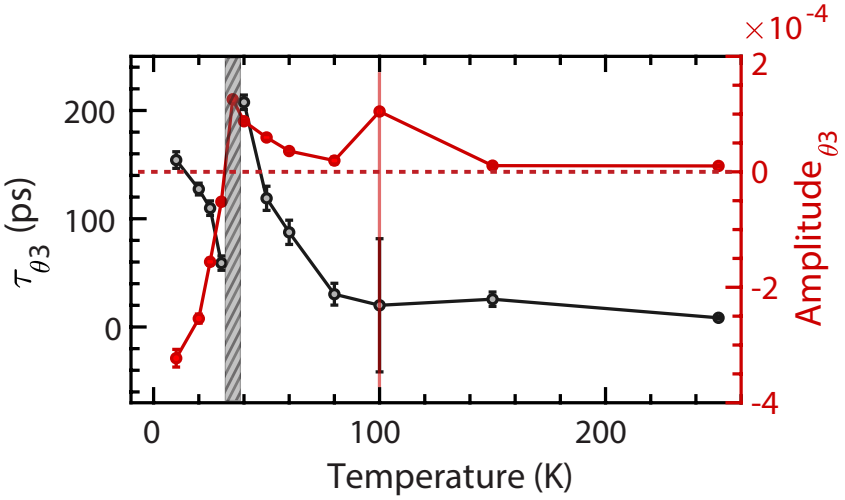

Figure 5.10: Fit parameters for the secondary rise time in the MOKE data taken at an applied field of 1 T. These are extracted from a multi-exponential fit to the data of the form given in Eq. 5.4.

5.8.5 MOKE Spin-Lattice Fit Parameters

The secondary rise time from an exponential fit to the MOKE data taken at 1 T (Fig. 5.4 in the text) is shown in Fig. 5.10. The form of the fit is identical to that used on the reflectivity data in Eq. 5.4. Both the time constant and amplitude are highly reminiscent of the $\Delta R/R$ fit parameters, following the same temperature dependence with a very similar characteristic time. For these reasons we attribute this component to spin-lattice coupling, and conclude that the dynamics are primarily determined by the excited Ti spins.

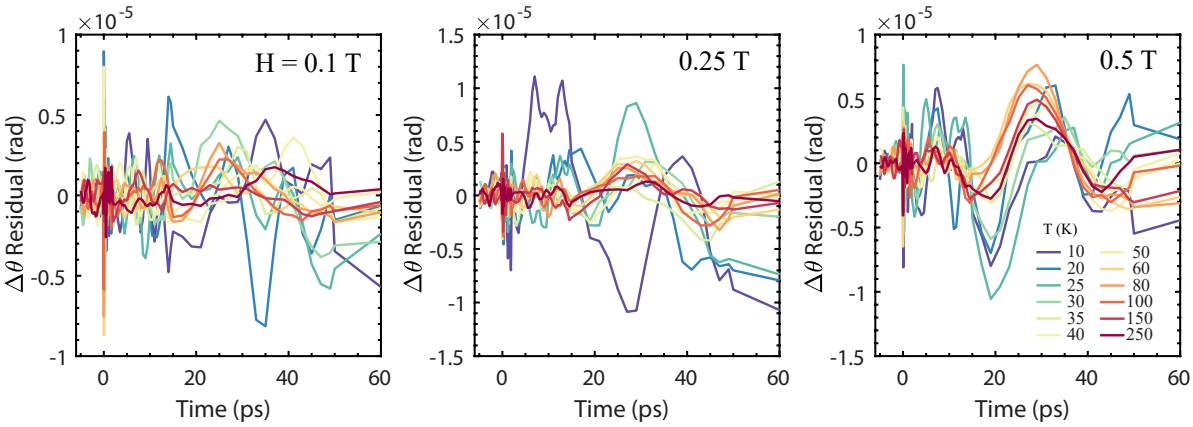

Figure 5.11: The MOKE signal residual (Kerr rotation Δθ – fit) for applied field strengths of 0.1, 0.25, and 0.5 T. The coherent oscillation is buried by noise at 0.1 T, but is visible above this field strength. The amplitude of the phonon increases with increasing field strength, but the frequency of oscillation does not.

5.8.6 Low-field MOKE Residuals

The Kerr signal residual is shown in Fig. 5.11 for the lower applied field strengths: 0.1 T, 0.25 T, and 0.5 T. At the lowest field the data is too noisy to effectively resolve the coherent oscillation, and at 0.25 T it is barely visible. At 0.5 T the acoustic mode is clearly resolved and the temperature dependence apparent. It is clear from these and the data in the main text at 1 T that the amplitude of the acoustic mode increases with increasing applied magnetic field. The frequency of oscillation does not change, ruling out magnon dynamics. This is further indication of magnetoelastic coupling to an acoustic phonon mode.

Chapter 6

Conclusion and Future Directions

The work presented in this thesis is the culmination of many years as a graduate student, yet it is merely a small contribution of knowledge to a niche within a niche of physics. However small, it is a contribution nonetheless, and this is how science progresses. The greater field of condensed matter physics, and more specifically strongly correlated materials, still contains many questions and mysteries. This work has not solved these, but it has contributed to our understanding of a few particular physical systems that will lead to further understanding still. I am proud to have contributed my work to this greater sum of knowledge.

The work on $LaVO_3$ thin films presented in Chapter 4 represents a contribution to our understanding of Mott-Hubbard exciton physics and dynamics in correlated systems undergoing simultaneous phase transitions. LVO is a Mott insulator that undergoes nearly simultaneous structural, spin, and orbital ordering below its critical temperature. In addition, bound electron-hole pairs form below T_C, excitons which interact with the ordered phases. My work provides evidence for the existence of excitons in this material, which have not been definitively proven, and suggests that their formation is induced by an interaction with the AFM spin and antiferro-orbitally ordered background. More so, this research provides insight into the ultrafast dynamics of spin and orbital order, with power-law scaling suggesting critical behavior and critical slowing

down that is often seen at a second-order phase transition. Perhaps, even, there is a conserved and universally-scaling order parameter associated with the recovery of orbital order?

LVO is a rich physical system and there are numerous follow-up studies that could be performed. As a thin film grown on a substrate, the epitaxial strain on the lattice can be controlled by choice of substrate. This very likely modifies the critical temperature, possibly separating the spin, orbital, and structural phase transitions. Indeed, a series of LVO films with varying strain has been grown and preliminary measurements taken. The data was inconclusive, but a more careful look at this series of films could prove fruitful in understanding the interplay of structural, spin, and orbital ordering in the system, and how each relates to exciton formation. Furthermore, techniques beyond optical pump-probe could be employed to more directly measure a specific degree of freedom and understand its individual behavior. For example, time-resolved angle-resolved photoemission spectroscopy (TR-ARPES) is capable of directly measuring changes in electronic occupancy and thus orbital occupancy/order after photoexcitation. This could prove as a useful method for confirming the specific orbital ordering temperature and its role in exciton formation.

The work on $GdTiO_3$ presented in Chapter 5 is a contribution to our knowledge of optical signatures of a magnetic phase transition, to ferrimagnetic sublattice dynamics after photoexcitation, and to materials with strong magneto-elastic coupling. GTO is a Mott insulator with ferrimagnetic order that is highly dependent on the lattice. My observation of Gd spin order perturbation on spin-lattice coupling timescales gives insight into how energy is transferred from the charge, then lattice, then spin degrees of freedom after photoexcitation. Furthermore, the clear correlation of an acoustic phonon amplitude to the magnetic order indicates magneto-elastic coupling that was not previously known in this material. The mechanism of this coupling is a strain-induced modification of the exchange interaction, the parameter directly responsible for the magnetic order. This work indicates a novel route to controlling the magnetism of GTO and other titanates on ultrafast timescales.

There is much potential for future studies on GTO. In the last few years there have been various theory publications detailing methods for inducing a magnetic FM-AFM transition with mid-IR excitation, resonantly pumping an octahedral phonon mode. This also represents control and modification of the magnetic exchange interaction, which my work provides an excellent background to. Our lab is now capable of reaching the 17 μm excitation wavelength required for this phonon pumping experiment. There is also still potential Floquet engineering of GTO, using the period electric field of a laser pulse to directly drive electronic changes. The rare-earth titanates in general are a rich system for study. With magnetic order that is highly tied to the lattice, it is likely that other titanates display magneto-elastic coupling. This is an entire class of material with great potential for light-induced magnetic control, and should be studied in further detail.

Optical physics, especially ultrafast time-resolved spectroscopy in all its forms, is one of the newest and most promising modern fields of study. It enables us to probe dynamics at the most fundamental timescales, and it continues to constantly improve. Growing laser powers and modern techniques enable wider and more easily accessible spectral ranges, and shortening pulses enable continually improved time resolution. I am also excited to see how these improvements can be applied to technology, particularly in ultrafast optical control of materials. Switchable conducting and magnetic states on picosecond timescale has massive potential in optical memory, circuitry, and quantum computing, and may be the future of advanced electronics. It is my hope that the work I have done will provide even a slight contribution to these sciences. That it will provide a background to other researchers studying these materials or related phenomena, and to future students in the Averitt group. That I will be the shoulders upon which some future scientists stand.

Appendix A

Fitting Routine

This chapter details the use of the fitting routine introduced in Sec. 3.5. The matlab fitting routine is based on a Nelder-Meade triangulation algorithm and is intended to efficiently fit large sets of data with minimal input. Full datasets with an arbitrary number of runs will be fit in the same execution of the program. The matlab .m file, along with a sample set of data, can be found in the Averitt group folder under .../Averitt Group/Matlab/Fitting/NM_Data_Fitting_Routine.m. By default it is configured to fit to a series of n exponentials, but any functional form can be provided. The following sections describe the required inputs to run the program, and the usable outputs.

A.1 Inputs

This section describes the necessary inputs to run the fitting routine, and the data formats. Fig. A.1 (a) shows the data input section of the program. The filepath the .dat data file is specified in line 27. It is recommended to keep data in a personal Drive folder, to preserve data and for ease of access across devices. The file itself is loaded from line 33. The format of the data file is shown in Fig. A.1 (b). It is an $n \times m$ array, where the rows n represent individual $\Delta R/R$ readings at each pump-probe delay time, and the columns m represent different temperatures. The temperatures

(a)

```
%% Input - Filepaths

% enter filepath to data files:
cd 'D:\User Files\Google Drive\Averitt Group\Matlab\Fitting\NM Example Data';

% load datasets:
% format as a nxm array, where rows n represent each time point, and
%   columns m represent each temperature measured, in order of increasing
%   temperatures (m = 1 is low temp)
dataset1 = load('GTO_Kerr_660_bAxisPump_Dataset1_1T_example.dat');

% load time array:
% format as a single nx1 array, where n is the number of time points
timearray1 = load('timeGTOKerrbPump.dat');

% define dataset to use, useful if loading multiple datasets at once
t = timearray1;
dataArray = dataset1;

% define temperature array
% should be length m, the number of columns in dataset1
temps = [10, 20, 25, 30, 35, 40, 50, 60, 80, 100, 150, 250];
```

(b)

dataset1:

10 K	20 K	25 K	30 K	35 K	40 K	50 K	60 K	80 K	100 K	150 K	250 K
-6.6857e-08	9.2783e-07	1.3181e-06	-1.4121e-06	-8.7377e-07	6.1474e-07	9.1708e-07	1.5106e-07	5.7239e-07	3.9028e-07	5.7431e-07	-3.7927e-07
-1.4107e-06	-1.2399e-06	1.0268e-06	-2.0573e-07	-3.4788e-07	1.1979e-08	-2.3940e-06	-9.5848e-08	-1.4236e-06	-4.1724e-07	1.6182e-07	-5.9165e-07
3.8870e-07	6.7488e-07	1.0121e-06	-8.7732e-07	6.0212e-08	-4.3479e-07	-2.2129e-07	-1.1628e-06	-1.0664e-06	-1.3390e-06	4.9639e-07	8.4646e-07
-2.5024e-07	8.5431e-07	1.6651e-06	-1.4987e-06	-8.3834e-07	-3.6967e-06	-5.7288e-07	-4.9480e-07	1.7717e-07	-5.4754e-07	1.0002e-06	1.2122e-06
6.6796e-07	9.6842e-07	-1.3062e-07	5.9253e-07	1.2175e-06	-1.7769e-06	-5.8441e-08	-1.0209e-06	1.0649e-07	-5.9262e-07	-3.5657e-07	7.4306e-08
7.0531e-07	1.5825e-07	1.7994e-07	-3.5777e-07	2.3668e-06	-2.1079e-07	1.5814e-06	1.7923e-07	5.0299e-07	1.1667e-06	-1.4176e-06	-3.3845e-07
-1.1472e-06	-1.4493e-06	-1.4149e-06	-8.5133e-07	6.2988e-07	6.1176e-07	1.9947e-06	-6.9376e-07	1.3607e-07	-2.8448e-07	-1.5819e-06	-3.2442e-07
1.0270e-06	-1.2162e-06	-1.8866e-06	7.6320e-07	-8.2396e-07	-7.0701e-07	7.1077e-07	1.8941e-07	9.8690e-07	1.3770e-06	3.9641e-07	8.5039e-08
7.7983e-07	-1.1528e-07	5.5699e-07	1.2714e-06	-8.3761e-07	1.5827e-06	3.4559e-08	7.7066e-07	5.6941e-08	4.0053e-07	-9.4908e-07	-8.7355e-07
-5.5479e-07	1.7680e-06	-1.6696e-06	2.0462e-06	-4.8111e-07	2.5496e-06	-3.8516e-07	3.1343e-07	-1.7116e-07	1.3783e-06	-4.5208e-08	-3.4997e-07
⋮											

Figure A.1: Data inputs and formats for the Nelder-Meade matlab fitting routine. (a) lines specifying loading of pump-probe data set and corresponding time array. A temperature array is also manually input here. (b) example of the data set format.

```
49      %% Fitting Routine Parameters
50      % (0 = off, 1 = on)
51
52 -    terms = 4;              %number of exponential terms
53 -    startingRun = 12;       %which run (temp) to start from. Fitting routine starts goes from high temp to low
54 -        endingRun = 1;      %which run to end on
55
56 -    constrain = 1;          %constrain coefficients to be btwn lb & ub
57 -    lsq_constrain = 0;      %strict constraint, final values will not exceen designated upper/lower bounds
58 -    constrain_const = 0;    %strict constraint on constant offset term
59 -    iterations = 8;         %how many times to repeat the Nelder-Meade algorithm loop at each temperature
60 -    fitRange = 0;           %fit only a specified data range
61 -        lowCutoff = 2.5;    %lower cutoff (in ps)
62 -        highCutoff = 45;    %upper cutoff (in ps)
63
64      %less useful parameters
65 -    multi_temp = 1;         %Repeat for each temperature run
66 -    smoothing = 0;          %Smooth data. Might lead to incorrect errors
67 -    weighted_fit = 0;       %Weight the beginning of the data (not working)
68 -    rescale = 1;            %Rescale the data, yields better fits when working with decimal data values. Keep on
69 -        scaling = 100000;   %Amount to scale everything by
70 -    repeat_num = 1;         %Repeat everything this many times
```

Figure A.2: Fitting routine parameters, detailing the various options to change the behavior of the fitting routine.

should be arranged in ascending order, and should match the temperature array defined in line 45. In line 37 of Fig. A.1 (a), the time array is loaded. This should be an $n \times 1$ array of time steps, corresponding to the n rows of "dataset1". Multiple data sets and time arrays can and should be loaded simultaneously. The data set that will be fit by the program is defined in lines $40-41$.

Following data input is a section with options to change the fitting behavior. These fitting routine parameters are shown in Fig. A.2. Line 52 "terms" is the number of exponential terms to fit the data to. By default, data is fit to a series of exponentials of the form:

$$\Delta R/R = \left(A_1 e^{-t/\tau_1} + A_2 e^{-t/\tau_2} + \ldots + A_n e^{-t/\tau_n} + C\right) erfc\left(\frac{t-\tau_{erf0}}{A_{erf0}}\right), \tag{A.1}$$

where τ is a time constant, A is an amplitude, C is a constant offset, and *erfc* is the error function with corresponding time and amplitude, modeling the step-like rise in signal amplitude at $t = 0$. The number n of exponential terms corresponds to the numerical value of "terms" defined in line 52 of the program. The functional form of the fits can be modified on line 220.

Line 53 defines which data run, or temperature run, to start fitting from. The program works in descending order, fitting high temperature data first and moving to low temperature.

In the example, pump-probe data was taken at separate 12 temperatures. Defining "startingRun = 12" will start the fititng procedure at the 12th and last column of the input data dataset1, the highest temperature. The definition of "endingRun" in the following line tells the program at which run to stop fitting. A value of 1 means it will fit down to the lowest temperature.

The following lines are various control parameters for the fitting procedure. For a binary option, 0 turns the feature off and 1 turns it on. The options are defined as follows:

- "constrain" - places a loose constraint on the upper and lower bounds of the fit parameters, which are user-defined in the following section
- "lsq_constrain" - places tight bounds on the fit parameters, such that they cannot exceed the specified bounds
- "constrain_const" - places tight bounds on the constant offset term C
- "iterations" - number of times the program repeats the Nelder-Meade algorithm at each data run or temperature. Or how many times it will triangulate and optimize the position in parameter space. This is the fitting procedure's only stopping condition. A value higher than 16 is typically unnecessary.
- "fitRange" - specify whether to fit the entire pump-probe time range (0), or to fit only within a given range (1). If (1), "lowCutoff" and "highCutoff" define the fit range, specified in picoseconds.

The remaining options are of less use and are described briefly in the program. Smoothing is sometimes useful on particularly noisy data sets to find working fit parameters, but will yield inaccurate errors on the final fit parameters.

The final section for data input is for defining the fit parameter initial conditions and bounds. This starts on line 93. There is a different set of parameters for each different number of exponential terms that can be defined. Users must input a set of initial conditions in "tau0", a

set of lower bounds on the fit parameters in "lb", and a set of upper bounds in "ub". These are formatted in the following order:

$$tau0 = \begin{bmatrix} C & \tau_1 & \tau_2 & \dots & \tau_n & A_1 & A_2 & \dots & A_n & \tau_{erf0} & A_{erf0} \end{bmatrix}, \qquad \text{(A.2)}$$

where n is the number of exponential terms, and the parameters are as defined in Eq. A.1. A reasonable set of upper and lower bounds is essential to obtaining good fits, but even a very wide range of bounds can be used to converge on a fit.

A.2 Outputs

This section details the usable outputs of the fitting routine. As the program runs, the output figure 1 shows the fit progress in real time, adjusting the fit at each iteration of the algorithm. After the fit of each run/temperature is complete, a new figure is output to record it, labelled with the corresponding temperature. At the end of the fitting routine, after each run is fit, the fits at each temperature are displayed. An example is shown in Fig. A.3 (a) for a 4-exponential fit. The program can be stopped at any time by typing "ctrl+c" into the command window. The full full fits will not be displayed, but the output below will.

The fits displayed in Fig. A.3 (a) are output in matlab variable "fit_array_final". Assuming that all runs/temperatures are fit, this is an $n \times m$ array where rows n is the number of pump-probe time steps and columns m is the number of runs/temperatures. The columns are arranged in the order they were fit, thus descending order from high temperature ($m = 1$) to low. The fits can be plotted along with the time array given as an initial input.

The fit parameters are output in matlab variable "tau_array_final". An example of the fit parameters for a 3-exponential fit (terms = 3) is shown in Fig. A.3 (b). This is formatted as an $(N*2+1) \times m$ array, where N is the number of entries in the variable tau0 defined in Eq. A.2 ($tau0 = terms*2+3$) and the columns m again represent each run/temperature that was fit in

(a)

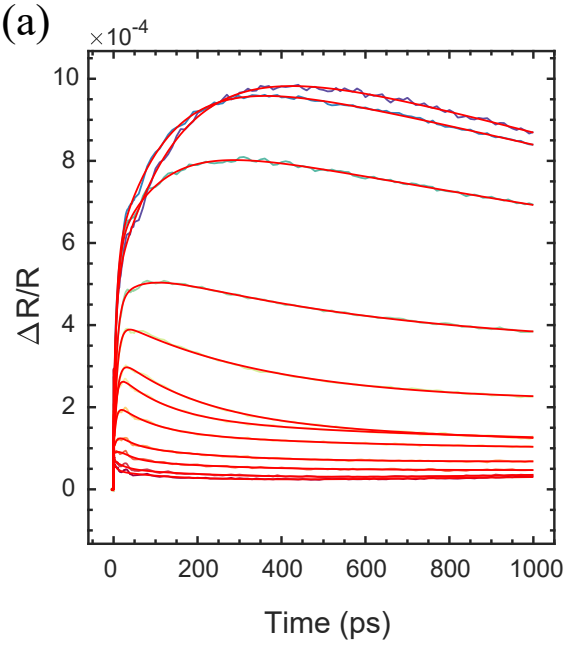

(b)

		250 K	150 K	100 K	80 K
		1	2	3	4
C	1	1.3258e-05	1.6052e-05	2.2637e-05	3.4478e-05
τ_1	2	0.1023	0.3930	0.3556	0.4957
τ_2	3	0.6786	5.3493	98.3949	3.6265
τ_3	4	49.0540	96.4622	438.2565	156.8419
A_1	5	0.0045	1.4937e-04	1.7465e-04	1.2595e-04
A_3	6	5.5936e-05	7.0574e-06	1.7013e-05	-2.2288e-05
A_2	7	1.4645e-05	1.5698e-05	6.9466e-06	2.9772e-05
τ_{erf0}	8	0.4155	0.2843	0.3004	0.2811
A_{erf0}	9	-0.1789	-0.1853	-0.1842	-0.1781
	10	0	0	0	0
σ C	11	1.1972e-07	1.4620e-07	1.6203e-06	1.6114e-07
τ_1	12	0.0173	0.0241	0.0133	0.0307
τ_2	13	0.0585	1.6739	22.2807	0.4036
τ_3	14	3.1630	7.6982	464.7375	4.6958
A_1	15	0.0073	1.2298e-05	1.2474e-05	6.1609e-06
A_3	16	7.6576e-06	1.0840e-06	5.1752e-06	2.1167e-06
A_2	17	3.5685e-07	6.4101e-07	3.8395e-06	3.3598e-07
τ_{erf0}	18	0.0848	0.0062	0.0050	0.0041
A_{erf0}	19	0.0137	0.0045	0.0038	0.0036

Figure A.3: Fitting routine outputs. (a) plot of all fits output by the fitting routine, overlaid on the original data. (b) fit parameter outputs found in the variable "tau_array_final".

descending order. The rows are the fit parameters and their errors. The first N represent the values of the fit parameters, in the same order as given in Eq. A.2. These are followed by a 0 as separator, then the last N represent the error on each of these fit parameters, in the same order. The error is defined by a 95% confidence interval (ci) using the Jacobian and fit residual, calculated as

$$\sigma_{error} = \frac{ci_{high} - ci_{low}}{2 * 1.96} \tag{A.3}$$

This is equivalent to $1.96\frac{\sigma}{\sqrt{n}} = 1.96 * SE$, where SE is the standard error. The value 1.96 represents that 95% of the area in a normal distribution is within 1.96 standard deviations from the mean.

Bibliography

[1] D. N. Basov, R. D. Averitt, D. van der Marel, M. Dressel, and K. Haule, "Electrodynamics of correlated electron materials," *Rev. Mod. Phys.*, vol. 83, pp. 471–541, jun 2011.

[2] D. N. Basov and T. Timusk, "Electrodynamics of high-T_C superconductors," *Rev. Mod. Phys.*, vol. 77, pp. 721–779, aug 2005.

[3] M. Imada, A. Fujimori, and Y. Tokura, "Metal-insulator transitions," *Rev. Mod. Phys.*, vol. 70, pp. 1039–1263, oct 1998.

[4] L. D. Landau, L. P. Pitaevskii, and E. Lifshitz, *Electrodynamics of Continuous Media*. London, U.K.: Butterworth-Heinemann, 2nd editio ed., 1984.

[5] W. J. Padilla, "Light–Matter Interactions," in *Opt. Tech. Solid-State Mater. Charact.* (R. P. Prasankumar and A. J. Taylor, eds.), Boca Raton, FL: CRC Press, 2012.

[6] D. I. Khomskii, "Localized and itenerant electrons in solids," in *Transit. Met. Compd.*, ch. Localized, pp. 1–24, Cambridge: Cambridge University Press, 2014.

[7] J. Hubbard, "Electron correlations in narrow energy bands," *Proc. R. Soc. London. Ser. A. Math. Phys. Sci.*, vol. 276, pp. 238–257, nov 1963.

[8] P. W. Ma, S. L. Dudarev, and C. H. Woo, "Spin-lattice-electron dynamics simulations of magnetic materials," *Phys. Rev. B*, vol. 85, no. 18, pp. 30–37, 2012.

[9] M. Mochizuki and M. Imada, "Magnetic Phase Transition of the Perovskite-Type Ti Oxides," *J. Phys. Soc. Japan*, vol. 69, no. 7, pp. 1982–1985, 2000.

[10] P. Bordet, C. Chaillout, M. Marezio, Q. Huang, A. Santoro, S.-W. Cheong, H. Takagi, C. Oglesby, and B. Batlogg, "Structural Aspects of the Crystallographic-Magnetic Transition in $LaVO_3$ around 140 K," *J. Solid State Chem.*, vol. 106, pp. 253–270, oct 1993.

[11] S. M. Miyasaka, Y. Okimoto, and Y. Tokura, "Anisotropy of Mott–Hubbard Gap Transitions due to Spin and Orbital Ordering in $LaVO_3$ and YVO_3," *J. Phys. Soc. Japan*, vol. 71, no. 9, pp. 2086–2089, 2002.

[12] E. Abreu, S. N. Gilbert Corder, S. J. Yun, S. Wang, J. G. Ramírez, K. West, J. Zhang, S. Kittiwatanakul, I. K. Schuller, J. Lu, S. A. Wolf, H.-T. Kim, M. Liu, and R. D. Averitt, "Ultrafast electron-lattice coupling dynamics in VO_2 and V_2O_3 thin films," *Phys. Rev. B*, vol. 96, p. 094309, sep 2017.

[13] H. E. Stanley, *Introduction to phase transitions and critical phenomena*. Oxford University Press, 1987.

[14] K. F. Tseng, *Critical Dynamics in Classical Antiferromagnets*. Doctoral thesis, Max Planck Institute for Solid State Research, 2016.

[15] L. Onsager, "Crystal Statistics. I. A Two-Dimensional Model with an Order-Disorder Transition," *Phys. Rev.*, vol. 65, pp. 117–149, feb 1944.

[16] M. Campostrini, M. Hasenbusch, A. Pelissetto, P. Rossi, and E. Vicari, "Critical exponents and equation of state of the three-dimensional Heisenberg universality class," *Phys. Rev. B*, vol. 65, p. 144520, apr 2002.

[17] A. Pelissetto and E. Vicari, "Critical phenomena and renormalization-group theory," *Phys. Rep.*, vol. 368, pp. 549–727, oct 2002.

[18] M. Scheffer, J. Bascompte, W. A. Brock, V. Brovkin, S. R. Carpenter, V. Dakos, H. Held, E. H. van Nes, M. Rietkerk, and G. Sugihara, "Early-warning signals for critical transitions," *Nature*, vol. 461, pp. 53–59, sep 2009.

[19] P. C. Hohenberg and B. I. Halperin, "Theory of dynamic critical phenomena," *Rev. Mod. Phys.*, vol. 49, pp. 435–479, jul 1977.

[20] T. Kise, T. Ogasawara, M. Ashida, Y. Tomioka, Y. Tokura, and M. Kuwata-Gonokami, "Ultrafast Spin Dynamics and Critical Behavior in Half-Metallic Ferromagnet: Sr_2FeMoO_6," *Phys. Rev. Lett.*, vol. 85, no. 9, pp. 1986–1989, 2000.

[21] V. V. Krishnamurthy, I. Watanabe, K. Nagamine, H. Kuwahara, and Y. Tokura, "Critical spin dynamics in $Nd_{1-x}Sr_xMnO_3$ with x = 0.5," *Phys. Rev. B*, vol. 61, no. 6, p. 4060, 2000.

[22] C. Meisel, A. Klaus, C. Kuehn, and D. Plenz, "Critical Slowing Down Governs the Transition to Neuron Spiking," *PLOS Comput. Biol.*, vol. 11, no. 2, pp. 1–20, 2015.

[23] M. Eichberger, H. Schäfer, M. Krumova, M. Beyer, J. Demsar, H. Berger, G. Moriena, G. Sciaini, and R. J. D. Miller, "Snapshots of cooperative atomic motions in the optical suppression of charge density waves," *Nature*, vol. 468, no. 7325, pp. 799–802, 2010.

[24] A. Kowalevicz, "Ultrashort Pulse Generation and Measurement," in *Opt. Tech. Solid-State Mater. Charact.* (R. P. Prasankumar and A. J. Taylor, eds.), pp. 237– 289, Boca Raton, FL: CRC Press, 2012.

[25] D. Misemer, "The Effect of Spin-Orbit Interaction and Exchange Splitting on Magneto-Optic Coefficients," *J. Magn. Magn. Mater.*, vol. 72, pp. 267–274, 1988.

[26] H. Tanaka, *Development of MOKE Spectrometer for Magneto-optical Studies of Novel Magnetic Materials and Quantum Structures*. PhD thesis, Ohio University, 2008.

[27] Z. Q. Qiu and S. D. Bader, "Surface magneto-optic Kerr effect," *Rev. Sci. Instrum.*, vol. 71, no. 3, pp. 1243–1255, 2000.

[28] J. Wang, "Time-Resolved Magneto-Optical Spectroscopy," in *Opt. Tech. Solid-State Mater. Charact.* (R. P. Prasankumar and A. J. Taylor, eds.), Boca Raton, FL: CRC Press, 2012.

[29] R. C. Jones, "A New Calculus for the Treatment of Optical Systems I. Description and Discussion of the Calculus," *J. Opt. Soc. Am.*, vol. 31, pp. 488–493, jul 1941.

[30] M. Veis, *Optical interactions in thin films of selected magnetic oxides*. Doctoral thesis, Charles University, Prague, 2009.

[31] D. S. Kliger, J. W. Lewis, and C. E. Randall, "Introduction to the Jones Calculus, Mueller Calculus, and Poincare Sphere," in *Polariz. Light Opt. Spectrosc.* (D. S. Kliger, J. W. Lewis, and C. E. Randall, eds.), pp. 59–101, Boston: Academic Press, 1990.

[32] M. Nyvlt, *Optical interactions in ultrathin magnetic film structures*. Thesis, Charles University, Prague, 1996.

[33] J. A. Nelder and R. Mead, "A Simplex Method for Function Minimization," *Comput. J.*, vol. 7, pp. 308–313, jan 1965.

[34] M. D. Raychaudhury, E. Pavarini, and O. K. Andersen, "Orbital Fluctuations in the Different Phases of $LaVO_3$ and YVO_3," *Phys. Rev. Lett.*, vol. 99, no. 12, p. 126402, 2007.

[35] S. Y. Park, A. Kumar, and K. M. Rabe, "Charge-Order-Induced Ferroelectricity in $LaVO_3/SrVO_3$ Superlattices," *Phys. Rev. Lett.*, vol. 118, p. 087602, feb 2017.

[36] G. Jackeli and G. Khaliullin, "Spin, Orbital, and Charge Order at the Interface between Correlated Oxides," *Phys. Rev. Lett.*, vol. 101, p. 216804, nov 2008.

[37] J. Varignon, N. C. Bristowe, E. Bousquet, and P. Ghosez, "Coupling and electrical control of structural, orbital and magnetic orders in perovskites," *Sci. Rep.*, vol. 5, no. 1, p. 15364, 2015.

[38] F. Novelli, D. Fausti, J. Reul, F. Cilento, P. H. M. van Loosdrecht, A. A. Nugroho, T. T. M. Palstra, M. Grüninger, and F. Parmigiani, "Ultrafast optical spectroscopy of the lowest energy excitations in the Mott insulator compound YVO_3: Evidence for Hubbard-type excitons," *Phys. Rev. B*, vol. 86, p. 165135, oct 2012.

[39] J. Reul, A. A. Nugroho, T. T. Palstra, and M. Grüninger, "Probing orbital fluctuations in RVO_3 (R = Y, Gd, or Ce) by ellipsometry," *Phys. Rev. B*, vol. 86, no. 12, p. 125128, 2012.

[40] M. Kim, "Signatures of spin-orbital states of t_{2g}^2 system in the optical conductivity: The case of RVO_3 (R = Y and La)," *Phys. Rev. B*, vol. 97, no. 15, p. 155141, 2018.

[41] Z. Lenarčič and P. Prelovšek, "Ultrafast Charge Recombination in a Photoexcited Mott-Hubbard Insulator," *Phys. Rev. Lett.*, vol. 111, p. 016401, jul 2013.

[42] P. Prelovšek and Z. Lenarčič, "Charge relaxation and recombination in photo-excited Mott insulators," *Int. J. Mod. Phys. B*, vol. 30, p. 1642015, may 2016.

[43] P. Wróbel and R. Eder, "Excitons in Mott insulators," *Phys. Rev. B*, vol. 66, p. 035111, jul 2002.

[44] D. G. Sahota, R. Liang, M. Dion, P. Fournier, H. A. Dąbkowska, G. M. Luke, and J. S. Dodge, "Many-body recombination in photoexcited insulating cuprates," *Phys. Rev. Res.*, vol. 1, p. 033214, dec 2019.

[45] M. L. Schneider, J. Demsar, Y. Glinka, A. Klimov, A. Krapf, S. Rast, Y. H. Ren, W. Si, Y. Xu, X. H. Zeng, I. Bozovic, G. Lüpke, R. Manzke, R. Sobolewski, A. T. Taylor, N. H. Tolk, X. X. Xi, R. Joynt, and M. Onellion, "Ultrafast carrier relaxation dynamics in single-layer cuprates," *Europhys. Lett.*, vol. 60, pp. 460–466, nov 2002.

[46] I. M. Vishik, F. Mahmood, Z. Alpichshev, N. Gedik, J. Higgins, and R. L. Greene, "Ultrafast dynamics in the presence of antiferromagnetic correlations in electron-doped cuprate $La_{2-x}Ce_xCuO_4$," *Phys. Rev. B*, vol. 95, p. 115125, mar 2017.

[47] A. I. Lobad, R. D. Averitt, C. Kwon, and A. J. Taylor, "Spin-lattice interaction in colossal magnetoresistance manganites," *Appl. Phys. Lett.*, vol. 77, no. 24, pp. 4025–4027, 2000.

[48] J. Zhang, X. Tan, M. Liu, S. W. Teitelbaum, K. W. Post, F. Jin, K. A. Nelson, D. N. Basov, W. Wu, and R. D. Averitt, "Cooperative photoinduced metastable phase control in strained manganite films," *Nat. Mater.*, vol. 15, pp. 956–960, sep 2016.

[49] A. Mann, E. Baldini, A. Odeh, A. Magrez, H. Berger, and F. Carbone, "Probing the coupling between a doublon excitation and the charge-density wave in TaS_2 by ultrafast optical spectroscopy," *Phys. Rev. B*, vol. 94, p. 115122, sep 2016.

[50] H. Weng and K. Terakura, "Phase diagram of $LaVO_3$ under epitaxial strain: Implications for thin films grown on $SrTiO_3$ and $LaAlO_3$ substrates," *Phys. Rev. B*, vol. 82, no. 11, p. 115105, 2010.

[51] P. Horsch, A. M. Oleś, L. F. Feiner, and G. Khaliullin, "Evolution of Spin-Orbital-Lattice Coupling in the RVO_3 Perovskites," *Phys. Rev. Lett.*, vol. 100, p. 167205, apr 2008.

[52] G. Khaliullin, P. Horsch, and A. M. Oleś, "Spin Order due to Orbital Fluctuations: Cubic Vanadates," *Phys. Rev. Lett.*, vol. 86, pp. 3879–3882, apr 2001.

[53] H. Sawada, N. Hamada, K. Terakura, and T. Asada, "Orbital and spin orderings in YVO_3 and $LaVO_3$ in the generalized gradient approximation," *Phys. Rev. B*, vol. 53, no. 19, p. 12742, 1996.

[54] S. Tomimoto, S. Miyasaka, T. Ogasawara, H. Okamoto, and Y. Tokura, "Ultrafast photoinduced melting of orbital order in $LaVO_3$," *Phys. Rev. B*, vol. 68, no. 11, p. 035106, 2003.

[55] T. Arima, Y. Tokura, and J. B. Torrance, "Variation of optical gaps in perovskite-type 3d transition-metal oxides," *Phys. Rev. B*, vol. 48, pp. 17006–17009, dec 1993.

[56] D. G. Clarke, "Particle-hole bound states in Mott-Hubbard insulators," *Phys. Rev. B*, vol. 48, pp. 7520–7525, sep 1993.

[57] A. Gössling, R. Schmitz, H. Roth, M. W. Haverkort, T. Lorenz, J. A. Mydosh, E. Müller-Hartmann, and M. Grüninger, "Mott-Hubbard exciton in the optical conductivity of $YTiO_3$ and $SmTiO_3$," *Phys. Rev. B*, vol. 78, no. 7, p. 075122, 2008.

[58] J. T. C. Thomsen, H. T. Grahn, H. J. Maris, "Surface Generation and Detection of Phonons by Picosecond Light Pulses," *Phys. Rev. B*, vol. 34, no. 6, p. 4129, 1986.

[59] R. V. Yusupov, D. Mihailovic, C. V. Colin, G. R. Blake, and T. T. M. Palstra, "Critical phenomena and femtosecond ordering dynamics associated with electronic and spin-ordered phases in YVO_3 and $GdVO_3$," *Phys. Rev. B*, vol. 81, no. 7, p. 075103, 2010.

[60] J. Qi, L. Yan, H. D. Zhou, J. X. Zhu, S. A. Trugman, A. J. Taylor, Q. X. Jia, and R. P. Prasankumar, "Coexistence of coupled magnetic phases in epitaxial $TbMnO_3$ films revealed by ultrafast optical spectroscopy," *Appl. Phys. Lett.*, vol. 101, no. 12, p. 122904, 2012.

[61] S. Wall, D. Prabhakaran, A. T. Boothroyd, and A. Cavalleri, "Ultrafast Coupling between Light, Coherent Lattice Vibrations, and the Magnetic Structure of Semicovalent $LaMnO_3$," *Phys. Rev. Lett.*, vol. 103, p. 097402, aug 2009.

[62] K. Miyasaka, M. Nakamura, Y. Ogimoto, H. Tamaru, and K. Miyano, "Ultrafast photoinduced magnetic moment in a charge-orbital-ordered antiferromagnetic $_{0.5}Sr_{0.5}MnO_3$ thin film," *Phys. Rev. B*, vol. 74, no. 1, p. 012401, 2006.

[63] D. A. Mazurenko, A. A. Nugroho, T. T. Palstra, and P. H. Van Loosdrecht, "Dynamics of spin and orbital phase transitions in YVO_3," *Phys. Rev. Lett.*, vol. 101, no. 24, p. 245702, 2008.

[64] T. Kise, T. Ogasawara, M. Ashida, Y. Tomioka, Y. Tokura, and M. Kuwata-Gonokami, "Ultrafast Spin Dynamics and Critical Behavior in Half-Metallic Ferromagnet: Sr_2FeMoO_6," *Phys. Rev. Lett.*, vol. 85, pp. 1986–1989, aug 2000.

[65] S. Miyashita and H. Takano, "Dynamical Nature of the Phase Transition of the Two-Dimensional Kinetic Ising Model," *Prog. Theor. Phys.*, vol. 73, pp. 1122–1140, may 2005.

[66] P. C. Hohenberg and B. I. Halperin, "Theory of dynamic critical phenomena," *Rev. Mod. Phys.*, vol. 49, pp. 435–479, jul 1977.

[67] C.-w. Liu, A. Polkovnikov, and A. W. Sandvik, "Dynamic scaling at classical phase transitions approached through nonequilibrium quenching," *Phys. Rev. B*, vol. 89, p. 054307, feb 2014.

[68] J. P. Hinton, S. Patankar, E. Thewalt, A. Ruiz, G. Lopez, N. Breznay, A. Vishwanath, J. Analytis, J. Orenstein, J. D. Koralek, and I. Kimchi, "Photoexcited states of the harmonic honeycomb iridate γ-Li_2IrO_3," *Phys. Rev. B*, vol. 92, no. 11, p. 115154, 2015.

[69] A. Pelissetto and E. Vicari, "Critical phenomena and renormalization-group theory," *Phys. Rep.*, vol. 368, pp. 549–727, oct 2002.

[70] M. Campostrini, M. Hasenbusch, A. Pelissetto, P. Rossi, and E. Vicari, "Critical exponents and equation of state of the three-dimensional Heisenberg universality class," *Phys. Rev. B*, vol. 65, p. 144520, apr 2002.

[71] L. Onsager, "Crystal Statistics. I. A Two-Dimensional Model with an Order-Disorder Transition," *Phys. Rev.*, vol. 65, pp. 117–149, feb 1944.

[72] G. F. Mazenko and O. T. Valls, "Dynamic critical exponent z in some two-dimensional models," *Phys. Rev. B*, vol. 24, pp. 1419–1428, aug 1981.

[73] N. D. Mermin and H. Wagner, "Absence of Ferromagnetism or Antiferromagnetism in One- or Two-Dimensional Isotropic Heisenberg Models," *Phys. Rev. Lett.*, vol. 17, pp. 1133–1136, nov 1966.

[74] S. Miyasaka, Y. Okimoto, M. Iwama, and Y. Tokura, "Spin-orbital phase diagram of perovskite-type RVO_3 (R = rare-earth ion or Y)," *Phys. Rev. B*, vol. 68, p. 100406, sep 2003.

[75] L. D. Tung, A. Ivanov, J. Schefer, M. R. Lees, G. Balakrishnan, and D. M. Paul, "Spin, orbital ordering, and magnetic dynamics of $LaVO_3$: Magnetization, heat capacity, and neutron scattering studies," *Phys. Rev. B*, vol. 78, p. 054416, aug 2008.

[76] H. Ikeda, "Pseudo-Critical Dynamics in First-Order Transitions," *Prog. Theor. Phys.*, vol. 61, no. 4, pp. 1023–1033, 1979.

[77] Y. Zhu, J. Hoffman, C. E. Rowland, H. Park, D. A. Walko, J. W. Freeland, P. J. Ryan, R. D. Schaller, A. Bhattacharya, and H. Wen, "Unconventional slowing down of electronic recovery in photoexcited charge-ordered $La_{1/3}Sr_{2/3}FeO_3$," *Nat. Commun.*, vol. 9, p. 1799, dec 2018.

[78] R. P. Prasankumar, H. Okamura, H. Imai, Y. Shimakawa, Y. Kubo, S. A. Trugman, A. J. Taylor, and R. D. Averitt, "Coupled Charge-Spin Dynamics of the Magnetoresistive Pyrochlore $Tl_2Mn_2O_7$ Probed Using Ultrafast Midinfrared Spectroscopy," *Phys. Rev. Lett.*, vol. 95, p. 267404, dec 2005.

[79] M. Mochizuki and M. Imada, "Orbital physics in the perovskite Ti oxides," *New J. Phys.*, vol. 6, p. 154, 2004.

[80] Y. Tokura, "Fillingness dependence of electronic structures in strongly correlated electron systems: Titanates and vanadates," *J. Phys. Chem. Solids*, vol. 53, pp. 1619–1625, dec 1992.

[81] C. W. Turner and J. Greedan, "Ferrimagnetism in the rare earth titanium (III) oxides, $RTiO_3$; R = Gd, Tb, Dy, Ho, Er, Tm," *J. Solid State Chem.*, vol. 34, pp. 207–213, sep 1980.

[82] Y. Okimoto, T. Katsufuji, Y. Okada, T. Arima, and Y. Tokura, "Optical spectra in (La,Y)TiO_3: Variation of Mott-Hubbard gap features with change of electron correlation and band filling," *Phys. Rev. B*, vol. 51, pp. 9581–9588, apr 1995.

[83] M. Itoh, M. Tsuchiya, H. Tanaka, and K. Motoya, "Orbital Ordering and Local Magnetic Properties of Mott-Hubbard Insulators $YTiO_3$ and $LaTiO_3$: NMR Study," *J. Phys. Soc. Japan*, vol. 68, no. 8, pp. 2783–2789, 1999.

[84] M. Mochizuki and M. Imada, "Origin of G-type antiferromagnetism and orbital-spin structures in $LaTiO_3$," *J. Phys. Soc. Japan*, vol. 70, no. 10, pp. 2872–2875, 2001.

[85] H. D. Zhou and J. B. Goodenough, "Localized or itinerant TiO_3 electrons in $RTiO_3$ perovskites," *J. Phys. Condens. Matter*, vol. 17, no. 46, pp. 7395–7406, 2005.

[86] K. Takubo, M. Shimuta, J. E. Kim, K. Kato, M. Takata, and T. Katsufuji, "Crossover behavior of the crystal structure and the relation to magnetism in perovskite $RTiO_3$," *Phys. Rev. B*, vol. 82, no. 2, p. 020401, 2010.

[87] E. Pavarini, S. Biermann, A. Poteryaev, A. I. Lichtenstein, A. Georges, and O. K. Andersen, "Mott Transition and Suppression of Orbital Fluctuations in Orthorhombic $3d^1$ Perovskites," *Phys. Rev. Lett.*, vol. 92, no. 17, p. 176403, 2004.

[88] M. Mochizuki and M. Imada, "Magnetic and Orbital States and Their Phase Transition of the Perovskite-Type Ti Oxides: Strong Coupling Approach," *J. Phys. Soc. Japan*, vol. 70, pp. 1777–1789, jun 2001.

[89] A. C. Komarek, H. Roth, M. Cwik, W. D. Stein, J. Baier, M. Kriener, F. Bourée, T. Lorenz, and M. Braden, "Magnetoelastic coupling in $RTiO_3$ (R=La,Nd,Sm,Gd,Y) investigated with diffraction techniques and thermal expansion measurements," *Phys. Rev. B*, vol. 75, no. 22, p. 224402, 2007.

[90] J. Y. Zhang, C. A. Jackson, S. Raghavan, J. Hwang, and S. Stemmer, "Magnetism and local structure in low-dimensional Mott insulating $GdTiO_3$," *Phys. Rev. B*, vol. 88, no. 12, p. 121104, 2013.

[91] J. Varignon, M. N. Grisolia, D. Preziosi, P. Ghosez, and M. Bibes, "Origin of the orbital and spin ordering in rare-earth titanates," *Phys. Rev. B*, vol. 96, no. 23, p. 235106, 2017.

[92] G. Amow, J. S. Zhou, and J. B. Goodenough, "Peculiar magnetism of the $Sm_{(1-x)}Gd_xTiO_3$ system," *J. Solid State Chem.*, vol. 154, no. 2, pp. 619–625, 2000.

[93] J. Liu, K. Hejazi, and L. Balents, "Floquet Engineering of Multiorbital Mott Insulators: Applications to Orthorhombic Titanates," *Phys. Rev. Lett.*, vol. 121, no. 10, p. 107201, 2018.

[94] G. Khalsa and N. A. Benedek, "Ultrafast optically induced ferromagnetic/antiferromagnetic phase transition in $GdTiO_3$ from first principles," *npj Quantum Mater.*, vol. 3, no. 15, 2018.

[95] P. Moetakef, J. Y. Zhang, S. Raghavan, A. P. Kajdos, and S. Stemmer, "Growth window and effect of substrate symmetry in hybrid molecular beam epitaxy of a Mott insulating rare earth titanate," *J. Vac. Sci. Technol. A Vacuum, Surfaces, Film.*, vol. 31, p. 041503, jul 2013.

[96] J. L. Schmehr, M. Aling, E. Zoghlin, and S. D. Wilson, "High-pressure laser floating zone furnace," *Rev. Sci. Instrum.*, vol. 90, p. 043906, apr 2019.

[97] A. B. Kuzmenko, "Kramers-Kronig constrained variational analysis of optical spectra," *Rev. Sci. Instrum.*, vol. 76, no. 8, p. 083108, 2005.

[98] D. Crandles, T. Timusk, J. Garrett, and J. Greedan, "The midinfrared absorption in $RTiO_3$ perovskites (R = La, Ce, Pr, Nd, Sm, Gd): The Hubbard gap?," *Phys. C Supercond.*, vol. 201, pp. 407–412, oct 1992.

[99] L. Bjaalie, A. Verma, B. Himmetoglu, A. Janotti, S. Raghavan, V. Protasenko, E. H. Steenbergen, D. Jena, S. Stemmer, and C. G. Van De Walle, "Determination of the Mott-Hubbard gap in $GdTiO_3$," *Phys. Rev. B*, vol. 92, no. 8, p. 085111, 2015.

[100] F. Wang, N. Hatano, and M. Suzuki, "Study on dynamical critical exponents of the Ising model using the damage spreading method," *J. Phys. A. Math. Gen.*, vol. 28, pp. 4543–4552, aug 1995.

[101] P. Moetakef, D. G. Ouellette, J. Y. Zhang, T. A. Cain, S. J. Allen, and S. Stemmer, "Growth and properties of $GdTiO_3$ films prepared by hybrid molecular beam epitaxy," *J. Cryst. Growth*, vol. 355, no. 1, pp. 166–170, 2012.

[102] J. Wang, C. Sun, J. Kono, A. Oiwa, H. Munekata, A. Cywiński, and L. J. Sham, "Ultrafast Quenching of Ferromagnetism in InMnAs Induced by Intense Laser Irradiation," *Phys. Rev. Lett.*, vol. 95, no. 16, p. 167401, 2005.

[103] A. Vaterlaus, T. Beutler, and F. Meier, "Spin-lattice relaxation time of ferromagnetic gadolinium determined with time-resolved spin-polarized photoemission," *Phys. Rev. Lett.*, vol. 67, no. 23, pp. 3314–3317, 1991.

[104] A. V. Kimel, R. V. Pisarev, J. Hohlfeld, and T. Rasing, "Ultrafast Quenching of the Antiferromagnetic Order in $FeBO_3$: Direct Optical Probing of the Phonon-Magnon Coupling," *Phys. Rev. Lett.*, vol. 89, no. 28, p. 287401, 2002.

[105] E. Beaurepaire, M. Maret, V. Halte, J.-C. Merle, A. Daunois, and J.-Y. Bigot, "Spin dynamics in $CoPt_3$ alloy films: A magnetic phase transition in the femtosecond time scale," *Phys. Rev. B*, vol. 58, no. 18, pp. 12134–12137, 1998.

[106] T. Ogasawara, K. Ohgushi, Y. Tomioka, K. S. Takahashi, H. Okamoto, M. Kawasaki, and Y. Tokura, "General features of photoinduced spin dynamics in ferromagnetic and ferrimagnetic compounds," *Phys. Rev. Lett.*, vol. 94, no. 8, p. 087202, 2005.

[107] M. Weiler, L. Dreher, C. Heeg, H. Huebl, R. Gross, M. S. Brandt, and S. T. Goennenwein, "Elastically driven ferromagnetic resonance in nickel thin films," *Phys. Rev. Lett.*, vol. 106, no. 11, p. 117601, 2011.

[108] E. Rossi, O. G. Heinonen, and A. H. MacDonald, "Dynamics of magnetization coupled to a thermal bath of elastic modes," *Phys. Rev. B*, vol. 72, no. 17, p. 174412, 2005.

[109] S. Streib, H. Keshtgar, and G. E. Bauer, "Damping of Magnetization Dynamics by Phonon Pumping," *Phys. Rev. Lett.*, vol. 121, no. 2, p. 27202, 2018.

[110] R. I. Thomson, T. Chatterji, and M. A. Carpenter, "CoF_2: A model system for magnetoelastic coupling and elastic softening mechanisms associated with paramagnetic $\leftrightarrow$ antiferromagnetic phase transitions," *J. Phys. Condens. Matter*, vol. 26, no. 14, p. 146001, 2014.

[111] J. R. Neighbors and R. W. Moss, "Ultrasonic attenuation near the magnetic critical point of MnF_2," *Phys. Rev.*, vol. 173, no. 2, p. 542, 1968.

[112] H. S. Bennett and E. Pytte, "Ultrasonic Attenuation in the Heisenberg Paramagnet," *Phys. Rev.*, vol. 155, no. 2, p. 553, 1967.

[113] S. K. Ghatak, "Acoustic Attenuation and Frequency Shift in Ferromagnetic Insulators at Low Temperature," *Phys. Rev. B*, vol. 5, no. 9, p. 3702, 1972.

[114] J. W. Kim, M. Vomir, and J. Y. Bigot, "Ultrafast Magnetoacoustics in Nickel Films," *Phys. Rev. Lett.*, vol. 109, no. 16, p. 166601, 2012.

[115] J. W. Kim, M. Vomir, and J. Y. Bigot, "Controlling the spins angular momentum in ferromagnets with sequences of picosecond acoustic pulses," *Sci. Rep.*, vol. 5, no. 8511, pp. 1–7, 2015.

[116] T. F. Nova, A. Cartella, A. Cantaluppi, M. Först, D. Bossini, R. V. Mikhaylovskiy, A. V. Kimel, R. Merlin, and A. Cavalleri, "An effective magnetic field from optically driven phonons," *Nat. Phys.*, vol. 13, no. 2, pp. 132–136, 2017.

[117] Y. Furukawa, I. Okamura, K. Kumagai, Y. Taguchi, and Y. Tokura, "NMR Study on Electronic and Magnetic State in $RTiO_3$ (R=La, Y)," *J. Low Temp. Phys.*, vol. 105, pp. 413–418, 1996.

[118] Y. Furukawa, I. Okamura, K. Kumagai, Y. Taguchi, and Y. Tokura, "NMR study of ferromagnetic $YTiO_3$ and antiferromagnetic $LaTiO_3$," *Phys. B Condens. Matter*, vol. 237-238, pp. 39–40, 1997.

[119] M. Itoh and M. Tsuchiya, "Orbital ordering in $YTiO_3$ observed by NMR," *J. Magn. Magn. Mater.*, vol. 226-230, pp. 874–875, may 2001.